TRUMPET INITIAL DATA FOR HIGHLY BOOSTED BLACK HOLES AND HIGH ENERGY BINARIES

Kyle Patrick Slinker

A dissertation submitted to the faculty at the University of North Carolina at Chapel Hill in partial fulfillment of the requirements for the degree of Doctor of Philosophy in the Department of Physics and Astronomy.

Chapel Hill
2017

Approved by:

Charles R. Evans

J. Christopher Clemens

Louise A. Dolan

Joaquín E. Drut

Fabian Heitsch

Reyco Henning

ABSTRACT

Kyle Patrick Slinker: Trumpet Initial Data for Highly Boosted Black Holes and High Energy Binaries
(Under the direction of Charles R. Evans)

Initial data for a single boosted black hole is constructed that analytically contains no initial transient (junk) gravitational radiation and is adapted to the moving punctures gauge conditions. The properties of this data are investigated in detail. It is found to be generally superior to canonical Bowen-York data and, when implemented numerically in simulations, yields orders of magnitude less junk gravitational radiation content and more accurate black hole velocities. This allows for modeling of black holes that are boosted faster than previously possible. An approximate superposition of the data is used to demonstrate how a binary black hole system can be constructed to retain the advantages found for the single black hole. Extensions to black holes with spin are considered.

TABLE OF CONTENTS

LIST OF TABLES

LIST OF FIGURES

LIST OF ABBREVIATIONS AND SYMBOLS

ADM — Arnowitt, Deser, and Misner

LIGO — Laser Interferometer Gravitational-Wave Observatory

AMR — adaptive mesh refinement

BSSN — Baumgarte, Shapiro, Shibata, and Nakamura

LHS, RHS — left hand side and right hand side of an equation

CFL — Courant-Friedrichs-Lewy

ODE — ordinary differential equation

$\mathcal{M}$ — spacetime manifold

g_{ab}, g — spacetime metric on $\mathcal{M}$ with signature $(-,+,+,+)$ and its determinant

$a, b, c, d, e, f, \ldots$ — spacetime indices, running from 0 to 3 $(t, x, y, z$ or $t, r, \theta, \phi)$

$^{(4)}\Gamma^a_{\ bc}$, ∇_a — Christoffel symbols and covariant derivative compatible with g_{ab}

$^{(4)}R_{abcd}$, $^{(4)}C_{abcd}$, $^{(4)}R_{ab}$, $^{(4)}R$, G_{ab} — Riemann tensor, Weyl tensor, Ricci tensor, Ricci scalar, and Einstein tensor describing the curvature of $\mathcal{M}$

Σ — spatial slice in the foliation of $\mathcal{M}$

n^a, t^a, ω_a, Ω_a — normal vectors to Σ and related 1-forms

$\mathbb{P}^a_b$ — operator to project object "into" spatial slice: $\mathbb{P}^a_b = \delta^a_b + n^a n_b$

γ_{ij}, γ — spatial metric on Σ with signature $(+,+,+)$ and its determinant

$i, j, k, l, m, n, \ldots$ — spatial indices, running from 1 to 3 $(x, y, z$ or $r, \theta, \phi)$

$\Gamma^i_{\ jk}$, D_i — Christoffel symbols and covariant derivative compatible with the spatial three-metric γ_{ij}

R_{ijkl}, R_{ij}, R — three-dimensional Riemann tensor, Ricci tensor, and Ricci scalar describing the intrinsic curvature of Σ

α, β^i, K_{ij}, K — lapse, shift, extrinsic curvature, and mean curvature describing foliation of the spatial slices within $\mathcal{M}$

$\mathcal{S}$	2-sphere slice in the foliation of Σ
q_{AB}, q	angular metric on $\mathcal{S}$ and its determinant
A, B	angular indices, running from 2 to 3 (θ and ϕ)
σ, ω^A	lapse and shift analogs describing foliation of the spherical surfaces within a spatial slice
$d\Omega$	area element of a sphere $d\Omega \equiv \sin\theta d\theta d\phi$
H, M^i	Hamiltonian constraint violation (2.48a) and momentum constraint violation (2.48b)
δ^a_b, ε_{abcd}, ε_{ijk}	Kronecker delta and totally anti-symmetric tensors
$\mathcal{L}$	Lie derivative
T_{ab}, S_{ij}, S_i, S, ρ	stress-energy tensor and its projections (2.30)
R	the Schwarzschild radial coordinate
f	$1 - 2M/R$
TT	the transverse-traceless piece of a tensor
$\sim$	a conformally related quantity
$\tilde{\gamma}_{ij}$, ψ, ϕ, W^i, A_{ij}, $\tilde{A}_{ij}$, $\tilde{A}^{ij}_{TT}$, $\tilde{A}^{ij}_L$	pieces of the conformal decomposition
$\left(\tilde{\mathbb{L}}W\right)^{ij}$, $\left(\tilde{\Delta}_{\mathbb{L}}W\right)^i$	symmetrized transverse-traceless gradient (2.65) and vector Laplacian (2.68)
$\tilde{R}_{ij}$, R^ϕ_{ij}, $\tilde{\Gamma}_i$, ∂_0	quantities for the BSSN equations (2.75)
h_{ab}, $^{(1)}h_{ab}$, $^{(2)}h_{ab}$	perturbations to the spacetime metric g_{ab}
k^a, l^a, m^a, $\overline{m}^a$	null tetrad basis vectors
M_{ADM}, P^i_{ADM}, J^i_{ADM}	ADM mass, momentum, and angular momentum
Θ	expansion of outgoing light rays at the horizon
$\mathcal{H}$	the horizon at all times $\mathcal{S} = \mathcal{H} \cap \Sigma$

$M_\mathcal{S}$, $J_\mathcal{S}$, $R_\mathcal{S}$, $A_\mathcal{S}$	mass and angular momentum defined by symmetries on the horizon and radius and area of the horizon
ψ_0, ψ_1, ψ_2, ψ_3, ψ_4	Weyl scalars
$\mathcal{I}$, $\mathcal{J}$	Weyl curvature invariants
$e_{ab}^\times$, e_{ab}^+, $h_\times$, h_+	tensor wave polarizations and their amplitudes
$\eth$, $\bar{\eth}$	derivative operators for raising and lower spin weights
$_s Y_{lm}$	spherical harmonic of spin weight s
T_{ab}^{GW}	stress-energy of GWs
L_{GW}	luminosity of GWs
$^{(1)}R_{ab}$, $^{(2)}R_{ab}$	perturbations to the Ricci tensor
$\langle \quad \rangle$	time average over many GW cycles
$\mathcal{F}$	Fourier transform
$\mathbf{L}$, $\mathbf{U}$, $\mathbf{D}$, $\ldots$	matrices
$\vec{x}$, $\vec{b}$, $\ldots$	vectors

CHAPTER 1:   Introduction

Historically, tests of general relativity have taken place in our solar system and were generally only able to probe the weak field limit. This has changed with the recent rapid progress in the field of gravitational wave astronomy. In the past two years, this new field has given us novel tests of general relativity, not possible within our own solar system. As instrument sensitivities are increased, it promises to provide more stringent tests in the future. In order to properly understand observations, comparisons with theory must be made. Accurate methods exist for simulating highly relativistic systems, but there is the non-trivial issue of how to initialize simulations. This project provides improved methods for computing initial data. This Chapter gives an overview of tests of general relativity, simulation methods, and what this project has accomplished.

Section 1.1:   Testing General Relativity Through Gravitational Wave Astronomy

One of the most famous tests of general relativity which has been carried out in the solar system is the perihelion advance of Mercury: the measured value $(42.98 \pm 0.04)''$/century [43] is in remarkably good agreement with the value calculated from theory $42.98''$/century [43]. The Cassini-Huygens spacecraft was able to perform measurements of the Shapiro time delay during its flight to Saturn and measured the parameterized post-Newtonian parameter γ; if general relativity is correct it is expected that $\gamma = 1$. The measured value $\gamma - 1 = (2.1 \pm 2.3) \times 10^{-5}$ [55] is consistent with zero, indicating that no deviation from general relativity was detected. Violations of the weak equivalence principle have been constrained to be at most a few parts in 10^{13} by Eötvös-type experiments [54]. These are only a few of many tests. None of these findings have contradicted general relativity, but they have only tested it in the weak field limit.

Observations of the Hulse-Taylor pulsar have probed general relativity in an environment with a stronger gravitational field. This pulsar is one of two neutron stars forming a binary system [31]. The observed time rate of change of the orbital period of this binary system $(-2.396 \pm 0.005) \times 10^{-12}$ is once again remarkably close to the predicted value $(-2.402531 \pm 0.000014) \times 10^{-12}$ [55].[1] This is generally seen as the first observational evidence for the existence of gravitational waves, but the measurement was made through electromagnetic observations and is therefore somewhat indirect.

---

[1] Using $31\,557\,600$ s $= 1$ year, these values correspond to (75.6 ± 0.2) μs/year (observed) and (75.8181 ± 0.0004) μs/year (predicted).

It is only with the recent detections by the advanced Laser Interferometer Gravitational-Wave Observatory (LIGO) that we have obtained our first direct measurements of gravitational waves. The first four detected events – dubbed GW150914 [6], GW151226 [11], GW170104 [12], and GW170814 [8] – were each generated by the co-orbital motion and merger of a pair of black holes. The fifth detection – GW170817 [9] – was of a signal from the merger of two neutron stars. But the existence of gravitational waves is not the only strong field test of general relativity that gravitational wave astronomy can provide. The mass of the graviton was constrained to be less than 1.2×10^{-22} eV (corresponding to a Compton wavelength of over a lightyear) [7] by the dispersion of gravitational waves detected from GW150914. Additionally, GW150914 allowed for constraints on deviations from general relativity, even if some of these constraints are not particularly strong [7].

To be able to connect the raw data of the detection to a physical model of the emitting system we must have a well developed understanding of general relativity [10]. General relativity is non-linear, which makes it difficult to work with mathematically. Perturbative methods exist to handle its non-linearities iteratively, including black hole perturbation theory and post-Newtonian expansions [35, 42, 22]. These methods require restrictive physical properties, such as a small ratio between the masses of the orbiting objects or low velocities; the signals detected by LIGO came from systems which do not possess these properties. Therefore, for these systems, perturbative processes break down and Einstein's equations must be solved 'all at once.' To distinguish it from perturbative methods, this 'all at once' method is called numerical relativity [20, 13]. Although all of these methods inform one another, are important, and ultimately must all be understood to get the fullest picture of general relativity, numerical relativity is currently our only tool to model the inspiral, merger, and remnant of compact binaries that are being observed.

Section 1.2:   Numerical Relativity

One downside of numerical relativity as compared with other methods is the relative difficultly in constructing initial data for a simulation. Consider briefly a simulation of electromagnetic fields. Two of Maxwell's equations (Coulomb's law and $\vec{\nabla} \cdot \vec{B} = 0$) constrain the possible configurations of the electric and magnetic fields, and these constraints must be satisfied at any time. When starting a simulation, data must be given for the electric and magnetic fields which satisfies these constraints. This may require solving a Poisson equation for the initial electric potential, for example. Similarly, Einstein's equations do not allow for arbitrary configurations of the gravitational field, and it is non-trivial to pose initial data which is properly constrained.

One of the most widely used codes for numerical relativity is the Einstein Toolkit [32]. The current state-

of-the-art initial data in use with the Einstein Toolkit is based on the Bowen-York formalism [23, 57]. This formalism makes mathematical assumptions in order to greatly simplify the constraint equations, allowing valid initial data to be computed more easily. This data solves the constraint equations, which is required for a mathematically valid solution to Einstein's equations. It does not, however, accurately model the intended physical system. As we will see, initial data computed this way contains non-physical 'junk radiation' which initially distorts the space near the black holes and is released as gravitational waves at the start of the simulation. This junk signal robs the black holes of energy, momentum, and angular momentum and contaminates the physically relevant gravitational wave signal.

In order to distinguish the junk signal from the physical gravitational wave signal which appears later, the black holes must be started farther apart (increasing the duration of the simulation) and the boundary of the simulation domain must be farther out (to reduce the impact of reflected waves on the simulation). Both allowances drive up the computational cost of a simulation, but this is not the only problem with junk radiation. Areas of parameter space are precluded as the energy and angular momentum carried away by junk radiation limits the range of spins and momenta of black holes that can be simulated. Because astrophysical black holes are expected to have large spins, this limitation on spins is more than just a pedantic concern [33].

Clearly, it would be advantageous to have an alternate method for constructing initial data. However, the method by which the black hole singularity is handled numerically plays a large role in how initial data can be constructed. One method for handling singularities is the so-called 'excision' method. In this method, the interior of the black holes – where large gradients and infinite values are present – are removed from the simulation domain. This creates the need to specify interior boundary conditions and remove a roughly ellipsoidal region from a cubical lattice; but information cannot leave a black hole in classical general relativity so there is no need to simulate its interior. This method has been found to be amenable to using a Lorentz-like coordinate transformation to boost a black hole written in Kerr-Schild coordinates to generate initial data [34], as well as initial data modifications to reduce junk radiation content [49, 50].

The Einstein Toolkit does not use excision, instead it uses the 'moving punctures' method. Moving punctures is the name given to a specific set of choices for the spacetime coordinates.[2] Like excision, a moving punctures coordinate system has the effect of removing a black hole's singularity from the simulation domain. However, unlike excision, moving punctures does not remove any points from the simulation grid. Instead, the coordinates are engineered so that they only cover a portion of the spacetime manifold away from the black hole singularities; this coordinate patch corresponds to the simulation domain. This can be

---

[2]Recall that the gauge freedom of general relativity allows us to choose any coordinate system.

accomplished using a so called 'trumpet slicing,' a specific topology where the spatial slices reach a limit a finite distance away from any singularities. The moving punctures gauge is not the only coordinate system that gives trumpet slicing, but it is an example of trumpet slicing which is well suited to numerical work.

It has been shown that, over the course of a simulation, the moving punctures gauge conditions drive Bowen-York initial data away from its initial (non-trumpet) slicing to trumpet slicing [30]. Trumpet slicing has been explored for non-moving, non-rotating [25] and non-moving, rotating black holes [26] in a gauge other than moving punctures, and also for a non-moving, non-rotating black hole in the moving punctures gauge [30]. Recent attempts to decrease junk radiation content of initial data within the moving punctures scheme have focused on relaxing one of the Bowen-York assumptions without using trumpet slicing [46].

Section 1.3:   Project Goals

We have discussed the importance of strong field tests of general relativity, the importance of numerical relativity to these tests, and the importance of well constructed initial data to numerical relativity. The goal of this project has been to improve the Einstein Toolkit by improving the tools available for construction of initial data, utilizing the specific trumpet slicing that is the steady state of the moving punctures gauge.

At its core, this work has combined the ideas of trumpets in moving punctures gauge and a Lorentz boosted Schwarzschild black hole. By creating a series of coordinate changes, we transform a black hole written in a common coordinate system to a black hole with both non-zero coordinate velocity and trumpet slicing adapted to the moving punctures gauge.

To understand the big picture better, return momentarily to the electromagnetic simulation considered above. Suppose we have initial data for the vector potential which we know gives electric and magnetic fields which satisfy Maxwell's two constraint equations, but that this initial data is not well suited to our numerical methods. We might then apply a gauge transformation to this vector potential to obtain different initial data which models the same physical situation (i.e., the electric and magnetic fields are unchanged). The result is guaranteed to satisfy the constraint equations, and this known without explicitly solving them. This is analogous to what we propose here: we start with Schwarzschild spacetime in the familiar Schwarzschild coordinates (a simple, known solution to the constraints that is not well suited for simulation) and apply a series of coordinate (gauge) transformations to get it in a form that may look more complex, but represents the same physical situation.

The idea for this project can be stated simply, but the detailed properties of the resulting coordinate system are complicated to understand. Having applied a series of coordinate transformations to Schwarzschild spacetime, the result is still a Schwarzschild black hole, even if its Killing symmetries are no longer as

4

apparent. A large part of this project has been concerned with the interpretation of the properties of the resulting coordinate system.

Section 1.4:   Outline of the Remainder of the Thesis

Chapters 2 through 4 give overviews of various required aspects of simulating black holes. With that foundation laid, we then discuss novel methods for constructing initial data and the results of this project, found in Chapters 5 and 6. Throughout this work, we use units where $G = 1 = c$,[3] the spacetime metric signature is $(-, +, +, +)$, and sign conventions are those of Misner, Thorne, and Wheeler [35].

Chapter 2 discusses a number of formalisms needed to carry out numerical relativity simulations. There we make explicit the formulation of Einstein's equations as a Cauchy initial value problem and explore the options for solving for initial data, including the Bowen-York method.

Chapter 3 gives an overview of how a number of physical properties of spacetimes are extracted from simulations. Among these properties are the energy, momentum, and angular momentum contained in a spacetime, the gravitational wave content of the spacetime, and black hole horizon properties.

Chapter 4 gives a very brief overview of relevant numerical methods and how the Einstein Toolkit implements them.

Chapter 5 describes our new method for constructing initial data. We compare results from this data to those found using Bowen-York data. We find that it is well adapted to the moving punctures gauge conditions and contains orders of magnitude less junk gravitational waves than the Bowen-York data. We also carry out analysis to gain a thorough understanding of the properties of the new coordinate system we have created.

Chapter 6 examines preliminary results of a binary composed of boosted-trumpet black holes. The initial data for this binary system is constructed by a simple superposition of the data for a single black hole.

Finally, Chapter 7 summarizes our findings.

---

[3]So 1 $M_\odot \approx 1.5$ km ≈ 4.9 μs.

CHAPTER 2:   Decomposing Spacetimes and Einstein's Equations

In order to be dealt with numerically, Einstein's equations must be separated into space and time parts. This breaks their inherently covariant nature but does allow for a formulation in terms of a Cauchy problem, which is more amenable to numerical evolution. We describe a formalism for decomposing spacetime and Einstein's equations in this Chapter.

In the first section of this Chapter, we will foliate the spacetime manifold $\mathcal{M}$ by dividing it into a collection of three-dimensional spacelike surfaces Σ. Each Σ can be interpreted as representing the universe at an instant in time, and collectively the Σ cover the portion of $\mathcal{M}$ in which we are interested. We will then compute curvature quantities for the spatial slices and relate them to the curvature quantities describing $\mathcal{M}$. These quantities will allow us to decompose Einstein's equations via temporal and spatial projections. Finally, we will specialize to a specific basis to bring out a time derivative, culminating in the Arnowitt, Deser, and Misner (ADM) equations [20, 28, 56]. In investigating the nature of the ADM equations, we will see the consequences of general relativity's coordinate freedom and how it can be used to improve numerical stability.

The second section carries the decomposition one step further, foliating a spatial slice into a collection of surfaces which are topologically spherical. This allows us to define the idea of trumpet slicing. The final section outlines a conformal decomposition which is useful in numerically solving the constraint equations obtained in section 2.1 in order to give initial data in practice.

Section 2.1:   ADM Formalism for Foliation and 3+1 Decomposition of Spacetime

Before investigating the exact nature of the decomposition, we look to see generally how it must come about. Consider the twice contracted Bianchi identity

$$\nabla_b G^{ab} = 0, \tag{2.1}$$

and Einstein's equations with indices raised

$$G^{ab} = 8\pi T^{ab}. \tag{2.2}$$

Separating the Bianchi identity into the timelike derivative and spatial derivatives, we find

$$\nabla_0 G^{a0} = -\nabla_i G^{ai}. \tag{2.3}$$

Because G^{ab} is a curvature quantity which is constructed from derivatives of the metric, including second derivatives, $\nabla_i G^{ai}$ contains at most second time derivatives of g_{ab}. Therefore, $\nabla_0 G^{a0}$ contains at most second time derivatives and so G^{a0} contains at most first time derivatives. Thus, four of Einstein's equations,

$$G^{a0} = 8\pi T^{a0}, \tag{2.4}$$

relate the metric and its first time derivatives, and are therefore constraint equations which must be satisfied initially and at all subsequent times. The evolution equations are the remaining six Einstein's equations,

$$G^{ij} = 8\pi T^{ij}, \tag{2.5}$$

which govern the evolution of the spacetime. The system may appear under specified as there are only six evolution equations for the ten metric components. However, there are four degrees of gauge freedom corresponding to coordinate changes; specifying four equations in order to fix the coordinate system brings the total number of equations back up to ten. Given these considerations, it is perhaps not surprising that we will find that doing at least one temporal projection gives us a constraint while two spatial projections will give us evolution equations.

Analytically, if the constraint equations are satisfied initially, they will continue to be satisfied. We see this because

$$\nabla_b \left(G^{ab} - 8\pi T^{ab} \right) = 0 \tag{2.6}$$

which means

$$\nabla_0 \left(G^{a0} - 8\pi T^{a0} \right) = -\nabla_i \left(G^{ai} - 8\pi T^{ai} \right). \tag{2.7}$$

If, on some slice, data is given which satisfies Einstein's equations, the RHS of (2.7) will be zero. The LHS then tells us that the value of the constraint violation will not change away from the initial slice. This means that if the constraints are satisfied at one time then, analytically, they must be satisfied at all times. Compare this with Maxwell's equations, where $\vec{\nabla} \times \vec{E} = -\partial \vec{B}/\partial t$ requires that $\vec{\nabla} \cdot \vec{B} = 0$ remain true if it is satisfied initially.

The foliation of $\mathcal{M}$ consists of a collection of spacelike surfaces which are level sets of a function $\tilde{t} : \mathcal{M} \to \mathbb{R}$. This function can loosely be interpreted as a time associated with each slice of the foliation. We can create

a normal vector to the surfaces by working with the gradient of $\tilde{t}$. To this end, define a one-form as the exterior derivative of $\tilde{t}$

$$\omega_a \equiv \left(d\tilde{t}\right)_a. \tag{2.8}$$

Note that, in general, ω_a is timelike and will have a variable norm

$$g^{ab}\omega_a\omega_b = -\alpha^{-2}. \tag{2.9}$$

This defines the 'lapse' function α. With this we can create another timelike one form which is unit normalized

$$\Omega_a \equiv \alpha\omega_a \tag{2.10}$$

so that

$$g^{ab}\Omega_a\Omega_b = -1. \tag{2.11}$$

The unit normal vector is then

$$n^a \equiv -g^{ab}\Omega_b, \tag{2.12}$$

it is also timelike

$$n^a n_a = -1, \tag{2.13}$$

where the sign in (2.12) is chosen so that n^a points in the future direction (increasing $\tilde{t}$) when the lapse is positive

$$n^a\nabla_a\tilde{t} = n^a\omega_a = \alpha^{-1}. \tag{2.14}$$

There are many timelike vector fields t^a which satisfy the normalization $\omega_a t^a = 1$ relative to the foliation. One possible choice for t^a is αn^a, but we are free to add a vector β^a (called the 'shift' vector) which satisfies $n_a\beta^a = 0$ but is otherwise arbitrary, and still maintain the normalization

$$\omega_a\left(\alpha n^a + \beta^a\right) = 1. \tag{2.15}$$

Spatial coordinates are dragged from time slice to time slice in the direction t^a. In this way, the decomposition

$$t^a = \alpha n^a + \beta^a \tag{2.16}$$

shows that the lapse function α and the shift vector β^a encode the development of the coordinate system.

We will find these two quantities very important moving forward, where their interpretation will be more fully explored. Equations governing the evolution of α and β^a will determine the coordinate system and, as mentioned above, complement the six evolution equations coming from Einstein's equations to give ten equations needed to specify the dynamics of the ten independent pieces of the spacetime metric g_{ab}.

Contracting a vector with $-n^a n_b$ gives its projection in a timelike direction, so $-n^a n_b$ can be thought of as a temporal projection operator. If V^a is a vector such that $V^a n_a = 0$ then V^0 is not algebraically independent from V^i and the vector V^a has three degrees of freedom, effectively containing no timelike information. The same idea holds for tensors of all ranks and index structures. In general, a tensor is said to be 'spatial' when all of its contractions with n^a (or n_a) give zero. When dealing with spatial tensors, we are free to disregard any timelike components; as we have seen, they are not independent and – if needed – we can recover them by contracting with n^a, setting the result equal to zero, and solving algebraically. We will make liberal use of this in the future and for simplicity's sake often only consider the spatial indices. A spatial projection operator can also be constructed from n^a

$$\mathbb{P}^a_b \equiv \delta^a_b + n^a n_b. \tag{2.17}$$

Consider an arbitrary (in particular, not necessarily spatial) covector C_a acted on by $\mathbb{P}^a_b$ and n^b

$$n^b \mathbb{P}^a_b C_a = n^b \left(\delta^a_b + n^a n_b \right) C_a = \left(n^a - n^a \right) C_a = 0. \tag{2.18}$$

As can be seen, this result is independent of C_a and thus demonstrates how $\mathbb{P}^a_b C_a$ is spatial by virtue of the construction of $\mathbb{P}^a_b$. When every index of a tensor has been projected into Σ by $\mathbb{P}^a_b$, the tensor is guaranteed to be spatial.

By projecting the spacetime metric g_{ab} into Σ, we obtain a 'spatial metric'

$$\gamma_{ab} \equiv \mathbb{P}^c_a \mathbb{P}^d_b g_{cd} = g_{ab} + n_a n_b \tag{2.19}$$

which makes Σ a Riemannian manifold in its own right. The spatial metric is positive definite and can be used to raise and lower indices of spatial tensors. The covariant derivative D_a in Σ arises naturally from the geometric structure of $\mathcal{M}$: first the spacetime covariant derivative ∇_a is taken and then every index of the result is projected into Σ. With this definition, D_a can be shown to be compatible with γ_{ab}

$$D_a \gamma_{bc} \equiv \mathbb{P}^d_a \mathbb{P}^e_b \mathbb{P}^f_c \nabla_d \gamma_{ef} = \mathbb{P}^d_a \mathbb{P}^e_b \mathbb{P}^f_c \left(n_e \nabla_d n_f + n_f \nabla_d n_e \right) = 0. \tag{2.20}$$

Thus, we know it must also be possible to find connection coefficients for D_a

$$\Gamma^i{}_{jk} \equiv \frac{1}{2}\gamma^{il}\left(\gamma_{lk,j} + \gamma_{jl,k} - \gamma_{jk,l}\right),\tag{2.21}$$

and covariant derivatives in Σ can be computed without reference to the geometric structure of $\mathcal{M}$. All the other usual intrinsic curvature quantities can be similarly defined in Σ; in particular, the curvature of Σ is described by a three-dimensional Riemann tensor $R^i{}_{jkl}$, a Ricci tensor R_{ij}, and a Ricci scalar R (when we need to refer to curvature quantities of the four-dimensional spacetime we will indicate them with a (4); e.g., $^{(4)}R^a{}_{bcd}$). The three dimensional tensors in Σ transform as expected under changes of the spatial coordinates, but not under coordinate changes involving time. Expressions involving spatial tensors are therefore covariant in a restricted sense. These last two points serve to reemphasize that Σ is a Riemannian manifold with a geometric structure independent from that of $\mathcal{M}$.

So far, all curvature quantities have been defined completely in terms of the intrinsic geometry of Σ. In order to make connections between $R^i{}_{jkl}$ and $^{(4)}R^a{}_{bcd}$, we will need a notion of how Σ curves in and is embedded within $\mathcal{M}$. We make this connection by examining how the spatial metric changes as you move from Σ to a neighboring spatial slice in the foliation. Specifically, this is accomplished by Lie dragging γ_{ab} along the normal vector n^a. The extrinsic curvature is defined by

$$K_{ab} \equiv -\frac{1}{2}\mathcal{L}_{\hat{n}}\gamma_{ab} = -\frac{1}{2}(n^c\nabla_c\gamma_{ab} + \gamma_{cb}\nabla_a n^c + \gamma_{ac}\nabla_b n^c).\tag{2.22}$$

Because n^a is timelike, this definition captures the (rough) idea that the extrinsic curvature measures the time rate of change of the spatial metric. It can be shown from this definition that

$$K_{ij} = -\mathbb{P}^a_i\mathbb{P}^b_j\nabla_{(a}n_{b)},\tag{2.23}$$

from which it is apparent that K_{ij} is symmetric and spatial.

The symmetries $^{(4)}R_{abcd} = -^{(4)}R_{bacd}$ and $^{(4)}R_{abcd} = -^{(4)}R_{abdc}$ mean that projecting the Riemann tensor three or more times onto n^b gives zero identically (e.g., $n^a n^b n^{c\,(4)}R_{abcd} = -n^a n^b n^{c\,(4)}R_{bacd}$ necessitates that $n^a n^b n^{c\,(4)}R_{abcd} = 0$). Thus, we consider four spatial projections of $^{(4)}R_{abcd}$ (Gauss's equation), three spatial and one temporal projection of $^{(4)}R_{abcd}$ (Codazzi's equation), and two spatial and two temporal projections of $^{(4)}R_{abcd}$ (Ricci's equation). After some calculation (the details of which are omitted), we find

$$\mathbb{P}^a_i\mathbb{P}^b_j\mathbb{P}^c_k\mathbb{P}^{d\,(4)}_l R_{abcd} = R_{ijkl} + K_{ik}K_{jl} - K_{il}K_{jk} \qquad \text{(Gauss)}\tag{2.24}$$

$$\mathbb{P}_i^b \mathbb{P}_j^a \mathbb{P}_k^c n^{d\,(4)} R_{abcd} = D_i K_{jk} - D_j K_{ik} \qquad \text{(Codazzi)} \qquad (2.25)$$

$$\mathbb{P}_i^d \mathbb{P}_j^b n^c n^{a\,(4)} R_{abcd} = \mathcal{L}_{\hat{n}} K_{ij} + \alpha^{-1} D_i D_j \alpha + K_{ki} K_j{}^k \qquad \text{(Ricci)}. \qquad (2.26)$$

Contracting Gauss's equation twice and Codazzi's equation once gives

$$\gamma^{ac} \mathbb{P}_i^d \mathbb{P}_j^b {}^{(4)} R_{abcd} = R_{ij} + K K_{ij} - K_i{}^k K_{jk} \qquad (2.27)$$

$$\gamma^{ac} \gamma^{bd\,(4)} R_{abcd} = R + K^2 - K^{ij} K_{ij} \qquad (2.28)$$

$$\mathbb{P}_i^b n^d \gamma^{ac\,(4)} R_{abcd} = D_i K - D_j K_i{}^j, \qquad (2.29)$$

where the mean curvature is defined as $K = \text{Tr}(K) = K_i{}^i$.

Define projections of the stress-energy tensor

$$\rho \equiv n^a n^b T_{ab}, \qquad S_i \equiv -\mathbb{P}_i^a n^b T_{ab}, \qquad S_{ij} \equiv \mathbb{P}_i^a \mathbb{P}_j^b T_{ab}, \qquad \text{and} \qquad S \equiv \gamma^{ij} S_{ij}. \qquad (2.30)$$

Also compute projections of the Einstein tensor

$$2 n^a n^b G_{ab} = \gamma^{ac} \gamma^{bd\,(4)} R_{abcd} \qquad \text{and} \qquad \mathbb{P}_i^a n^b G_{ab} = \gamma^{ac} \mathbb{P}_i^b n^{d\,(4)} R_{abcd}. \qquad (2.31)$$

Einstein's equations and Gauss's equation contracted twice (2.28) give the Hamiltonian (or energy) constraint

$$16\pi\rho = 16\pi n^a n^b T_{ab} = 2 n^a n^b G_{ab} = \gamma^{ac} \gamma^{bd\,(4)} R_{abcd} = R + K^2 - K_{ij} K^{ij}. \qquad (2.32)$$

Einstein's equations and Codazzi's equation contracted once (2.29) give the momentum constraint

$$8\pi S_i = -8\pi \mathbb{P}_i^a n^b T_{ab} = -\mathbb{P}_i^a n^b G_{ab} = -\gamma^{ac} \mathbb{P}_i^b n^{d\,(4)} R_{abcd} = D_j K_i{}^j - D_i K. \qquad (2.33)$$

The constraints do not involve time derivatives, instead they relate the variables γ_{ij}, K_{ij}, and their spatial derivatives at all times (again, recall the case of Maxwell's equations where $\vec{\nabla} \cdot \vec{B} = 0$). Noting that both these equations derive from one or more temporal projections of Einstein's tensor it makes sense that they are constraint equations, given the discussion of the Bianchi identity at the beginning of the section.

We now derive the equations governing evolution. We expect our spatial objects γ_{ij} and K_{ij} to evolve along the vector t^a which we found to be a general vector pointing out of Σ. We will therefore want to

calculate $\mathcal{L}_{\hat{t}}\gamma_{ij}$ and $\mathcal{L}_{\hat{t}}K_{ij}$. The first evolution equation is

$$\mathcal{L}_{\hat{t}}\gamma_{ij} = \alpha\mathcal{L}_{\hat{n}}\gamma_{ij} + \mathcal{L}_{\hat{\beta}}\gamma_{ij} = -2\alpha K_{ij} + D_i\beta_j + D_j\beta_i. \tag{2.34}$$

The second involves Ricci's equation

$$\mathcal{L}_{\hat{t}}K_{ij} = \alpha\left(\mathbb{P}_i^d\mathbb{P}_j^b n^a n^{c\,(4)}R_{abcd} - \alpha^{-1}D_iD_j\alpha - K_{ki}K_j^{\ k}\right) + \mathcal{L}_{\hat{\beta}}K_{ij}. \tag{2.35}$$

But Gauss's equation (2.27) and the trace-reverse of Einstein's equations give

$$\mathbb{P}_i^d\mathbb{P}_j^b n^a n^{c\,(4)}R_{abcd} = \gamma^{ac}\mathbb{P}_i^d\mathbb{P}_j^{b\,(4)}R_{abcd} - \mathbb{P}_i^a\mathbb{P}_j^{b\,(4)}R_{ab}$$

$$= R_{ij} + KK_{ij} - K_i^{\ k}K_{jk} - \mathbb{P}_i^a\mathbb{P}_j^b\left(8\pi T_{ab} - 4\pi T g_{ab}\right)$$

$$= R_{ij} + KK_{ij} - K_i^{\ k}K_{jk} - 8\pi S_{ij} + 4\pi\gamma_{ij}\left(S - \rho\right), \tag{2.36}$$

so that

$$\mathcal{L}_{\hat{t}}K_{ij} = \alpha\left(R_{ij} + KK_{ij} - 2K_i^{\ k}K_{jk} - 8\pi S_{ij} + 4\pi\gamma_{ij}\left(S - \rho\right)\right) - D_iD_j\alpha$$

$$+ \beta^k D_k K_{ij} + K_{ik}D_j\beta^k + K_{kj}D_i\beta^k. \tag{2.37}$$

This second evolution equation came from two spatial projections of Einstein's equations, again reflecting the discussion at the beginning of the section on the Bianchi identity. Notice that the six second-order evolution equations have now been recast as twelve first-order evolution equations. The first evolution equation essentially came from the definition of the extrinsic curvature in terms of the Lie derivative of the spatial metric, which we saw before makes the extrinsic curvature something like a time derivative of the spatial metric. This reduction of order in the evolution equations is therefore analogous to reduction of order in the simple system

$$\frac{d^2}{dt^2}x(t) = a(t) \qquad \Rightarrow \qquad \begin{cases} \dfrac{d}{dt}x(t) = v(t) \\[2ex] \dfrac{d}{dt}v(t) = a(t) \end{cases} \tag{2.38}$$

with γ_{ij} playing the part of the coordinate $x(t)$ and K_{ij} the part of the velocity $v(t)$.

In order to treat these equations numerically, a basis must be chosen. We pick a basis where three of the

basis vectors lie in a spatial slice. Therefore, these three basis vectors $(e_i)^a$ satisfy

$$\omega_a (e_i)^a = 0. \tag{2.39}$$

We will also want this basis to be unchanged between slices

$$\mathcal{L}_{\hat{t}}(e_i)^a = 0. \tag{2.40}$$

If both of these desired properties are to hold, we must have

$$0 = \mathcal{L}_{\hat{t}} \left(\omega_a (e_i)^a \right) = (e_i)^a \mathcal{L}_{\hat{t}} \omega_a + \omega_a \mathcal{L}_{\hat{t}}(e_i)^a = (e_i)^a \mathcal{L}_{\hat{t}} \omega_a \tag{2.41}$$

which can only be true in general if $\mathcal{L}_{\hat{t}} \omega_a = 0$, but we see that this is the case

$$\mathcal{L}_{\hat{t}} \omega = \mathcal{L}_{\hat{t}} d\tilde{t} = d \left(\mathcal{L}_{\hat{t}} \tilde{t} \right) = d \left(t^a \nabla_a \tilde{t} \right) = d \left(t^a \omega_a \right) = d \left((\alpha n^a + \beta^a) \left(-\alpha^{-1} n_a \right) \right) = d \left(1 + 0 \right) = 0. \tag{2.42}$$

To complete our basis, we take $(e_0)^a = t^a$. With the definitions of the other three basis vectors, we know $t^a = (1, 0, 0, 0)$ in this basis. Note that

$$\mathcal{L}_{\hat{t}} T_{ab} = t^c T_{ab,c} + T_{ac} t^c{}_{,b} + T_{cb} t^c{}_{,a} = \partial_t T_{ab}. \tag{2.43}$$

It can be shown that the same holds for more general tensors, so $\mathcal{L}_{\hat{t}}$ the Lie derivative along t^a is just a partial derivative with respect to time t in this basis.

In this basis, the following matrix representations for a number of quantities can be found

$$t^a = \begin{pmatrix} 1 \\ 0 \\ 0 \\ 0 \end{pmatrix} \qquad n^a = \alpha^{-1} \begin{pmatrix} 1 \\ -\beta^i \end{pmatrix} \qquad \beta^a = \begin{pmatrix} 0 \\ \beta^i \end{pmatrix}$$

$$n_a = (-\alpha, 0, 0, 0) \qquad \gamma^{ab} = \begin{pmatrix} 0 & 0 \\ 0 & \gamma^{ij} \end{pmatrix} \qquad \gamma_{ab} = \begin{pmatrix} \beta^i \beta_i & \beta_i \\ \beta_j & \gamma_{ij} \end{pmatrix}, \tag{2.44}$$

where $\beta_i \equiv \gamma_{ij} \beta^j$ and γ^{ij} (the inverse spatial metric) is the 3×3 matrix inverse of γ_{ij}. This gives matrix

representations for g_{ab} and g^{ab}

$$g_{ab} = \begin{pmatrix} \beta^i \beta_i & \beta_i \\ \beta_j & \gamma_{ij} \end{pmatrix} - \begin{pmatrix} \alpha^2 & 0 \\ 0 & 0 \end{pmatrix} = \begin{pmatrix} \beta^i \beta_i - \alpha^2 & \beta_i \\ \beta_j & \gamma_{ij} \end{pmatrix} \qquad (2.45)$$

and

$$g^{ab} = \begin{pmatrix} 0 & 0 \\ 0 & \gamma^{ij} \end{pmatrix} - \alpha^{-2} \begin{pmatrix} 1 & -\beta^i \\ -\beta^j & \beta^i \beta^j \end{pmatrix} = \begin{pmatrix} -\alpha^{-2} & \alpha^{-2} \beta^i \\ \alpha^{-2} \beta^j & \gamma^{ij} - \alpha^{-2} \beta^i \beta^j \end{pmatrix}. \qquad (2.46)$$

The line element is

$$\begin{aligned} ds^2 &= \left(-\alpha^2 + \beta^i \beta_i\right) dt^2 + 2\beta_i dx^i dt + \gamma_{ij} dx^i dx^j \\ &= -\alpha^2 dt^2 + \gamma_{ij} \left(dx^i + \beta^i dt\right)\left(dx^j + \beta^j dt\right). \end{aligned} \qquad (2.47)$$

These forms of the line element illustrate again the interpretation of α and β^i as determining the coordinate system (or more specifically, the evolution of the coordinate system in moving from Σ to a nearby spatial slice). It is helpful to think of the lapse as specifying the rate at which time is passing between slices and the shift as describing how the spatial coordinates move from one slice to the next. Between two slices separated by a coordinate time dt, the proper time of an observer moving along the normal n^a increases by an amount αdt and the spatial coordinates shift by an amount $\beta^i dt$. This is shown in Fig. 2.1. Also note that $\alpha^2 = -g/\gamma$.

A few words are in order about the final form of the ADM equations we use. We will now specialize to the case of vacuum where $T_{ab} = 0$ (with the exception of parts of §3.1 and §3.2). We also define H and M_i as shorthands for the Hamiltonian and momentum constraint equations, respectively. These quantities are analytically zero, but are useful to refer to none the less, especially as diagnostics of numerical results. Reproduced together for easy reference, we have our final form for the ADM equations

$$0 = H \equiv R + K^2 - K_{ij} K^{ij} \qquad (2.48a)$$

$$0 = M_i \equiv D_j K_i{}^j - D_i K \qquad (2.48b)$$

$$\partial_t \gamma_{ij} = -2\alpha K_{ij} + D_i \beta_j + D_j \beta_i \qquad (2.48c)$$

$$\partial_t K_{ij} = \alpha \left(R_{ij} + K K_{ij} - 2K_i{}^k K_{jk}\right) - D_i D_j \alpha + \beta^k D_k K_{ij} + K_{ik} D_j \beta^k + K_{kj} D_i \beta^k. \qquad (2.48d)$$

It is worth noting that these derivations can be done from a completely field-theoretic approach starting with the Einstein-Hilbert action (and, in fact, this is how Arnowitt, Deser, and Misner originally derived
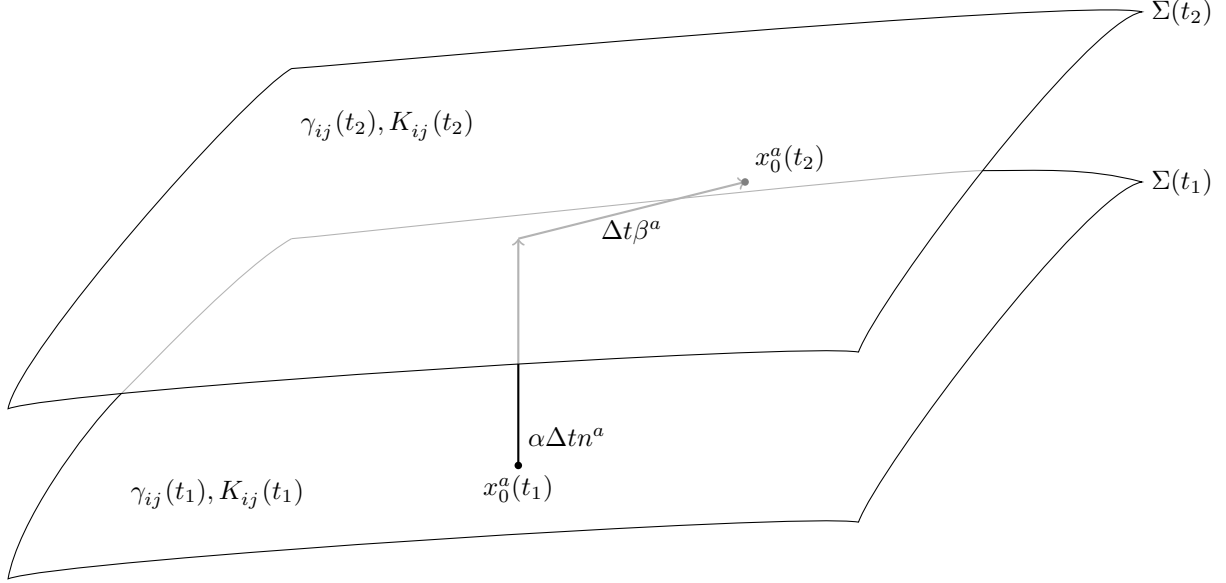
Figure 2.1: The foliation of spacetime. Shown are two moments in time, $\Sigma(t_1)$ and $\Sigma(t_2)$, in the foliation, each with its own γ_{ij} and K_{ij}. The relationship between a point x_0^a in the two members of the foliation in terms of α and β^i also is shown. Analytically, there are an infinite number of such slices; numerically, the code computes quantities at the two times t_1 and t_2 separated by some small Δt.

their formalism [17]). A more geometric approach was taken here (and in e.g., [20, 13, 57]) because it gives helpful insight into how data is evolved from one spatial slice to the next during a simulation. However, the original approach does highlight two important features, reinforcing results obtained here. The first feature is that the extrinsic curvature is related to π^{ij}, the generalized momenta conjugate to γ_{ij}. Thus, the reduction in order we saw earlier comes naturally from a Hamiltonian mechanics approach. Secondly, α and β^i arise as Lagrange multipliers, multiplying H and M_i, respectively. This further emphasizes that they are freely specifiable.

2.1.1: Gauge Choice

Now, contract the evolution equation for the spatial metric (2.48c) using Jacobi's formula

$$\partial_t \ln \gamma = -2\alpha K + 2D_i \beta^i. \tag{2.49}$$

Assume for now that we have chosen a gauge where $\beta^i = 0$. Near the black hole, where $\alpha \approx 0$ (i.e., proper time passes more slowly near the singularity), this tells us that

$$\partial_t \gamma \approx 0. \tag{2.50}$$

This is a desirable property because – if γ does not change near the black hole – then volumes will be preserved and a coordinate singularity is avoided. If the volume were to become too small, freely falling observers would "crash" into each other. Therefore, we can demand the lapse satisfy the equation

$$\partial_t \alpha = -2\alpha K \tag{2.51}$$

to drive the term $2\alpha K$ toward zero and achieve this. Integrating (2.51) gives

$$\alpha = 1 + \ln \gamma. \tag{2.52}$$

Hence, the condition (2.51) is called '1+log' slicing [20].

A common choice for fixing one of the four coordinate choices is a slight modification of (2.51) where an advection term is added

$$\left(\partial_t \alpha - \beta^i \partial_i\right) = -2\alpha K \tag{2.53}$$

(which is also commonly called 1+log slicing). The common choice for fixing the other three is the 'Γ-driver' condition

$$\left(\partial_t - \beta^j \partial_j\right)\beta^i = \frac{3}{4}B^i \tag{2.54a}$$

$$\left(\partial_t - \beta^j \partial_j\right)B^i = \left(\partial_t - \beta^j \partial_j\right)\tilde{\Gamma}^i - \eta B^i, \tag{2.54b}$$

where η is a constant and the notation $\tilde{\Gamma}^i$ will be explained in §2.3 [20]. Seeing as these are differential gauge conditions, there is an additional freedom where initial α, β^i, and $\partial_t \beta^i$ must be specified. Of course, the somewhat simplistic conclusions reached in the previous paragraph were obtained using (2.51) and $\beta^i = 0$ instead of the actual gauge we will use given by (2.53) and (2.54). However, choosing (2.53) and (2.54) as gauge conditions in numerical relativity has been found to yield very stable evolutions, reflecting the qualitative features described above.

Section 2.2:   Trumpet Spatial Slice Topology

In motivating our analysis in Chapter 5, it will important to understand the topology of Σ and how it slices $\mathcal{M}$. We will seek a type of topology which is referred to as 'trumpet slicing.' The features of trumpet slices are well laid out in [25, 26] where simple analytic trumpet conditions are used to investigate some of their important properties. Before investigating trumpets in a rigorous way, we look at their general

properties by considering a fairly simple example.

Consider the Schwarzschild line element written in Schwarzschild coordinates[1]

$$ds^2 = -f d\bar{t}'^2 + f^{-1} dR^2 + R^2 d\Omega^2, \tag{2.55}$$

where $f \equiv 1 - 2M/R$ and $d\Omega^2 \equiv d\theta^2 + \sin^2\theta d\phi^2$. Now make a coordinate change by adding a height function $h(R)$ to the time coordinate

$$t' = \bar{t}' - h(R). \tag{2.56}$$

In the new coordinate system

$$ds^2 = -f \left(dt' + h'(R) dR \right)^2 + f^{-1} dR^2 + R^2 d\Omega^2. \tag{2.57}$$

For our purposes, $h(R)$ is generally chosen so that it diverges at some $r_0 > 0$ to get trumpet slicing.

Embedding diagrams for spatial slices in these two coordinate systems are shown in Fig. 2.2. Firstly, imagining rotating the curves in Fig. 2.2b around the $\bar{t}'$-axis gives some indication of why the word "trumpet" was chosen. Secondly, note that the curves in Fig. 2.2b do not intersect the singularity at $R = 0$. This will prove to be one of the most important features of trumpet slicing. It is a natural way to "hide the singularity from the computer." It is shown very nicely in [30] that the 1+log and Γ-driver gauge choices drive spatial slices to trumpet slicing (see especially their Fig. 15), yielding insight into why this gauge choice is so numerically stable.

For completeness, corresponding Penrose diagrams are shown in Fig. 2.3, in which the same properties can also be seen. In summary, trumpet slicing involves the following:

1. The trumpet slice must limit on a sphere with non-zero area (viewed on an embedding diagram with one spatial dimension suppressed, it limits on a circle with non-zero circumference).

2. The trumpet does not intersect the singularity.

There exists a 2+1 decomposition [26] where Σ is foliated into level sets of a radial function $r(\theta, \phi)$. A member of this foliation $\mathcal{S}$ is a Riemannian manifold with metric q_{AB} and is diffeomorphic to a 2-sphere. There is also a "lapse" $\sigma = \sqrt{\gamma/q}$ relating radial movement off of $\mathcal{S}$ to the radial normal vector $s_i = (\sigma, 0, 0)$ and a "shift" vector ω^A. The relationship between the spatial metric γ_{ij} and the spherical metric q_{AB} is

---

[1]The overbars and primes are a notation we will find helpful in Chapter 5.
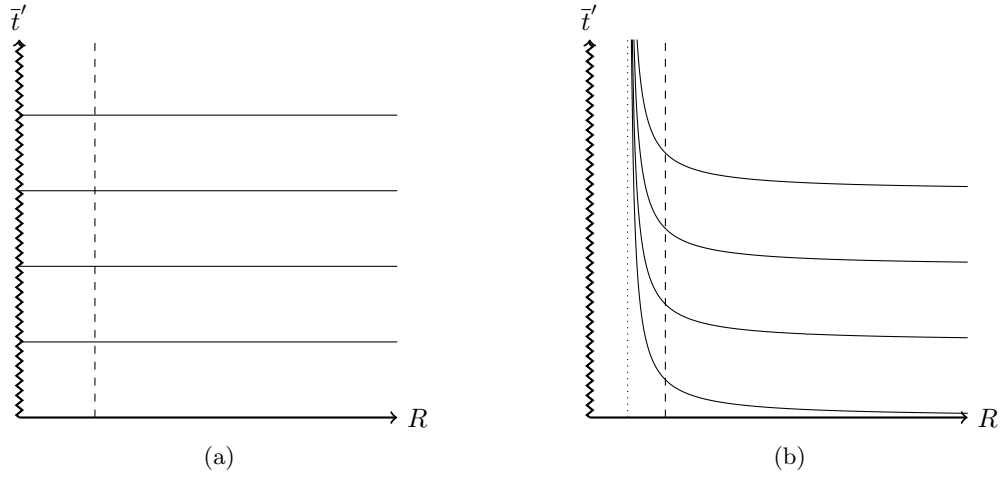
Figure 2.2: Embedding diagrams for the Schwarzschild spacetime. Showing level sets of $\bar{t}'$ in the $\bar{t}'R$-plane on the left and level sets of t' in the $\bar{t}'R$-plane on the right (with solid lines). The singularity at $R = 0$ is shown with a zigzag line and the horizon at $R = 2M$ is shown with a dashed line. The limiting radius of the trumpet slices $R = r_0$ is shown by the dotted line in the right figure. The flat slices (on the left) intersect the singularity after entering the horizon; in contrast, the trumpet slices (on the right) enter the horizon but limit on r_0 (the dotted line) instead of intersecting the singularity. Note that these are schematic diagrams only and were drawn without using a practical a height function $h(R)$.
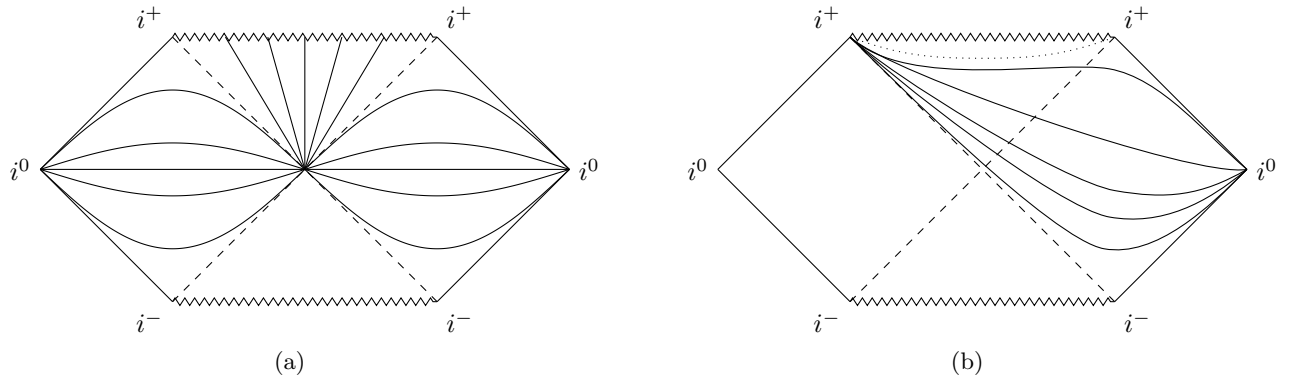
Figure 2.3: Penrose diagrams for the Schwarzschild spacetime. Showing surfaces of constant $\bar{t}'$ on the left and surfaces of constant t' on the right (solid lines). The singularity at $R = 0$ is shown with a zigzag line and the horizon at $R = 2M$ is shown with a dashed line. The limiting radius of the trumpet slices $R = r_0$ is shown by the dotted line in the right figure (these are the same conventions used in Fig. 2.2). The flat slices (on the left) either enter the parallel universe or intersect the singularity; in contrast, the trumpet slices (on the right) enter the horizon and terminate on i^+ without crossing r_0 (the dotted line). Note that these are schematic diagrams only and were drawn without using a practical height function $h(R)$.

18

$q_{ab} = \gamma_{ab} - s_a s_b$

$$\gamma_{ij} = \begin{pmatrix} \omega_A \omega^A + \sigma^2 & \omega_A \\ \omega_B & q_{AB} \end{pmatrix}. \tag{2.58}$$

The spatial line element is

$$dl^2 = \sigma^2 dR^2 + q_{AB} \left(d\theta^A + \omega^A dR \right) \left(d\theta^B + \omega^B dR \right). \tag{2.59}$$

Note though that there is an important difference in sign which stems from difference in signatures of g_{ab} and γ_{ij} (i.e., $\mathcal{M}$ is pseudo-Riemannian and Σ is Riemannian).[2] Just as spatial objects effectively contained no independent temporal component, angular objects contain no independent radial component; we will again be somewhat relaxed in which set of indices we use when discussing them.

This decomposition is used by [26] to give rigor to the desired properties listed above; for a trumpet with limiting radius r_0 these are:

1. A spherical surface $\mathcal{S}$ which is a level set with $R = r_0$ has a positive area (where $A_\mathcal{S} = \int \sqrt{q} d\theta d\phi$). This can be assured by $q > 0$ at r_0.

2. A spherical surface $\mathcal{S}$ which is a level set with $R = r_0$ must be an infinite distance from the singularity. Given that radial distance is measured by $dl = \sigma dr$, σ must diverge at r_0.

We will see in Chapter 5 that at $R = r_0$ for our choice of trumpet σ diverges while q remains finite, thus reinforcing that we really will have found trumpet slicing.

Section 2.3:   Conformal Transformations

This section first considers why and how we carry out conformal transformations. We then give an overview of how a conformal transformation is used to construct the initial data which has been used by almost all finite difference based numerical relativity simulations.

The four constraint equations (2.48a) and (2.48b) must be solved to obtain initial data for γ_{ij} and K_{ij}. Of course, four equations are not enough to determine the twelve independent components of these two tensors. Apparently, we are free to choose eight of the twelve components and the other four are then determined by the constraints. But which four should we single out to solve for? One answer, to try to keep the various

---

[2]There is also the additional complication that we typically consider γ_{ij} in Cartesian-like coordinates and q_{AB} in spherical coordinates, so there is a coordinate transformation we have swept under the rug above.

components on equitable footing, is doing a conformal transformation

$$\gamma_{ij} = \psi^4 \tilde{\gamma}_{ij}. \tag{2.60}$$

We call $\tilde{\gamma}_{ij}$ the 'conformal (spatial) metric.' In general, a tilde signals that a quantity is conformally related; for example, $\tilde{\Gamma}^i$ in (2.54) is the contraction of connection coefficients computed from the conformal metric

$$\tilde{\Gamma}^i = \tilde{\gamma}^{jk} \tilde{\Gamma}^i{}_{jk} = \tilde{\gamma}^{jk} \frac{1}{2} \tilde{\gamma}^{il} \left(\tilde{\gamma}_{lk,j} + \tilde{\gamma}_{jl,k} - \tilde{\gamma}_{jk,l} \right). \tag{2.61}$$

Such a transformation preserves angles, but that is not what motivates us to do it. If we pick the $\tilde{\gamma}_{ij}$ then solve for ψ we have not had to single out any components over the others. In order to not introduce an extra degree of freedom, we demand that $\tilde{\gamma} = 1$ (and, as a consequence, $\gamma^{1/3} = \psi^4$). The five algebraically independent components of $\tilde{\gamma}_{ij}$ along with ψ together equal the six independent components of γ_{ij}.

Decomposition of the extrinsic curvature is done so that we are able to pick three of the six components. First, the trace is removed

$$A_{ij} \equiv K_{ij} - \frac{1}{3} \gamma_{ij} K, \tag{2.62}$$

then a conformal rescaling is carried out on the trace-free part of the extrinsic curvature

$$A_{ij} = \psi^{-2} \tilde{A}_{ij}. \tag{2.63}$$

Finally, this is broken into transverse and longitudinal parts

$$\tilde{A}^{ij} = \tilde{A}^{ij}_{TT} + \tilde{A}^{ij}_L. \tag{2.64}$$

The longitudinal part comes from the gradient of a potential vector

$$\tilde{A}^{ij}_L = \left(\tilde{\mathbb{L}} W \right)^{ij} \equiv \tilde{D}^i W^j + \tilde{D}^j W^i - \frac{2}{3} \tilde{\gamma}^{ij} \tilde{D}_k W^k. \tag{2.65}$$

The vector potential accounts for three of the five degrees of freedom of $\tilde{A}_{ij}$, meaning the remaining part, $\tilde{A}^{ij}{}_{TT}$, must have two degrees of freedom. We can remove these three degrees of freedom from $\tilde{A}^{ij}$ using a divergence condition

$$\tilde{D}_i \tilde{A}^{ij}_{TT} = 0. \tag{2.66}$$

Table 2.1 summarizes the distribution of the twelve total degrees of freedom of the initial data.

Variable	Degrees of Freedom	Variable	Degrees of Freedom
γ_{ij}	6	$\tilde{\gamma}_{ij}$	5
		ψ	1
K_{ij}	6	K	1
		W^i	3
		$\tilde{A}_{TT}^{ij}$	2
Total	12	Total	12

Table 2.1: Table summarizing the information content of the the pieces of conformal transverse-traceless decomposition.

Plugging these definitions into the constraint equations yields

$$0 = 8\tilde{D}^2\psi - \tilde{R}\psi - \frac{2}{3}K^2\psi^5 + \tilde{A}_{ij}\tilde{A}^{ij}\psi^{-7} \tag{2.67a}$$

$$0 = \left(\tilde{\Delta}_{\mathbb{L}}W\right)^i - \frac{2}{3}\psi^6\tilde{\gamma}^{ij}\tilde{D}_j K, \tag{2.67b}$$

where the vector Laplacian is defined by

$$\left(\tilde{\Delta}_{\mathbb{L}}W\right)^i \equiv \tilde{D}^2 W^i + \frac{1}{3}\tilde{D}^i\tilde{D}_j W^j + \tilde{R}^i{}_j W^j. \tag{2.68}$$

The Hamiltonian constraint then becomes an equation for ψ and the momentum constraint is an equation for W^i (though they are coupled). Freely specifiable parameters are $\tilde{\gamma}_{ij}$, K, and $\tilde{A}_{TT}^{ij}$. The decomposition outlined above is called the 'conformal transverse-traceless' decomposition (described in e.g., [57]).

If we choose $K = 0$ and $\tilde{\gamma}_{ij} = \delta_{ij}$, these equations will simplify immensely. Choosing $K = 0$ – referred to as 'maximal slicing' – removes the dependence of W^i on ψ. Choosing $\tilde{\gamma}_{ij} = \delta_{ij}$ – referred to as 'conformal flatness' – reduces all covariant derivatives to partial derivatives. The 'Bowen-York formalism' constructs maximally sliced, conformally flat initial data. This decomposition forms the basis for the canonical method of posing initial data for black hole simulations in the Einstein Toolkit. The equations become

$$0 = \Delta\psi + \frac{1}{8}\tilde{A}_{ij}\tilde{A}^{ij}\psi^{-7} \tag{2.69a}$$

$$0 = \Delta W^i + \frac{1}{3}\partial^i\partial_j W^j, \tag{2.69b}$$

where $\Delta \equiv \partial_x^2 + \partial_y^2 + \partial_z^2$ is the flat space Laplacian. Notably, the momentum constraint is now not only decoupled from the Hamiltonian constraint, it is also linear in W^i. Solutions include

$$W^i = \frac{1}{r^2}\varepsilon^{ijk}l_j J_k \tag{2.70}$$

and

$$W^i = -\frac{1}{4r} \left(7P^i + l^i l_j P^j \right), \tag{2.71}$$

where $r^2 = x^2 + y^2 + z^2$ and $l^i = l_i = x^i/r$ and J_i and P^i are constant vectors. There is only one equation (2.69a) left to solve, though it is non-linear and must be solved numerically. Initial data constructed by substituting (2.70) into (2.69a) yields a black hole with spin J_i. Initial data constructed with (2.71) yields a black hole with momentum P^i.

One of the most powerful features of this formalism is that the linearity of (2.69b) allows us to add multiple solutions for W^i to get a black hole with both spin and momentum. Or, offsetting the origins, we can get multiple black holes. In practice, when solving for the divergent ψ it is common to "put the divergences in by hand" near the black holes and solve for a correction factor u which is regular. In particular, for two black holes with mass parameters M_1 and M_2 and singularities at $\vec{r}_1$ and $\vec{r}_2$,

$$\psi = 1 + \frac{M_1}{2\left|\vec{r} - \vec{r}_1\right|} + \frac{M_2}{2\left|\vec{r} - \vec{r}_2\right|} + u. \tag{2.72}$$

These second and third terms are referred to as the 'punctures' associated with each of the black holes.

Thus, in the Bowen-York initial data formalism, dealing with the non-linearities of general relativity comes down to solving the single non-linear elliptic equation (2.69a). The choices made for Bowen-York initial data were mathematically motivated. It yields data which satisfies Einstein's equations, but is not quite the physical situation one might hope for. Bowen-York black holes are initially distorted and at the beginning of a simulation transient gravitational radiation is released that is referred to as 'junk radiation.' The junk radiation not only may overlap and confuse the eventual physically realistic gravitational wave signal, but can also perturb the mass, momentum, and angular momentum of the black holes (e.g., the masses of the black holes in (2.72) shortly after the beginning of the simulation will not be M_1 and M_2).

Other, more general approaches are being explored more fully (e.g., [34, 46], among others). Some choice is made for the free parts of the initial data for one black hole. Multiple copies of the data for a single black hole are then added together and the constraint equations are solved; e.g., as in (2.72), the constraint is solved for the correction u, but with a different choice for the singular part of ψ. The choices in recent work are more physically motivated, but this comes at the expense of having to solve more complicated versions of (2.67).

2.3.1:   BSSN Equations: Conformal Rescaling of the Evolution Equations

It turns out to also be advantageous to make use of the conformal decomposition for the purposes of evolution. This results in the BSSN equations, named for Baumgarte, Shapiro, Shibata, and Nakamura [20, 32]. The BSSN of the evolution equations is strongly hyperbolic whereas the combination of (2.48c) and (2.48d) is not. This yields much better stability. Part of how strong hyperbolicity is achieved is by promoting the quantities

$$\tilde{\Gamma}^i \equiv \tilde{\gamma}^{jk} \tilde{\Gamma}^i{}_{jk} \tag{2.73}$$

to independent (albeit constrained by their definition (2.73)) variables. Additionally, to ease numerical difficulties near the location of the black hole singularity, an alternative conformal factor is often evolved instead of ψ

$$e^{4\phi} = \psi^4. \tag{2.74}$$

The standard form for the BSSN equations (without sources) is[3] [32]

$$\partial_0 \phi = -\frac{1}{6} \alpha K + \frac{1}{6} \partial_i \beta^i \tag{2.75a}$$

$$\partial_0 \tilde{\gamma}_{ij} = -2\alpha \tilde{A}_{ij} + \tilde{\gamma}_{ik} \partial_j \beta^k + \tilde{\gamma}_{jk} \partial_i \beta^k - \frac{2}{3} \tilde{\gamma}_{ij} \partial_k \beta^k \tag{2.75b}$$

$$\partial_0 K = -\tilde{\gamma}^{ij} \left[\tilde{D}_j \tilde{D}_i \alpha + 2 \left(\partial_i \phi \right) \left(\partial_j \alpha \right) \right] + \alpha \left(\tilde{A}_{ij} \tilde{A}^{ij} + \frac{1}{3} K \right) \tag{2.75c}$$

$$\partial_0 \tilde{A}_{ij} = e^{-4\phi} \left[\alpha \tilde{R}_{ij} + \alpha R^\phi_{ij} - \tilde{D}_j \tilde{D}_i \alpha - 2 \left(\partial_i \phi \right) \left(\partial_j \alpha \right) \right]^{\text{TF}} + \alpha \left(K \tilde{A}_{ij} - 2 \tilde{A}_{il} \tilde{A}^l{}_j \right)$$
$$+ \tilde{A}_{ik} \partial_j \beta^k + \tilde{A}_{jk} \partial_i \beta^k - \frac{2}{3} \tilde{A}_{ij} \partial_k \beta^k \tag{2.75d}$$

$$\partial_0 \tilde{\Gamma}^i = -2\tilde{A}^{ij} \partial_j \alpha + 2\alpha \left(\tilde{\Gamma}^i{}_{jk} \tilde{A}^{kj} - \frac{2}{3} \tilde{\gamma}^{ij} \partial_j K + 6 \tilde{A}^{ij} \partial_j \phi \right)$$
$$- \tilde{\Gamma}^j \partial_j \beta^i + \frac{2}{3} \tilde{\Gamma}^i \partial_j \beta^j + \frac{1}{3} \tilde{\gamma}^{il} \partial_j \partial_l \beta^j + \tilde{\gamma}^{jl} \partial_j \partial_l \beta^i, \tag{2.75e}$$

where

$$\tilde{R}_{ij} = \tilde{\gamma}^{lm} \left(-\frac{1}{2} \partial_l \partial_m \tilde{\gamma}_{ij} + 2 \tilde{\Gamma}^k{}_{l(i} \tilde{\Gamma}_{j)km} + \tilde{\Gamma}^k{}_{im} \tilde{\Gamma}_{klj} \right) + \left(\tilde{\gamma}_{k(i} \partial_{j)} + \tilde{\Gamma}_{(ij)k} \right) \tilde{\Gamma}^k, \tag{2.76}$$

$$R^\phi_{ij} = -2 \left(\tilde{D}_i \tilde{D}_j \phi + \tilde{\gamma}_{ij} \tilde{\gamma}^{lm} \tilde{D}_l \tilde{D}_m \phi \right) + 4 \left[\left(\tilde{D}_i \phi \right) \left(\tilde{D}_j \phi \right) - \tilde{\gamma}_{ij} \tilde{\gamma}^{lm} \left(\tilde{D}_l \phi \right) \left(\tilde{D}_m \phi \right) \right], \tag{2.77}$$

$\partial_0 \equiv \partial_t - \beta^m \partial_m$, and the subscript TF indicates the trace-free part of a tensor (e.g., $R^{\text{TF}}_{ij} = R_{ij} - \frac{1}{3} \gamma_{ij} R$).

In summary, the system (2.53), (2.54), and (2.75) is evolved subject to the constraints (2.67) and (2.73).

---

[3]The BSSN formalism uses $A_{ij} = \psi^4 \tilde{A}_{ij}$ instead of (2.63), so a tilde on A_{ij} means something slightly different in (2.75).

CHAPTER 3: Measuring Properties of Black Holes and Spacetimes

In this Chapter, we will investigate energy and gravitational waves in flat spacetime in order to construct diagnostics that are applicable to our simulations. First, we develop the ADM measures of mass, momentum, and angular momentum [17, 20, 13]. In the next section, we consider a notion of horizon that is applicable in simulations and how it can be connected to properties of the black hole. The third section establishes properties of the Weyl scalars so that in the fourth and final section we are able to link quantities measurable in simulations with gravitational wave content.

Throughout this Chapter, we will consider metrics which are perturbations of the Minkowski metric η_{ab}

$$g_{ab} = \eta_{ab} + {}^{(1)}h_{ab} + {}^{(2)}h_{ab} + \mathcal{O}\left(h^3\right), \tag{3.1}$$

where ${}^{(1)}h_{ab}$ and ${}^{(2)}h_{ab}$ are first- and second-order corrections, respectively.[1] Note that there will be two types of second-order terms in the perturbation expansions we consider

$$ {}^{(1)}h_{ab}\, {}^{(1)}h_{cd} = \mathcal{O}\left(h^2\right) \tag{3.2a}$$

$$ {}^{(2)}h_{ab} = \mathcal{O}\left(h^2\right). \tag{3.2b}$$

We will also need a 'null tetrad.' This is an orthonormal basis at all events in a spacetime with all four basis vectors being null (i.e., have zero norm). The usual choice for a null tetrad is adapted to spherical coordinates. The first two vectors of the null tetrad,

$$k^a = \frac{1}{\sqrt{2}}\left(\hat{t}^a + \hat{r}^a\right) \qquad \text{and} \qquad l^a = \frac{1}{\sqrt{2}}\left(\hat{t}^a - \hat{r}^a\right), \tag{3.3}$$

correspond to the radially outgoing and ingoing null directions, where $\hat{t}^a$, $\hat{r}^a$, $\hat{\theta}^a$, and $\hat{\phi}^a$ are the orthonormal basis vectors of the spherical coordinate system. With these two basis vectors chosen, it may not be immediately clear how it is possible to identify other null directions. However, the complex vectors

$$m^a = \frac{1}{\sqrt{2}}\left(\hat{\theta}^a + \imath\hat{\phi}^a\right) \qquad \text{and} \qquad \overline{m}^a = \frac{1}{\sqrt{2}}\left(\hat{\theta}^a - \imath\hat{\phi}^a\right), \tag{3.4}$$

---

[1]Do not confuse the expansion order prefixes (1) and (2) with the spacetime dimension prefix (4) (e.g., ${}^{(4)}R_{abcd}$); this should not be an issue as we will never go beyond second-order when expanding the metric.

where the bar denotes complex conjugation, allow us to complete the null tetrad. Notice that $l^a k_a = -1$ and $m^a \overline{m}_a = 1$ with all other possible inner products of the null tetrad basis vectors equaling zero.

Section 3.1:   ADM Mass, Momentum, and Angular Momentum

In this section, we look at how the constraint equations give notions of mass, momentum, and angular momentum contained within a spatial slice. A concrete example of their use is then presented to provide insight into some of the properties of the ADM quantities relevant to their application in numerical settings.

A local definition of energy is a notoriously difficult thing to develop in general relativity [13, 40]. The problem is that T_{ab} does not take into account the energy of the gravitational field itself. However, the constraint equations (2.32) and (2.33) relate the energy and momentum densities of matter within a spacetime to the configuration of the gravitational field

$$16\pi\rho = H = R + K^2 - K_{ij}K^{ij} \tag{3.5a}$$

$$8\pi S_i = M_i = D_j K_i{}^j - D_i K. \tag{3.5b}$$

Focusing on the Hamiltonian constraint in the regime where the gravitational field is weak, the total energy in some volume of space is approximated by the integral of the energy density. Let us see how we can make a "measurement" of the energy in a gravitational field far from any gravitational sources. The total energy of matter contained in a volume V is

$$\int_V \rho\sqrt{\gamma}dV = \frac{1}{16\pi}\int_V H\sqrt{\gamma}dV. \tag{3.6}$$

Assuming gravity is weak within V we do an expansion of H, dropping terms of order $\mathcal{O}\left(h^2\right)$, the relevant pieces of which are

$$R = {}^{(1)}h^{ij}{}_{,ij} - \delta^{ij}{}^{(1)}h^k{}_{k,ij} \tag{3.7}$$

$$K_{ij} = \frac{1}{2}\left({}^{(1)}h_{i0,j} + {}^{(1)}h_{j0,i} - {}^{(1)}h_{ij,0}\right). \tag{3.8}$$

We recognize that parts of the Hamiltonian constraint are quadratic in the extrinsic curvature and therefore quadratic in the metric perturbation and therefore can be ignored at first order. Additionally, with the Ricci scalar already first order in the metric perturbation, all perturbations to the volume element can be dropped

$$\int_V \rho\sqrt{\gamma}dV = \frac{1}{16\pi}\int_V \left({}^{(1)}h^{ij}{}_{,ij} - \delta^{ij\,(1)}h^k{}_{k,ij} + \mathcal{O}\left(h^2\right)\right)dV \tag{3.9a}$$

$$= \frac{1}{16\pi}\int_V \left({}^{(1)}h^{ij}{}_{,i} - \delta^{ij\,(1)}h^k{}_{k,i} + \mathcal{O}\left(h^2\right)\right)_{,j}dV, \tag{3.9b}$$

where we have recognized that the integrand is a total divergence. Gauss's Law allows us to convert this volume integral into a surface integral

$$\int_V \rho\sqrt{\gamma}dV = \frac{1}{16\pi}\int_{\partial V} \left({}^{(1)}h^{ij}{}_{,i} - \delta^{ij\,(1)}h^k{}_{k,i} + \mathcal{O}\left(h^2\right)\right)ds_j. \tag{3.10}$$

Performing this surface integral far from any gravitational sources is how we "measure" the energy contained within the surface. In particular, if we push the surface all the way to infinite radius, we can find the total mass-energy on Σ. If the next correction after ${}^{(1)}h_{ij}$ falls off faster than r^{-1}, then the neglected second-order terms will tend to zero faster than the area element of the integral grows, and the formula will become exact, independent of the perturbation order

$$M_{\mathrm{ADM}} = \frac{1}{16\pi}\int_{\partial \Sigma} \left(\delta^{ik\,(1)}h_{kj,i} - {}^{(1)}h^i{}_{i,j}\right)ds^j. \tag{3.11}$$

The same arguments hold and we can define the total momentum content of Σ by integrating M_i

$$P^i_{\mathrm{ADM}} = \frac{1}{8\pi}\int_{\partial \Sigma} \left(K^i{}_j - \delta^i_j K\right)ds^j. \tag{3.12}$$

There is of course also an angular momentum measure

$$J^i_{\mathrm{ADM}} = \frac{1}{8\pi}\int_{\partial \Sigma} \varepsilon^{ijk}x_j \left(K_{kl} - \delta_{kl}K\right)ds^l. \tag{3.13}$$

These quantities are referred to as the ADM mass, momentum, and angular momentum due to their connection with the ADM decomposition. Again, although we have taken a geometric approach to understanding them here, they are also derivable from a field-theoretic approach [40]. Though we started with an assumption of an almost flat spacetime, the final forms in terms of surface integrals only require that the spacetime be asymptotically flat (i.e., flat in the region where we evaluate the surface integral). The black hole spacetimes we will be simulating are asymptotically flat, and so we can make use of the ADM mass and linear momentum estimates.

To see an example of how this works, consider the Schwarzschild spacetime written in Kerr-Schild coor-

dinates

$$g_{ab} = \eta_{ab} + \frac{2M}{r} l_a l_b, \tag{3.14}$$

where $l_a = l^a = (1, x/r, y/r, z/r)$ and $r^2 = x^2 + y^2 + z^2$. The metric perturbation is

$$^{(1)}h_{ij} = \frac{2M}{r^3} x_i x_j. \tag{3.15}$$

With $ds^j = l^j r^2 d\Omega^2 = \frac{x^j}{r} r^2 \sin\theta d\theta d\phi = r x^j \sin\theta d\theta d\phi$,

$$M_{\text{ADM}} = \frac{1}{16\pi} \int_{\partial\Sigma} \left(\frac{4M}{r^3} x_j \right) r x^j \sin\theta d\theta d\phi = \lim_{r\to\infty} \frac{M}{4\pi} \int_{\mathcal{S}(r)} \sin\theta d\theta d\phi = \lim_{r\to\infty} M = M. \tag{3.16}$$

For us, it is important to stop and consider the result obtained before doing the limit when carrying out these calculations. As stated above, under certain conditions on $^{(1)}h_{ij}$, the final limit does not depend the perturbation theory order of the integrand. In simulations though, we will need to know not only the limiting value but also how this limiting value is approached. We will not be able to simulate all the way to spatial infinity, the only place where the ADM measures are valid. So instead, we compute the surface integrals at a number of radii in the finite simulation domain and compare with the asymptotic behavior of the analytic expression before the limit is taken to approximate the value of the "numerical limit."

It may initially seem bizarre that a non-zero answer was obtained for a vacuum spacetime ($\rho = 0$) which satisfies the constraint equations ($H = 0$). How can (3.9a), an integral over zero, be non-zero? The answer lies in how we handled Gauss's Law in obtaining (3.10). In the Kerr-Schild example above, a spatial slice of the Schwarzschild spacetime is topologically $\mathbb{R}^3 \setminus \{0\}$. The singularity is not actually a point on the manifold and there is a boundary which we neglected. The integral of H over this inner boundary is $-M$ and the total integral is indeed zero. However, the example above should motivate the utility in computing only one of the boundary terms. We will return to this at the end of §3.2.

Section 3.2: Black Hole Horizons and Quasi-Local Measures

In this section we consider horizons. We will discuss why event horizons are troublesome in numerical simulations then define an 'apparent horizon,' which is more compatible with simulations. Finally, we will link measurements made on the horizon with properties of the black hole.

An event horizon is a global property of a spacetime. An outgoing photon on the event horizon will never reach null infinity. It is possible to use this property to attempt to locate an event horizon in a simulation. By launching photons radially outward from many spatial locations at many times, and tracking which make

it to the spatial boundary of the simulation, an approximate sense of the location of the event horizon can be found. If one accepts these limitations of measuring event horizons numerically, null geodesics can be integrated throughout the simulation and the event horizon can be found in post-processing. Even so, this leaves much to be desired. For instance, having knowledge of horizons during the simulation gives diagnostics about the masses of the black holes, signals merger and the formation of a single large black hole, and – when a horizon cannot be found – an indication that instabilities are developing.

There are, however, other types of horizons, which can be found during numerical simulations. Apparent horizons only require information on one spatial slice (in other words, at one instant). A 'trapped surface' is a surface $\mathcal{S}$ in Σ on which the expansion of outgoing null geodesics is non-positive. Drawing on the 2+1 decomposition outlined near (2.59), the expansion can be expressed mathematically as

$$\Theta \equiv q^{ab} \nabla_a u_b, \tag{3.17}$$

where $u_b \equiv \frac{1}{\sqrt{2}} (n_b + s_b)$ is an outgoing null vector (though it is unequal to k_b if $\mathcal{S}$ is not a level set of the radial coordinate) and $q_{ab} = g_{ab} + n_a n_b - s_a s_b$ (compare (2.19)). An apparent horizon is the outermost trapped surface of a region and is the limiting case where $\Theta = 0$ [27, 48, 20]. See Fig. 3.1. As an example, null rays near a Schwarzscild black hole in Schwarzschild coordinates have an expansion given by

$$\Theta = \frac{\sqrt{2}}{r} \sqrt{1 - \frac{2M}{r}}; \tag{3.18}$$

so there is an apparent horizon when $r = 2M$. Because the black hole is static, the event horizon and apparent horizon coincide.

Consider now the collection of apparent horizons at all times $\mathcal{H}$ so that $\mathcal{S} = \Sigma \cap \mathcal{H}$. This is a three dimensional surface. It is shown in [27] that $\mathcal{H}$ must be a null surface if no matter or radiation is crossing it and spacelike otherwise. In the first case it is called a 'nonexpanding horizon' and in the latter it is called a 'dynamical horizon.' Generally in simulations, there is gravitational radiation and horizons will be dynamical. In this case at least, all the tools developed for analyzing spacelike surfaces in §3.1 are applicable. We can therefore get a quasi-local measure of a black hole's mass, momentum, and angular momentum by doing integrals over the apparent horizon. This has the advantage that it is sensitive to an individual black hole's properties, whereas the ADM measurements carried out at infinity measure the content of the entire universe, including all black holes and radiation. It is also shown in [27] that the extrinsic curvature of $\mathcal{H}$ and normal of $\mathcal{S}$ within $\mathcal{H}$, etc. showing up in the integral over $\mathcal{S}$ can be replaced with the corresponding quantities from Σ. This means that $\mathcal{H}$ does not have to be found during a simulation, and the quasi-local
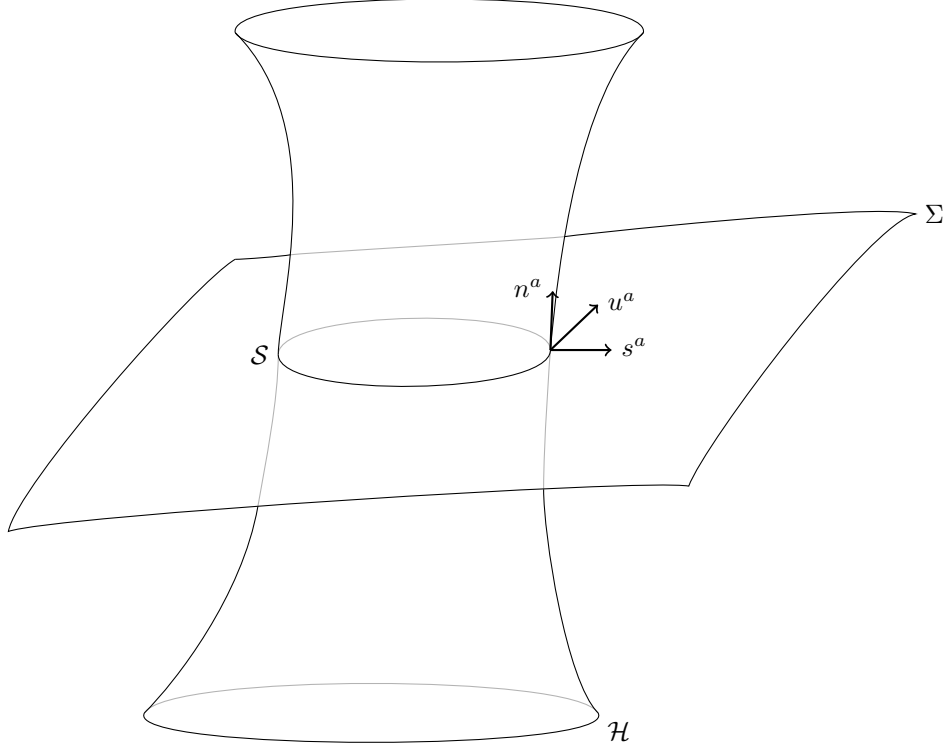
Figure 3.1: Horizon geometry. This shows the spatial slice Σ, the collection of horizons at all times $\mathcal{H}$, and their intersection $\mathcal{S} = \Sigma \cap \mathcal{H}$. It also shows n^a, the normal to Σ; s^a, the normal to $\mathcal{S}$ within Σ; and u^a, the outgoing null vector constructed from n^a and s^a and used in (3.17).

measures on the apparent horizon can be found using data on Σ.

There is one difference however: for the ADM quantities we computed in §3.1 $\hat{\phi}^A$ is a Killing vector in the surface $\partial\Sigma$ on which the integrals are done, but will not generally be a Killing vector on the apparent horizon $\mathcal{S}$. This modifies the formula for angular momentum slightly; the magnitude is given by

$$J_{\mathcal{S}} = \frac{1}{8\pi} \int_{\mathcal{S}} K_{ij}\xi^i ds^j, \tag{3.19}$$

where ξ^i is the Killing vector field on $\mathcal{S}$ (satisfying $\mathcal{L}_{\bar{\xi}}q_{ij} = 0$). Compare this with the magnitude of the ADM angular momentum

$$J^\phi_{\text{ADM}} = \frac{1}{8\pi} \int_{\partial\Sigma} \left(K_{ij} - \delta_{ij}K \right) \hat{\phi}^i ds^j = \frac{1}{8\pi} \int_{\partial\Sigma} K_{ij}\hat{\phi}^i ds^j \tag{3.20}$$

(where the second term drops out because the azimuthal and radial unit vectors are orthogonal).

It is a standard result that

$$M_{\mathcal{S}} = \frac{1}{R_{\mathcal{S}}}\sqrt{R_{\mathcal{S}}^4 + 4J_{\mathcal{S}}^2}, \tag{3.21}$$

29

where

$$R_{\mathcal{S}} = \sqrt{\frac{A_{\mathcal{S}}}{4\pi}} \qquad \text{and} \qquad A_{\mathcal{S}} = \int_{\mathcal{S}} ds = \int_{\mathcal{S}} \sqrt{q} d\Omega^2. \qquad (3.22)$$

This formula is the same as the equation for the irreducible mass of a Kerr black hole, but can be shown to hold in the more general case we require for analyzing our simulations [18].

The similarities between the ADM measures and quasi-local measures are not coincidence; recall the last paragraph of §3.1. For our binary black hole simulations, the quasi-local masses of the two black holes correspond to doing the integral (3.10) over the two apparent horizons as boundaries of the universe. Again, these quasi-local measures can be found using field theory and are related to boundary terms in the Hamiltonian. The sum of the quasi-local masses of the black holes will come close to equaling the ADM mass computed at infinity; the difference being due to the gravitational wave content of the slice. In this case, the volume integral over all of Σ exterior to the apparent horizons really is non-zero. When the horizons extend to timelike infinity, this difference can be used to measure the amount of gravitational radiation escaping to future null infinity. We will see how an effective energy density for gravitational radiation comes about in §3.4.

Section 3.3: Newman-Penrose Formalism and the Weyl Scalars

We turn attention now to the Newman-Penrose formalism [38, 39], in particular on what it has to say about the Weyl scalars. After discussing spin-weight, we will look at how the Weyl scalars relate to metric perturbations which is useful for the discussion of gravitational waves in §3.4.

The Weyl scalars are five complex scalars obtained from various projections of the Weyl tensor, which is

$$^{(4)}C_{abcd} \equiv {}^{(4)}R_{abcd} - \frac{1}{2}\left(g_{ac}{}^{(4)}R_{bd} - g_{ad}{}^{(4)}R_{bc} - g_{bc}{}^{(4)}R_{ad} + g_{bd}{}^{(4)}R_{ac}\right) + \frac{1}{6}\left(g_{ac}g_{bd} - g_{ad}g_{bc}\right){}^{(4)}R \quad (3.23)$$

in four dimensions. One important thing to notice about the construction of this tensor is that it is the Riemann tensor with combinations of the Ricci tensor and Ricci scalar removed. In fact, because the Ricci tensor is the trace of the Riemann tensor, the Weyl tensor is the trace-free part of the Riemann tensor. In four dimensions, the Riemann tensor's symmetries reduce the number of its algebraically independent components to twenty; this information content is divided evenly between the Ricci and Weyl tensors, each of which have ten independent components. For vacuum spacetimes – where Einsten's equations require the Ricci tensor to vanish – there will turn out to be at most ten non-zero independent components in the Riemann tensor which all correspond to information contained in the Weyl tensor. We will see how we can extract information about gravitational waves in our simulations from the Weyl tensor. The Newman-

Penrose formalism is based around projections of $^{(4)}C_{abcd}$ onto a null tetrad. The Weyl scalars are defined by

$$\psi_0 \equiv -\,^{(4)}C_{abcd} k^a m^b k^c m^d \tag{3.24a}$$

$$\psi_1 \equiv -\,^{(4)}C_{abcd} k^a l^b k^c m^d \tag{3.24b}$$

$$\psi_2 \equiv -\frac{1}{2}\,^{(4)}C_{abcd} \left(k^a l^b k^c l^d - k^a l^b m^c \overline{m}^d \right) \tag{3.24c}$$

$$\psi_3 \equiv \,^{(4)}C_{abcd} k^a l^b l^c \overline{m}^d \tag{3.24d}$$

$$\psi_4 \equiv -\,^{(4)}C_{abcd} l^a \overline{m}^b l^c \overline{m}^d, \tag{3.24e}$$

each of which is complex.

We now introduce the concept of 'spin-weighted' functions [29, 13]. There turns out to be some ambiguity in how m^a and $\overline{m}^a$ are defined. The necessary properties of orthonormality still hold under any transformation of the form

$$m^a \mapsto e^{\imath \eta} m^a \qquad \text{and} \qquad \overline{m}^a \mapsto e^{-\imath \eta} \overline{m}^a. \tag{3.25}$$

If some function f transforms as

$$f \mapsto e^{\imath s \eta} f \tag{3.26}$$

under (3.25), f is said to have spin-weight s. As an example, spherical harmonics have spin-weight zero. However, [29] define differential operators $\eth$ and $\overline{\eth}$ which raise and lower (respectively) the spin weight of whatever they are acting on; for f with spin-weight s

$$\eth f = -\sin^s \theta \left(\frac{\partial}{\partial \theta} + \imath \csc \theta \frac{\partial}{\partial \phi} \right) \sin^{-s} \theta f \tag{3.27a}$$

$$\overline{\eth} f = -\sin^{-s} \theta \left(\frac{\partial}{\partial \theta} - \imath \csc \theta \frac{\partial}{\partial \phi} \right) \sin^s \theta f. \tag{3.27b}$$

To re-enforce that these are raising and lowering operators, note that

$$\left(\overline{\eth}\eth - \eth\overline{\eth} \right) f = 2sf. \tag{3.28}$$

From the definitions of the Weyl scalars given above, we can count m^a and $\overline{m}^a$ to see that (3.25) sends

$$\psi_0 \mapsto e^{2\imath\eta} \psi_0 \tag{3.29a}$$

$$\psi_1 \mapsto e^{\imath\eta} \psi_1 \tag{3.29b}$$

31

$$\psi_2 \mapsto \psi_2 \tag{3.29c}$$

$$\psi_3 \mapsto e^{-i\eta}\psi_3 \tag{3.29d}$$

$$\psi_4 \mapsto e^{-2i\eta}\psi_4. \tag{3.29e}$$

In particular, we are often interested in ψ_4, which has spin weight -2. Spherical harmonics with spin-weight s are defined by

$$_s Y_{lm} \equiv \begin{cases} \sqrt{\frac{(l-s)!}{(l+s)!}} \eth^s Y_{lm} & 0 \leq s \leq l \\ \sqrt{\frac{(l+s)!}{(l-s)!}} \left(-\bar{\eth}\right)^s Y_{lm} & -l \leq s \leq 0 \\ \text{undefined} & |s| > l \end{cases} \tag{3.30}$$

For each s, the $_s Y_{lm}$ form a complete orthonormal basis for functions on the sphere. Numerical simulations often decompose ψ_4 into spherical harmonic amplitudes, and typically this is done using $_{-2} Y_{lm}$

$$\psi_4^{l,m}(t,r) = \int {}_{-2} Y_{l,m}^* \psi_4(t,r,\theta,\phi) d\Omega^2. \tag{3.31}$$

This decomposition is usually done on some small number of fixed radii as a function of simulation time. This spherical harmonic decomposition has the additional advantage of naturally reflecting the fact that conservation of mass and momentum require that gravitational radiation has no monopole $\psi_4^{0,m}$ or dipole $\psi_4^{1,m}$ parts. Often, the $\psi_4^{2,2}$ mode dominates. However, when we consider one black hole the $\psi_4^{2,0}$ dominates, reflecting the cylindrical symmetry of the problem.

Expanding the Riemann tensor to first-order relative to the flat background,

$$^{(4)}R_{abcd} = \frac{1}{2}\left({}^{(1)}h_{ad,bc} - {}^{(1)}h_{ac,bd} - {}^{(1)}h_{bd,ac} + {}^{(1)}h_{bc,ad}\right) + \mathcal{O}\left(h^2\right) \tag{3.32}$$

and recognizing that for vacuum spacetimes $^{(4)}R_{abcd} = {}^{(4)}C_{abcd}$, we see that

$$\psi_4 = -\frac{1}{2}\left({}^{(1)}h_{ad,bc} - {}^{(1)}h_{ac,bd} - {}^{(1)}h_{bd,ac} + {}^{(1)}h_{bc,ad}\right) l^a \overline{m}^b l^c \overline{m}^d + \mathcal{O}\left(h^2\right). \tag{3.33}$$

In the case of an outgoing radial wave[2]

$$^{(1)}h_{ab} = h_+ \left(t - r\right) e_{ab}^+ + h_\times \left(t - r\right) e_{ab}^\times \tag{3.34a}$$

$$e_{ab}^+ = \delta_{a\theta}\delta_{b\theta} - \delta_{a\phi}\delta_{b\phi} \tag{3.34b}$$

---

[2]The mathematics of gravitational waves and the notation will be covered more in §3.4.

$$e_{ab}^{\times} = \delta_{a\theta}\delta_{b\phi} + \delta_{a\phi}\delta_{b\theta}. \tag{3.34c}$$

With (3.34), (3.33) can be reduced to[3]

$$\psi_4 = \ddot{h}_+ - \imath \ddot{h}_\times, \tag{3.35}$$

i.e. ψ_4 gives the second time-derivative of the strain. The real and imaginary parts give the two polarizations of the wave.

Section 3.4: Gravitational Wave Content

We begin this section by considering the wave equation for metric perturbations. Next, we expand the Ricci tensor to obtain an effective stress-energy tensor for gravitational waves. Finally, we use this stress-energy tensor to compute the luminosity of gravitational radiation. In this section we will be considering only spacetime quantities and so will drop the prefix (4) to avoid possible confusion with order prefixes (in this section only).

To linear order and in Lorentz gauge, the metric perturbation satisfies the wave equation

$$\Box \bar{h}_{ab} = -16\pi T_{ab}, \tag{3.36}$$

where we have introduced the 'trace reversed' metric perturbation $\bar{h}_{ab} \equiv {}^{(1)}h_{ab} - \frac{1}{2}{}^{(1)}h^c{}_c\eta_{ab}$. In vacuum, this is the homogeneous wave equation. Being a differential gauge condition, Lorentz gauge is a class of coordinate conditions that requires an additional restriction. One such restriction brings the gauge into the transverse-traceless form (when in vacuum), admitting a solution with a traveling wave in the z direction

$$h_{ab}^{TT} = h_+ (t - z) e_{ab}^+ + h_\times (t - z) e_{ab}^\times = \begin{pmatrix} 0 & 0 & 0 & 0 \\ 0 & h_+ (t-z) & h_\times (t-z) & 0 \\ 0 & h_\times (t-z) & -h_+ (t-z) & 0 \\ 0 & 0 & 0 & 0 \end{pmatrix}. \tag{3.37}$$

Now consider the expansion of the Ricci tensor [35, 13]

$$R_{ab} = {}^{(1)}R_{ab} + {}^{(2)}R_{ab} + \mathcal{O}\left(h^3\right) \tag{3.38a}$$

$${}^{(1)}R_{ab} = {}^{(1)}F_{ab}\left({}^{(1)}h\right) \tag{3.38b}$$

---

[3]Overdots represent time derivatives in (3.35). Also note that although (3.35) is typically written without $\mathcal{O}\left(h^2\right)$, it is first-order in the metric perturbation.

$$^{(2)}R_{ab} = {}^{(1)}F_{ab}\left(^{(2)}h\right) + {}^{(2)}F_{ab}\left(^{(1)}h\right) \tag{3.38c}$$

$$^{(1)}F_{ab}\left(h\right) \equiv \frac{1}{2}\left(-h^c{}_{c,ab} - h_{ab,c}{}^c + h_{ca,b}{}^c + h_{cb,a}{}^c\right) \tag{3.38d}$$

$$^{(2)}F_{ab}\left(h\right) \equiv \frac{1}{4}h_{cd,a}h^{cd}{}_{,b} + \frac{1}{2}h^{cd}\left(h_{cd,ab} + h_{ab,cd} - h_{ac,bd} - h_{bc,ad}\right) + \frac{1}{2}h_b{}^{c,d}\left(h_{ac,d} - h_{ad,c}\right)$$

$$+ \frac{1}{2}\left(h^{cd}{}_{,d} - \frac{1}{2}h_d{}^{d,c}\right)\left(h_{ab,c} - h_{ca,b} - h_{cb,a}\right). \tag{3.38e}$$

Because we are considering a vacuum spacetime, the Ricci tensor must be zero order-by-order. Importantly, rearranging and trace-reversing[4] the second-order part (3.38c) can be written as

$$^{(1)}F_{ab}\left(^{(2)}h\right) - \frac{1}{2}\eta_{ab}\eta^{cd}{}^{(1)}F_{cd}\left(^{(2)}h\right) = -{}^{(2)}F_{ab}\left(^{(1)}h\right) + \frac{1}{2}\eta_{ab}\eta^{cd}{}^{(2)}F_{cd}\left(^{(1)}h\right). \tag{3.39}$$

The LHS side of (3.39) looks like the Einstein tensor constructed from $^{(2)}h_{ab}$, so we define the RHS to be an effective second-order stress-energy tensor

$$t_{ab}^{\rm GW} \equiv -\frac{1}{8\pi}\left[^{(2)}F_{ab}\left(^{(1)}h\right) - \frac{1}{2}\eta_{ab}\eta^{cd}{}^{(2)}F_{ab}\left(^{(1)}h\right)\right]. \tag{3.40}$$

Because energy in the gravitational field cannot be localized in general relativity, we must do a short-wave averaging procedure [35] where we integrate over several wavelengths of the gravitational wave (denoted by brackets $\langle\ \rangle$). Using this averaging

$$T_{ab}^{\rm GW} = \frac{1}{32\pi}\left\langle^{(1)}h_{cd,a}^{\rm TT}{}^{(1)}h_{\rm TT,b}^{cd}\right\rangle = \frac{1}{16\pi}\left\langle h_{,a}^+h_{,b}^+ + h_{,a}^\times h_{,b}^\times\right\rangle. \tag{3.41}$$

This same analysis can be carried out in the case where instead of expanding around Minkowski spacetime, we are expanding around some other background metric. The computations are more complicated in this case, but the results are quite similar. The total stress-energy tensor for the spacetime is the sum of the matter stress-energy tensor and an effective stress-energy tensor of the gravitational field (which is quadratic in the first-order perturbations)

$$R_{ab} - \frac{1}{2}g_{ab}R = 8\pi\left(T_{ab} + T_{ab}^{\rm GW}\right). \tag{3.42}$$

At the end of §3.2 we saw that, in a vacuum spacetime, the difference between the ADM mass of the spacetime computed at infinitely large radius and the quasi-local measures of mass computed on the black hole horizons should be non-zero only in the case of an energy density linked to gravitational waves. Equation (3.42) shows that the ADM mass includes energy from the gravitational waves through $T_{ab}^{\rm GW}$. Additionally,

---

[4]To trace-reverse a spacetime quantity subtract half its trace times the metric.

in §3.3 we claimed that there would be a link between the Weyl scalars and gravitational waves; equations (3.35) and (3.41) demonstrate this.

The luminosity of gravitational waves comes from integrating T_{ab}^{GW}

$$L_{\text{GW}} = -\frac{dE}{dt} = \frac{1}{16\pi} \int_{\partial\Sigma} \left\langle \dot{h}_+^2 + \dot{h}_\times^2 \right\rangle ds \tag{3.43a}$$

$$= \frac{1}{16\pi} \int_{\partial\Sigma} \left| \int_{-\infty}^{t} \psi_4 \left(t'\right) dt' \right|^2 ds \tag{3.43b}$$

$$= \lim_{r\to\infty} \frac{r^2}{16\pi} \sum_{l,m} \left| \int_{-\infty}^{t} \psi_4^{l,m} \left(t'\right) dt' \right|^2 . \tag{3.43c}$$

As before, we carry out the surface integral at infinity because the derivation of T_{ab}^{GW} assumed the weak field limit. In practice, (3.43c) is difficult to compute during post-processing. The limit to large or infinite radii must be done by extrapolating data from finite radii. There is also the additional complication that the extrapolation is best done as a function of retarded time $t_{\text{ret}} = t - r$, since the spherical harmonic modes are computed at different radii. The biggest problem though is the time integral: strictly speaking, it must be done from an infinite time in the past. Since $\psi_4^{l,m}$ is small before the simulation starts, this tends to not be a large problem. The accumulation of low-frequency unphysical modes is a bigger issue. These modes can be suppressed by 'fixed-frequency integration' [45]. Note that

$$\dot{h}^{l,m}(t) = \int^{t} \psi_4^{l,m} \left(t'\right) dt' = \mathcal{F}^{-1}\left[\frac{\tilde{\psi}_4^{l,m}\left(\omega\right)}{-\imath\omega} \right], \tag{3.44}$$

where $\mathcal{F}^{-1}$ is the inverse Fourier transform[5] and $\tilde{\psi}_4^{l,m}$ is the Fourier transform of $\psi_4^{l,m}$. Fixed-frequency integration chooses some limiting frequency ω_0 and takes

$$\dot{h}^{l,m}(t) = \mathcal{F}^{-1}\left[\frac{\tilde{\psi}_4^{l,m}\left(\omega\right)}{-\imath \max(\omega,\omega_0)} \right]. \tag{3.45}$$

This makes the denominator inside the inverse Fourier transform larger for $\omega < \omega_0$ and therefore limits these modes' contributions to the final result. While this does work, it requires two Fourier transforms and is therefore computationally expensive. An integration constant must also be found. Because of all these difficulties, it is common to just consider $\psi_4^{l,m}$ instead of the energy or luminosity when comparing simulation results.

Fig. 3.2 shows an example of what plots of the Weyl scalar look like. The data comes from a simulation that was initialized with Bowen-York data. From the plot, we are able two important things:

---

[5]Equation (3.44) is a basic property of the Fourier transform.

1. Because these curves correspond to different radii and the gravitational radiation moves at the speed of light, we expect the radiation curves to peak at different times. The first peak visible in all curves happens at $t_{\text{ret}} \approx 0$.

2. The junk radiation peak is weaker than the initial physical signal, but only by about a factor of two. This demonstrates how it can be difficult to separate the junk radiation from the physically realistic signal.

$r|\psi_4^{2,2}|$ as a Function of Simulation Time Sampled at Five Radii
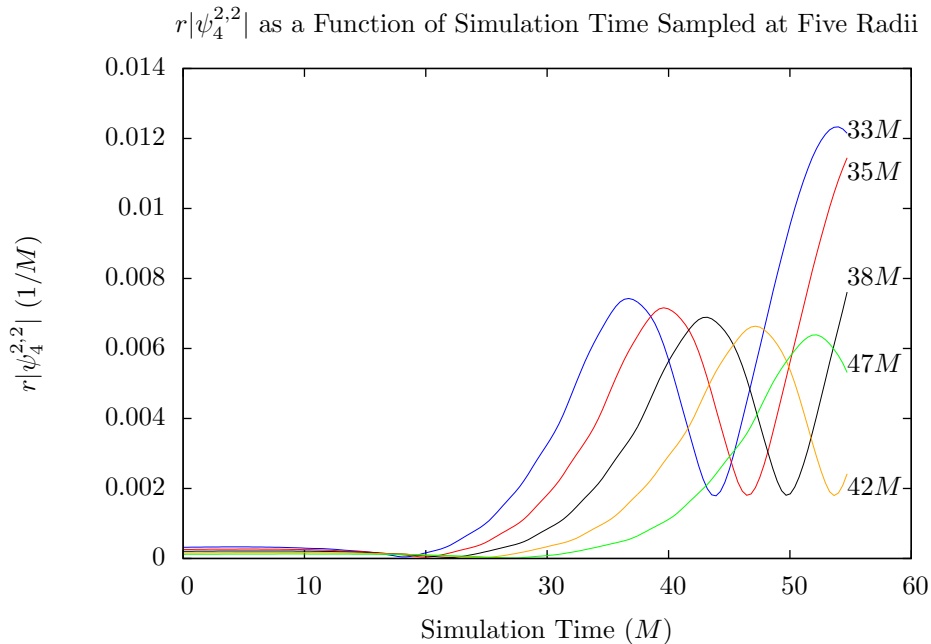
Figure 3.2: Plot of $r|\psi_4^{2,2}|$ as a function of simulation time at five different radii between $33M$ and $47M$ (with labels along the right side of the plot). Note the peaks in junk radiation at approximately $t = r$ (or $t_{\text{ret}} = 0$) before the larger peak corresponding to a physical signal. Note also that the amplitudes of the junk radiation peaks are approximately equal, indicating that this wave does indeed fall off approximately as $1/r$.

CHAPTER 4:   Numerical Methods and the Einstein Toolkit

In this Chapter we give a very brief overview of some of the numerical methods we use and discuss how the Einstein Toolkit implements them [32]. The Einstein Toolkit is built on Cactus, a general scientific modeling framework. One of the main strengths of Cactus is its modularity; in the Cactus vernacular, modules are called 'thorns' which contrast with the 'flesh,' the main body of Cactus which provides high level infrastructure (including controlling scheduling of subroutines, communication among thorns, and allocation of storage for variables, among other things). Thorns can be written in Fortran, C, or C++, and their names are traditionally written in monospaced font (e.g., `QuasiLocalMeasures`, `TwoPunctures`, `ML_BSSN`).

The Einstein Toolkit consists of Cactus along with a collection of thorns which utilize Cactus to solve Einstein's equations, magnetohydrodynamic equations (although, for this project we do not make use of this), and carry out analysis relevant for astrophysics. In the sections to follow, we will briefly cover many of the most important thorns used in our simulations, along with the numerical methods they employ. However, a typical application of the Einstein Toolkit uses many more thorns than we will be able to discuss here (a typical simulation utilizes roughly fifty thorns). Some of the more important thorns, which are not covered in more detail below, include:

1. `ADMBase` to initialize variables containing ADM data and coordinate their communication among thorns,

2. `CarpetIOHDF5` to write output files,

3. `CoordBase` to set up the grid,

4. `LoopControl` to handle loops over grids and mesh refinement levels,

5. `TerminationTrigger` to terminate simulations given certain conditions (e.g., after a certain amount of wallclock time) and output data in such a way that the simulation can be resumed,

6. `NaNChecker` to monitor variables for NaNs and warn the user or terminate the simulation,

7. and `SystemStatistics` to keep the user updated on things such as memory usage.

Thorns also exist for `BLAS`, `PETSc`, `FFTW`, etc., or at compile time the Einstein Toolkit can be told to use a copy already built on the system.

Section 4.1: Finite Differencing

Arguably the most important numerical technique – at the heart of how the Einstein Toolkit operates – is 'finite differencing.' A finite difference is a way to approximate derivatives of a function, the values of which are only known at the points of some discrete grid [15]. The basic idea can be seen from the following example. Imagine some function $f(x)$ which is known at the grid points $x_0 - \Delta x$, x_0, and $x_0 + \Delta x$. If the grid spacing Δx is small, we can Taylor expand to find

$$f(x_0 - \Delta x) = f(x_0) - f'(x_0)\Delta x + \frac{1}{2}f''(x_0)\Delta x^2 - \frac{1}{6}f'''(x_0)\Delta x^3 + \mathcal{O}(\Delta x^4) \tag{4.1a}$$

$$f(x_0 + \Delta x) = f(x_0) + f'(x_0)\Delta x + \frac{1}{2}f''(x_0)\Delta x^2 + \frac{1}{6}f'''(x_0)\Delta x^3 + \mathcal{O}(\Delta x^4). \tag{4.1b}$$

Given this, we have the standard (second-order accurate) finite difference schemes for first and second derivatives

$$\frac{f(x_0 + \Delta x) - f(x_0 - \Delta x)}{2\Delta x} = f'(x_0) + \frac{1}{6}f'''(x_0)\Delta x^2 + \mathcal{O}(\Delta x^3) \tag{4.2a}$$

$$\frac{f(x_0 + \Delta x) - 2f(x_0) + f(x_0 - \Delta x)}{\Delta x^2} = f''(x_0) + \mathcal{O}(\Delta x^2). \tag{4.2b}$$

These are two of the simplest (and most common) examples of finite difference 'stencils' or 'molecules;' which are really just collections of coefficients for nearby grid points which, when multiplied by the function values and summed, give an approximation of a certain derivative to a certain order. See Fig. 4.1a and Fig. 4.1f for alternative representations of (4.2). Many stencils are possible, and the Einstein Toolkit uses eighth-order accurate stencils for most spatial derivatives in its simulations (Fig. 4.1i). When stencils oriented in different coordinate directions are combined, a stencil for e.g., the Laplacian can be obtained (Fig. 4.1g); when a stencil is not centered around the point x_0, it can be used for x_0 on the boundary of the domain (e.g., Figs. 4.1c through 4.1e). More examples are shown in Fig. 4.1.

Section 4.2: Resolving Features Efficiently: Mesh Refinement, `Carpet`, and `PunctureTracker`

When a problem exhibits multiple length scales (e.g., the size of a black hole, the size of an orbit, and the size of the wave zone) the resolution of the grid is dictated by the finest scale. There is no inherent downside to using a uniform grid in such problems other than the computational costs, where memory and CPU requirements build prohibitively fast for three-dimensional simulations.

'Mesh refinement' is a method where higher resolution is added only where it is needed. This gives the benefits of high resolution with a (hopefully) smaller increase in computational cost. It is not always obvious

$$x_0 - \Delta x \qquad x_0 \qquad x_0 + \Delta x$$
$$\left(\frac{-1}{2\Delta x}\right) \quad\text{—}\quad (0) \quad\text{—}\quad \left(\frac{1}{2\Delta x}\right)$$

(a) First derivative, second order, centered: (4.2a).

$$x_0 - \Delta x \qquad x_0$$
$$\left(\frac{-1}{\Delta x}\right) \quad\text{—}\quad \left(\frac{1}{\Delta x}\right)$$

(b) First derivative, first order, off-center.

$$x_0 \qquad x_0 + \Delta x$$
$$\left(\frac{-1}{\Delta x}\right) \quad\text{—}\quad \left(\frac{1}{\Delta x}\right)$$

(c) First derivative, first order, off-center.

$$x_0 - 2\Delta x \qquad x_0 - \Delta x \qquad x_0$$
$$\left(\frac{1}{2\Delta x}\right) \quad\text{—}\quad \left(\frac{-2}{\Delta x}\right) \quad\text{—}\quad \left(\frac{3}{2\Delta x}\right)$$

(d) First derivative, second order, off-center.

$$x_0 \qquad x_0 + \Delta x \qquad x_0 + 2\Delta x$$
$$\left(\frac{-3}{2\Delta x}\right) \quad\text{—}\quad \left(\frac{2}{\Delta x}\right) \quad\text{—}\quad \left(\frac{-1}{2\Delta x}\right)$$

(e) First derivative, second order, off-center.

$$x_0 - \Delta x \qquad x_0 \qquad x_0 + \Delta x$$
$$\left(\frac{1}{\Delta x^2}\right) \quad\text{—}\quad \left(\frac{-2}{\Delta x^2}\right) \quad\text{—}\quad \left(\frac{1}{\Delta x^2}\right)$$

(f) Second derivative, second order: (4.2b).

(g) Laplacian, second order.

$$x_0 - 2\Delta x \qquad x_0 - \Delta x \qquad x_0 \qquad x_0 + \Delta x \qquad x_0 + 2\Delta x$$
$$\left(\frac{-1}{12\Delta x^2}\right) \quad\text{—}\quad \left(\frac{4}{3\Delta x^2}\right) \quad\text{—}\quad \left(\frac{-5}{2\Delta x^2}\right) \quad\text{—}\quad \left(\frac{4}{3\Delta x^2}\right) \quad\text{—}\quad \left(\frac{-1}{12\Delta x^2}\right)$$

(h) Second derivative, fourth order.

$$x_0 - 4\Delta x \quad x_0 - 3\Delta x \quad x_0 - 2\Delta x \quad x_0 - \Delta x \quad x_0 \quad x_0 + \Delta x \quad x_0 + 2\Delta x \quad x_0 + 3\Delta x \quad x_0 + 4\Delta x$$
$$\left(\frac{-1}{560\Delta x^2}\right)\left(\frac{8}{315\Delta x^2}\right)\left(\frac{-1}{5\Delta x^2}\right)\left(\frac{8}{5\Delta x^2}\right)\left(\frac{-205}{72\Delta x^2}\right)\left(\frac{8}{5\Delta x^2}\right)\left(\frac{-1}{5\Delta x^2}\right)\left(\frac{8}{315\Delta x^2}\right)\left(\frac{-1}{560\Delta x^2}\right)$$

(i) Second derivative, eighth order.

Figure 4.1: Graphical representation of finite differences for approximating various derivatives at a point $x = x_0$. The circles correspond to grid points and the numbers inside are the coefficients by which the function being differenced should be multiplied at each grid point before being summed. This should give some indication why the terms "stencil" and "molecule" are often used. It should also give some indication of the variety of possible stencils in terms of size, accuracy order, derivative, centered vs off-centered, and in different dimensions.

that mesh refinement will provide computational savings as there is an overhead associated with managing the mesh refinement, because it can be extremely complicated to implement. If the locations of small length scales do not change throughout the simulation, 'static mesh refinement' can be used. However, for our simulations the mesh refinement must track the black holes, meaning 'adaptive mesh refinement' is required: the resolution of a region changes with the changing length scales it contains. If it is not known *a priori* where small scales will be throughout a simulation, complex algorithms which monitor gradients of grid variables can be used.

While we do not know exactly which areas of our simulation will have small length scales, we do know that small length scales will be confined to regions around the black hole(s). The Einstein Toolkit takes advantage of this fact to adopt a form of adaptive mesh refinement that has a lower computational cost overhead, where the adaptations are driven by the movement of the black hole(s). Mesh refinement is facilitated by the thorn `Carpet` (first described in [47]). It is capable of handling many resolutions simultaneously. Box-in-box refinement is used: i.e., the refined regions are always rectangular boxes and a region of a given resolution is completely contained within a region of lower resolution. Our grids are set up so that the entire domain is covered by the coarsest grid, with nested, concentric boxes around the black hole(s). Each box has twice the resolution (half the grid spacing) as the next coarsest box. As many as eleven refinement levels (or twelve different resolutions) have been used [36].

`PunctureTracker` monitors the locations of the black holes; specifically, their punctures. It does this by monitoring the shift vector. Recall the interpretation of the shift as the motion of the spatial coordinates in going from one spatial slice to the next. If from the black hole's viewpoint the coordinates move in one direction (given by the shift vector), from the coordinate system's viewpoint the black hole's puncture must have moved (an equal distance) in the opposite direction

$$v_{\mathrm{BH}}^i(t) = -\beta^i\left(t, x_{\mathrm{BH}}^i(t)\right).$$

(4.3)

The former view is a passive description of the transformation and the latter is an active description.

Integrating (4.3),

$$x_{\mathrm{BH}}^i(t) = x_{\mathrm{BH}}^i(t_0) - \int_{t_0}^t \beta^i\left(t', x_{\mathrm{BH}}^i(t')\right) dt'.$$

(4.4)

Numerically, the location of the puncture at a time t_{n+1} is found by interpolating to find the value of the shift at the location of the puncture at time t_n. This shift value (times the time step) is then subtracted from the previous location of the puncture

$$x_{\mathrm{BH}}^i(t_{n+1}) = x_{\mathrm{BH}}^i(t_n) - \beta^i\left(t_{n+1}, x_{\mathrm{BH}}^i(t_n)\right) \Delta t.$$

(4.5)

The thorn must therefore be given the correct location of the puncture(s) at the beginning of the simulation. Equation (4.5) is a first-order approximation to the integral in (4.4)[1] and is done at every time step.

With `PunctureTracker` constantly updating the location of punctures throughout the simulation, the Einstein Toolkit knows where resolution is most needed. At user-defined intervals `CarpetRegrid2` is able to use the puncture locations in order to restructure the areas of higher resolution, to reflect the changing locations where resolution is needed most. This is a somewhat limited form of adaptive mesh refinement; only recently have numerical relativists made use of the fully adaptive mesh refinement which monitors gradients [24].

Section 4.3:   Evolution, Method of Lines, `ML_BSSN`, and `MoL`

Consider the example of a one dimensional wave equation with a propagation speed[2] c_w

$$\frac{1}{c_w^2}\frac{\partial^2 u}{\partial^2 t} = \frac{\partial^2 u}{\partial^2 x}. \tag{4.6}$$

One possible way to solve this equation by finite differencing is to use a scheme where we center second order stencils around x_i and t_n (Fig. 4.1f or (4.2b)). Using the notation $u_i^n = u(t_n, x_i)$,

$$\frac{1}{c_w^2}\frac{u_i^{n-1} - 2u_i^n + u_i^{n+1}}{\Delta t^2} = \frac{u_{i-1}^n - 2u_i^n + u_{i+1}^n}{\Delta x^2}. \tag{4.7}$$

Or, solving for u_i^{n+1}, we can find the updated value of u at the next time step

$$u_i^{n+1} = 2u_i^n - u_i^{n-1} + c_w^2\frac{\Delta t^2}{\Delta x^2}\left(u_{i-1}^n - 2u_i^n + u_{i+1}^n\right). \tag{4.8}$$

To examine the stability of the scheme (4.7) assume a solution of the form

$$u_i^n = A^n e^{ik\Delta xi}. \tag{4.9}$$

---

[1]Specifically, (4.5) can be thought of as a finite difference stencil corresponding to the integral. Alternatively, it can be found from algebraic manipulations of the finite difference stencil for the velocity in (4.3). This is like the midpoint rule, but using the shift at time t_{n+1} instead of interpolated halfway between t_n and t_{n+1} causes it to be a lower order approximation.

[2]We refer to c_w as the speed of light, though we do not mean this literally. It is simply helpful to have a common language with which to refer to the speed of propagation of the signal, whatever the physical interpretation of that signal is.

In order for this solution to not grow without bound, we require $|A| \leq 1$. Plugging (4.9) into (4.7), we find

$$A = 2 - A^{-1} + c_w^2 \frac{\Delta t^2}{\Delta x^2} \left(2 \cos k \Delta x - 2 \right) \tag{4.10}$$

so that $|A| \leq 1$ for all wave numbers k if and only if

$$c_w \leq \frac{\Delta x}{\Delta t}. \tag{4.11}$$

This says that the time step Δt cannot be so large that information moving at the speed of light c_w is able to travel more than one grid point away Δx during that time step; i.e., a grid point cannot be "aware" of information outside its light cone.

There are many such evolution schemes we could employ, based on the accuracy we want, the number of time levels we are able to store, etc. However, not all possible combinations will yield stable evolution, so one should be careful when choosing a scheme [15, 44]. Some schemes are stable, but with stronger or weaker conditions than (4.11), some are unconditionally stable, and some are unconditionally unstable.
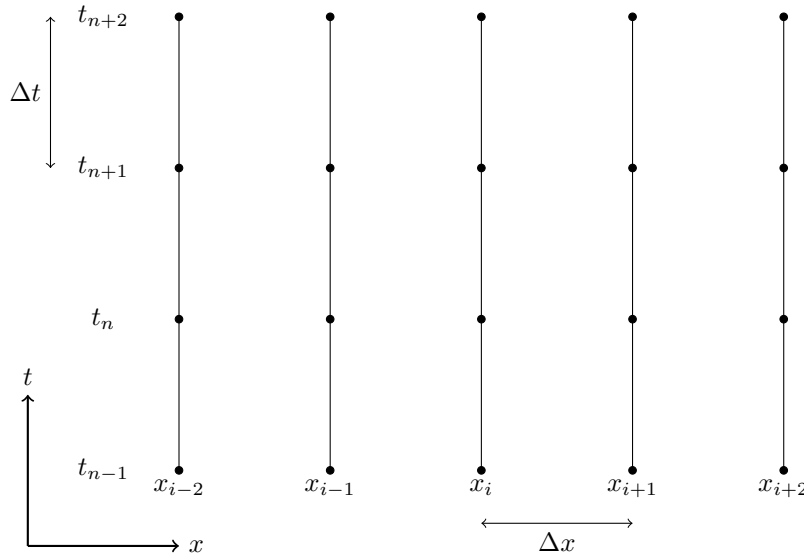
Figure 4.2: A representation of the method of lines in the tx-plane.

As an alternative to (4.7), we can apply a finite difference to only the spatial derivative. Using the notation $u_i(t) = u(t, x_i)$,

$$\frac{1}{c_w^2} \frac{\partial^2 u_i(t)}{\partial^2 t} = \frac{u_{i-1}(t) - 2u_i(t) + u_{i+1}(t)}{\Delta x^2}. \tag{4.12}$$

This yields a coupled set of ordinary differential equations for the $u_i(t)$, which are solved using techniques other than finite differencing. This strategy is called the 'method of lines.' We integrate along lines at each

grid point; see Fig. 4.2.

The thorns `McLachlan` and `MoL` use method of lines with fourth-order Runge-Kutta to do the time evolution in our simulations [3]. There are many versions of `McLachlan` which evolve different evolution equations corresponding to different decompositions of Einstein's equations (e.g., [14]). We use `ML_BSSN` to evolve (2.53), (2.54), and (2.75), though with the slight modification of using W mentioned just under (2.74) as the conformal factor instead of ϕ. Numerical dissipation can be used, but constraint damping is not (as it is in the Z4 formulation of the evolution equations [14]) [32]. Since constraint damping is not used, monitoring any growth in the magnitude of the constraint violations H and M^i can be used as a diagnostic of numerical fidelity throughout a simulation.

Section 4.4: Thorns and Methods for Initial Data

4.4.1: Bowen-York Initial Data and `TwoPunctures`

Solutions to (2.69a) with $\tilde{A}_{ij}$ given by linear combinations of (2.70) and (2.71) yield Bowen-York initial data. The thorn `TwoPunctures` finds a solution for the conformal factor in order to construct this data [16]. `TwoPunctures` uses a specially adapted bipolar coordinate system where the two coordinate singularities of the coordinate system are coincident with the locations of the black hole punctures. This coordinate system has the advantage of only requiring us solve in one continuous domain. Additionally, `TwoPunctures` solves only for the regular part of the conformal factor ψ. The ansatz (2.72) is made and (2.69a) is treated an equation for the regular part of the field, u. In effect, the divergences have been "put in by hand."

`TwoPunctures` uses a spectral method instead of finite differencing. The spectral method finds the coefficients for an expansion of the solution in terms of basis functions instead of solving for values of the solution directly on the discrete grid used for evolution. The spectral expansion in this case is a Fourier expansion in the azimuthal direction and a Chebyshev expansion in each of the other two spatial coordinates. The spectral method is efficient and converges exponentially with increasing number of basis functions. Once the spectral solution is known, it is interpolated back onto the usual spatial grid; this interpolation has recently been made significantly more efficient [41].

4.4.2: Successive Over-Relaxation and `CT_MultiLevel`

Consider the matrix problem

$$\mathbf{A}\vec{x} = \vec{b}, \tag{4.13}$$

where $\mathbf{A}$ is an $N \times N$ matrix. We can always decompose $\mathbf{A}$ into its lower triangular, diagonal, and upper triangular parts

$$\mathbf{A} = \mathbf{L} + \mathbf{D} + \mathbf{U}. \tag{4.14}$$

Substituting (4.13) in (4.14), multiplying both sides by ω,[3] and rearranging terms gives us

$$[\omega \mathbf{L} + \mathbf{D}] \vec{x} = - [\omega \mathbf{U} + (\omega - 1) \mathbf{D}] \vec{x} + \omega \vec{b}. \tag{4.15}$$

At this point, (4.15) is the same as (4.13): we have made no approximations. In successive over-relaxation, (4.15) is solved iteratively by saying the updated LHS (iteration $n+1$) must equal the RHS evaluated with the previous iterate (iteration n) [44]

$$[\omega \mathbf{L} + \mathbf{D}] \vec{x}^{n+1} = - [\omega \mathbf{U} + (\omega - 1) \mathbf{D}] \vec{x}^{n} + \omega \vec{b}, \tag{4.16}$$

or rearranged

$$\vec{x}^{n+1} = \vec{x}^{n} + \omega \mathbf{D}^{-1} \left[\vec{b} - (\mathbf{U} + \mathbf{D}) \vec{x}^{n} - \mathbf{L} \vec{x}^{n+1} \right]. \tag{4.17}$$

Writing (4.17) out in components,

$$x_i^{n+1} = x_i^n + \frac{\omega}{A_{ii}} \left(b_i - \sum_{j \geq i} A_{ij} x_j^n - \sum_{j < i} A_{ij} x_j^{n+1} \right) \qquad i, j \in \{1, 2, \ldots, N\} \qquad \text{(no sum on } i\text{)}. \tag{4.18}$$

Careful consideration of (4.18) shows that if we apply it repeatedly – each time increasing i by one – the two sums on the RHS taken together are just $(\mathbf{A}\vec{x})_i$ with the most current values of $\vec{x}$ being used, be they x_i^{n+1} or x_i^n.

Writing the finite difference stencil (e.g., an equation like (4.8)) in matrix form (4.13), we can then apply successive over-relaxation to obtain a numerical solution to a differential equation. In this case, increasing i as mentioned above "sweeps" the finite difference stencil over the grid, updating the values of the solution at each point based on its neighbors (again, using updated values where possible).

`CT_MultiLevel` is an initial data thorn that implements successive over-relaxation to solve elliptic differential equations [21]. It was designed with cosmological applications in mind and is able to handle the additional complications arising with periodic boundary conditions (e.g., re-normalizing the DC mode). But it was written in a very general way and may prove useful in superposing our initial data.

---

[3]This ω is unrelated to the one-form from Chapter 2. For successive over-relaxation $1 < \omega < 2$, which determines by how much the solution is "overshot" at each iteration.

Section 4.5:   Thorns for Analysis

4.5.1:   Finding and Storing Apparent Horizons: `AHFinderDirect` and `SphericalSurface`

`AHFinderDirect` finds the apparent horizons in a simulation [51, 52]. It does this by solving for the outermost surface where the expansion of outgoing light rays (3.17) is equal to zero. Once the location of a horizon has been found, it is stored in a data structure provided by the `SphericalSurface` thorn. `SphericalSurface` allows for the storage and communication of information about surfaces within the simulation that are topologically spheres. The information is stored as $r(\theta, \phi)$ on all points on the spherical grid as well as an origin and other meta-data.

4.5.2:   `QuasiLocalMeasures`, `WeylScal4`, and `Multipole`

`QuasiLocalMeasures` computes integrals such as (3.11), (3.12), (3.13), (3.19), and (3.22), among other measures of black hole properties [27]. It uses information stored by `AHFinderDirect` in `SphericalSurface` to carry out the integrals on horizons and other surfaces defined by the user stored by `SphericalSurface` for integrals over spheres at large radii.

`WeylScal4` does the projections (3.24) throughout the entire simulation domain [19]. The real and imaginary parts of all five Weyl scalars are, in principal, available at all grid points. However, usually only the multipole moments are considered. `Multipole` does the integrals such as (3.31), though it is able to find spherical harmonic coefficients of any variable using any spin-weight [4]. In practice, only the Weyl scalars are decomposed in this manner.

CHAPTER 5: Building a Single Boosted Trumpet Black Hole

Having set the stage with the theoretical background given in the previous three Chapters, we are now in a position to understand how we can construct black hole initial data which avoids some of the downsides of data produced using the Bowen-York formalism. In particular, we are able to construct initial data which satisfies the constraint equations without resorting to the mathematically simplifying assumptions which lead to junk radiation. We call this new initial data 'boosted-trumpet' data, as it utilizes a Lorentz boost and a trumpet slicing which is closely adapted to the moving punctures gauge. We describe the theory behind boosted-trumpet initial data and practical considerations for constructing it in section 5.1. In section 5.2, we outline how our simulations are set up and the development of relevant diagnostic tools. In section 5.3 we look at the properties of the coordinate system at large radius and utilize data from simulations to compare boosted-trumpet initial data with canonical Bowen-York initial data. We make summary remarks about our coordinate system in section 5.4. Considerations validating our initial data code can be found in section 5.5. This Chapter is closely adapted from an article in preparation for submission to *Phys. Rev. D.*

Section 5.1: Trumpet Coordinates for a Boosted Black Hole

In this section we lay out our analytic approach to constructing a coordinate system with trumpet time slices which are adapted to the moving punctures gauge for a boosted black hole. To set the stage for that result, we first briefly review the understanding of trumpet slicing for a static (unboosted) black hole developed previously by Hannam et al. [30] (and refer the reader to that paper for more thorough derivations). We begin with ingoing Eddington-Finkelstein coordinates, inc contrast to [30] who started with Schwarzschild coordinates; these two coordinate systems are related by a height function, which will give the difference between the height function we obtain and that obtained in [30]. The relevant results are given here in our notation, which differs slightly from the original paper.

5.1.1: Review of Trumpet Slicing of a Static Black Hole

The line element for Schwarzschild spacetime in Kerr-Schild coordinates ($\overline{t}'$, $\overline{x}'$, $\overline{y}'$, and $\overline{z}'$) is given by

$$ds^2 = \left[\eta_{\overline{a}'\overline{b}'} + \frac{2M}{R} l_{\overline{a}'} l_{\overline{b}'} \right] dx^{\overline{a}'} dx^{\overline{b}'}, \tag{5.1}$$

where $l_{\bar{a}'} \equiv (R, \bar{x}', \bar{y}', \bar{z}')/R$ and R is the Schwarzschild areal radius coordinate. The bars and primes here distinguish the Kerr-Schild coordinate system from other coordinate systems we will encounter later. In particular, a bar denotes a coordinate system which does not have the trumpet slicing adapted to the moving punctures gauge and the prime denotes a coordinate system in which a Lorentz boost has not been applied. Our final desired coordinate system will have neither bars nor primes.

Kerr-Schild coordinates have nice properties under a Lorentz boost [34], which we will find desirable in the next section, and we would therefore like to use it as the starting point for our construction. In order to carry out the analysis to determine the height-function, we need a spherical-like coordinate system though, so we change to ingoing Eddington-Finkelstein coordinates

$$ds^2 = -f d\bar{t}'^2 + \frac{4M}{R} d\bar{t}' dR + \left(1 + \frac{2M}{R}\right) dR^2 + R^2 d\Omega^2, \tag{5.2}$$

where $f \equiv 1 - 2M/R$.

We transform Kerr-Schild coordinates to a coordinate system with a new time coordinate t' related to $\bar{t}'$ by

$$t' = \bar{t}' - h(R), \tag{5.3}$$

where $h(R)$ is a to-be-determined function. Recall that un-barred coordinates are associated with a coordinate system in which the time slices have trumpet topology that is determined by the steady state of the moving punctures gauge conditions. After transforming to the new coordinate system the line element (5.2) becomes

$$ds^2 = -f dt'^2 - 2 \left[f \frac{dh}{dR} - \frac{2M}{R}\right] dt' dR + \left[1 + \frac{2M}{R} + \frac{4M}{R} \frac{dh}{dR} - f \left(\frac{dh}{dR}\right)^2\right] dR^2 + R^2 d\Omega^2. \tag{5.4}$$

We will suppress the arguments of $h(R)$. Note that the components of the metric depend on dh/dR but not h itself; we will not need to compute h in order to determine our new metric.

The 1+log slicing condition

$$\left(\partial_t - \beta^i \partial_i\right) \alpha = -n\alpha K, \tag{5.5}$$

when applied to the metric (5.4) gives an ODE which is satisfied by the lapse

$$\frac{d\alpha}{dR} = -\frac{n(3M - 2R + 2R\alpha^2)}{R(R - 2M + nR\alpha - R\alpha^2)}. \tag{5.6}$$

This equation assumes $\partial_t \alpha = 0$ (we are looking for the steady state solution) and the height function has

been eliminated in favor of α. The solution to (5.6) is

$$\alpha^2 = 1 - \frac{2M}{R} + \frac{C(n)^2 e^{2\alpha/n}}{R^4}, \tag{5.7a}$$

where the integration constant is given by

$$C(n)^2 = \frac{[3n + \sqrt{4 + 9n^2}]^3}{128 n^3} e^{-2\alpha_C/n} M^4 \tag{5.7b}$$

and the critical value of the lapse is

$$\alpha_C^2 = \frac{\sqrt{4 + 9n^2} - 3n}{\sqrt{4 + 9n^2} + 3n} \tag{5.7c}$$

at the critical radius

$$R_C = \frac{3n + \sqrt{4 + 9n^2}}{4n} M. \tag{5.7d}$$

Note that α_C and R_C are critical values in the sense that at these values both the numerator and denominator of the RHS of (5.6) go to zero, providing a finite value for $\frac{d\alpha}{dR}$ and a smooth solution through the critical point. We will now specialize to the standard 1+log gauge condition with $n = 2$.

We do not expect the lapse we compute from (5.6) to be equal to the lapse in our boosted-trumpet coordinate system. This discrepancy comes from the fact that we are applying a boost, so the analysis which would lead to the boosted analogue of (5.6) would be different. Nonetheless, we will use the height function we ultimately derive from the lapse of the unboosted black hole to create our boosted black hole. General relativity allows use to use any coordinate change we would like (including any height function we would like) so this is not an invalid thing to do. We will, however, further justify this choice in considering Fig. 5.14 and Fig. 5.15.

By computing the lapse associated with (5.4), we can solve for the derivative of the height function

$$\frac{dh}{dR} = \frac{2M\alpha - R\sqrt{\alpha^2 - f}}{\alpha f R} \tag{5.8}$$

(recall we do not need to know h itself). Note that this is one quantity which *is* different than that obtained by [30] as a result of starting with a different metric (as mentioned previously, the difference in the height functions of the two analyses accounts for the fact that a height function can be used to change from Schwarzschild coordinates to ingoing Eddington-Finkelstein coordinates). The expressions for components of the shift, spatial metric, and extrinsic curvature in terms of α and R end up being equal to those obtained by [30].

We apply a second coordinate transformation from the areal radial coordinate R to the a new quasi-

isotropic radial coordinate r' of the form $R = R(r')$. We require that this coordinate transformation makes the spatial line element conformally flat, giving

$$\frac{dR}{dr'} = \frac{\alpha R}{r'}.$$
(5.9)

Integral Solutions

Instead of using integral expressions for $r'(\alpha)$ as in [30], we solve the coupled system of ODEs (5.6) and (5.9) as functions of r'. Our boundary conditions are $r' \to R$ and $\alpha \to 1$ as $r' \to \infty$. Using r' as an integration variable and starting integration at a finite value makes it impossible to choose a starting value. We will see how the initial value for r' can be fixed with an overall multiplicative factor determined by the boundary conditions after integration has been carried out. Rewriting (5.9), integrating by parts, and making the appropriate choice for the integration constant, we obtain

$$r' = R^{1/\alpha} \exp\left[\int_{\alpha_C}^{\alpha} \frac{\ln R(\tilde{\alpha})}{\tilde{\alpha}^2} d\tilde{\alpha} - C_0\right].$$
(5.10)

If this is going to exhibit our desired behavior at large r' (i.e., $r' \approx R$), we see that

$$C_0 = \int_{\alpha_C}^{1} \frac{\ln R(\tilde{\alpha})}{\tilde{\alpha}^2} d\tilde{\alpha}$$
(5.11)

or, if we define k by requiring

$$\frac{dk}{dr'} \equiv \frac{\ln R}{\alpha^2} \frac{d\alpha}{dR} \frac{dR}{dr'},$$
(5.12)

we get

$$C_0 = \int_{r'_C}^{\infty} \frac{\ln R(r')}{\alpha(r')^2} \frac{d\alpha}{dR}(r') \frac{dR}{dr'}(r') dr' = \int_{r'_C}^{\infty} \frac{dk}{dr'} dr' = \lim_{r' \to \infty} k(r') - k(r'_C).$$
(5.13)

We also define $\tilde{r}$ in such a way that we can rewrite (5.10)

$$\tilde{r} \equiv r' e^{C_0} = R^{1/\alpha} \exp \int_{\alpha_C}^{\alpha} \frac{\ln R(\tilde{\alpha})}{\tilde{\alpha}^2} d\tilde{\alpha}.$$
(5.14)

By simultaneously integrating to find k (and therefore C_0), we can fix the value of r' after integration and use $\tilde{r}$ as our independent variable during numerical integration. Note that we can choose any $\tilde{r} \neq 0$ for the initial value.

In order to deal with the critical point, we start integration of the ODE at $\tilde{r}_C$ and integrate twice: once toward large $\tilde{r}$ and then again toward zero. We apply L'Hôpital's rule to (5.6) to find the derivative $\frac{d\alpha}{dR}\big|_{R_C}$

49

at the critical point

$$\frac{d\alpha}{dR}\bigg|_{R_C} \left[2(1-\alpha_C)R_C^2\right] = -R_C + M - 6R_C\alpha_C + R_C\alpha_C^2 + \left[8R_C^2(\alpha_C^2 - 1)(\alpha_C - 1)\right.$$

$$\left. + [M + R_C(\alpha_C^2 - 6\alpha_C - 1)]^2\right]^{1/2}. \tag{5.15}$$

The final form of the system we integrate is

$$\frac{dR}{d\tilde{r}} = \frac{\alpha R}{\tilde{r}} \tag{5.16a}$$

$$\frac{d\alpha}{d\tilde{r}} = -\frac{\alpha R}{\tilde{r}} \frac{2(3M - 2R + 2R\alpha^2)}{R(R - 2M + 2R\alpha - R\alpha^2)} \tag{5.16b}$$

$$\frac{dk}{d\tilde{r}} = -\frac{\ln R}{\alpha^2} \frac{\alpha R}{\tilde{r}} \frac{2(3M - 2R + 2R\alpha^2)}{R(R - 2M + 2R\alpha - R\alpha^2)}, \tag{5.16c}$$

with initial conditions $R(\tilde{r}_c) = R_c$, $\alpha(\tilde{r}_c) = \alpha_c$, and $k(\tilde{r}_c) = 0$, where $\tilde{r}_c = R_c^{1/\alpha_c}$ and we use (5.15) to avoid $\frac{0}{0}$. We then can compute $r' = \tilde{r}e^{-C_0}$ from $C_0 = \lim_{\tilde{r}\to\infty} k(\tilde{r})$.

We solve (5.16) numerically in Mathematica then output a lookup table of values for R, dR/dr', d^2R/dr'^2, d^3R/dr'^3, dh/dR, d^2h/dR^2, d^3h/dR^3 for a number of values of r'. We space the entries in this lookup table evenly in $\ln r'$, so that resolution is highest when interpolating near the puncture. Note dR/dr', dh/dR, etc., computed from R and α, could be computed in the C code. However, we find trouble with near-cancellation errors and therefore do these computations in Mathematica with better than double precision. This list of lookup table values is input to our C code.

Series Solutions

At large r', we know that $\alpha \to 1$ and $R \to r'$ are two of our boundary conditions. This allows us to say that $\alpha = 1 + u$, where u is some small correction. We plug this ansatz into (5.7a) and, keeping to order $\mathcal{O}(M/R)$, we find $u = -M/R$. We then take

$$\alpha \approx \alpha_1 + u = 1 - \frac{M}{R} + u, \tag{5.17}$$

plug in, keep to order $\mathcal{O}(M^2/R^2)$ in (5.7a), and iterate. We find

$$\alpha(R) = 1 - \frac{M}{R} - \frac{M^2}{2R^2} - \frac{M^3}{2R^3} + \frac{N - 160}{256}\frac{M^4}{R^4} - \frac{7M^5}{8R^5} + \frac{N - 672}{512}\frac{M^6}{R^6} + \frac{5N - 3168}{1536}\frac{M^7}{R^7}$$

$$+ \frac{N^2 + 768N - 439296}{131072}\frac{M^8}{R^8} - \frac{15N^2 - 21056N + 10982400}{1966080}\frac{M^9}{R^9} + \mathcal{O}\left(\frac{M^{10}}{R^{10}}\right), \tag{5.18}$$

50

where

$$N \equiv \left(3 + \sqrt{10}\right)^3 e^{4-\sqrt{10}} = C(2)^2 \frac{128e}{M^4} \approx 541. \tag{5.19}$$

Using a similar procedure with (5.9) and starting with $R \approx r' + u$, we find

$$\frac{R(r')}{M} = \frac{r'}{M} + 1 + \frac{M}{4r'} - \frac{N}{1024}\frac{M^3}{r'^3} + \frac{3N}{1280}\frac{M^4}{r'^4} - \frac{15N}{4096}\frac{M^5}{r'^5} + \frac{251N}{53760}\frac{M^6}{r'^6} - \frac{5N^2 + 11008N}{2097152}\frac{M^7}{r'^7}$$
$$+ \frac{77N^2 + 27912N}{5160960}\frac{M^8}{r'^8} - \frac{98361N^2 + 9855232N}{1887436800}\frac{M^9}{r'^9} + \mathcal{O}\left(\frac{M^{10}}{r'^{10}}\right). \tag{5.20}$$

Together, (5.18) and (5.20) give

$$\alpha(R(r')) = 1 - \frac{M}{r'} + \frac{M^2}{2r'^2} - \frac{M^3}{4r'^3} + \frac{N+32}{256}\frac{M^4}{r'^4} - \frac{17N+64}{1024}\frac{M^5}{r'^5} + \frac{207N+160}{5120}\frac{M^6}{r'^6} - \frac{4549N+960}{61440}\frac{M^7}{r'^7}$$
$$+ \frac{315N^2 + 1556992N + 107520}{13762560}\frac{M^8}{r'^8} - \frac{13573N^2 + 11167872N + 286720}{73400320}\frac{M^9}{r'^9} + \mathcal{O}\left(\frac{M^{10}}{r'^{10}}\right). \tag{5.21}$$

From (5.8) we also find

$$\frac{dh}{dR}(R) = \frac{2M}{R} - \frac{\sqrt{2N}-64}{16}\frac{M^2}{R^2} - \frac{5\sqrt{2N}-256}{32}\frac{M^3}{R^3} - \frac{47\sqrt{2N}-2048}{128}\frac{M^4}{R^4} - \frac{635\sqrt{2N}-24576}{768}\frac{M^5}{R^5}$$
$$+ \frac{3\sqrt{2N^3}-44644\sqrt{2N}+1572864}{24576}\frac{M^6}{R^6} + \frac{135\sqrt{2N^3}-965236\sqrt{2N}+31457280}{245760}\frac{M^7}{R^7} + \mathcal{O}\left(\frac{M^8}{R^8}\right) \tag{5.22}$$

and

$$\frac{dh}{dR}(R(r')) = \frac{2M}{r'} - \frac{\sqrt{2N}-32}{16}\frac{M^2}{r'^2} - \frac{\sqrt{2N}-48}{32}\frac{M^3}{r'^3} - \frac{7\sqrt{2N}-128}{128}\frac{M^4}{r'^4} + \frac{3N-34\sqrt{2N}+960}{1536}\frac{M^5}{r'^5}$$
$$- \frac{24N+925\sqrt{2N}-11520}{30720}\frac{M^6}{r'^6} + \frac{9\sqrt{2N^3}+1392N-5032\sqrt{2N}+107520}{491520}\frac{M^7}{r'^7} + \mathcal{O}\left(\frac{M^8}{r'^8}\right). \tag{5.23}$$

When substituting (5.18), (5.20), and (5.21), one can verify that

$$R' - \frac{\alpha R}{r'} = \mathcal{O}\left(\frac{M^{10}}{r'^{10}}\right) \tag{5.24}$$

$$\alpha(R)^2 - 1 + \frac{2M}{R} - \frac{C(2)^2 e^{\alpha(R)}}{R^4} = \mathcal{O}\left(\frac{M^{10}}{R^{10}}\right) \tag{5.25}$$

$$\alpha(R(r'))^2 - 1 + \frac{2M}{R(r')} - \frac{C(2)^2 e^{\alpha(R(r'))}}{R(r')^4} = \mathcal{O}\left(\frac{M^{10}}{r'^{10}}\right). \tag{5.26}$$
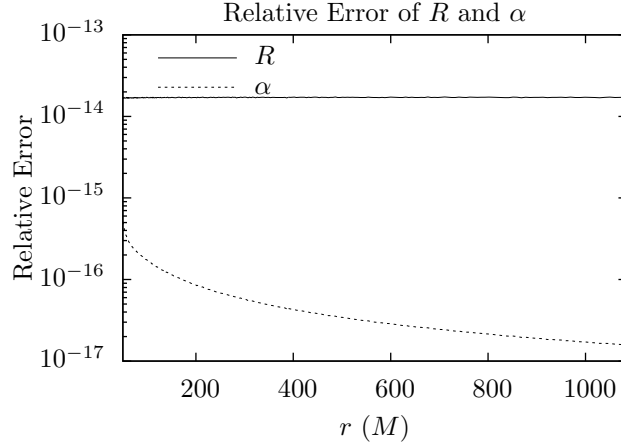
Figure 5.1: Relative error of R and α comparing the lookup table values (computed with numerical integration) with the asymptotic expansions.

We will use these expansions in order to examine the asymptotic properties of the boosted-trumpet coordinate system.

Because we have found so many terms in the preceding series, we find agreement between our numerically integrated and series solutions of at the level of a part in 10^{13} or better for all $r' > 50M$ for both α and R (see Fig. 5.1). This gives us confidence in our solutions, both numerical and series. It also means that the expansion is accurate, even surprisingly far from $r' = \infty$ (the point around which the expansion was done). When using the series to compute asymptotic properties of the coordinate system (i.e., the Weyl scalars and ADM measures) at $r \approx 100M$, we can have some confidence that the expressions are trustworthy.

Finally, we point out that, in this section, α was the lapse of the static spacetime and was thought of more as a sort of auxiliary variable which is helpful when computing dh/dR and R. Moving forward, we will use α to mean the lapse of our boosted-trumpet spacetime, and not this auxiliary variable.

5.1.2:   Adapting Trumpet Slicing to Moving Punctures Gauge: Boosted Black Hole

As mentioned at the beginning of the previous section and in [34], Kerr-Schild coordinates have nice properties under Lorentz boosts. We therefore begin construction of boosted-trumpet coordinates by Lorentz boosting Kerr-Schild coordinates using a standard Lorentz boost along the z-direction

$$\bar{t} = \gamma(\bar{t}' + v\bar{z}') \qquad\qquad \bar{x} = \bar{x}'$$

$$\bar{y} = \bar{y}' \qquad\qquad \bar{z} = \gamma(\bar{z}' + v\bar{t}'). \qquad (5.27)$$

52

We use a prime to distinguish a coordinate system in which the black hole is not Lorentz boosted. If we apply this coordinate change to (5.1), we see that it is form-invariant under the boost:

$$ds^2 = \left[\eta_{\bar{a}\bar{b}} + \frac{2M}{R} l_{\bar{a}} l_{\bar{b}} \right] dx^{\bar{a}} dx^{\bar{b}}, \tag{5.28}$$

where now

$$l_{\bar{a}} = \Lambda_{\bar{a}}^{\ \bar{b}'} l_{\bar{b}'} = \left(\gamma - \frac{v\gamma^2}{R} \left(\bar{z} - v\bar{t} \right), \frac{\bar{x}}{R}, \frac{\bar{y}}{R}, -v\gamma + \frac{\gamma^2}{R} \left(\bar{z} - v\bar{t} \right) \right), \tag{5.29}$$

and $R^2 = \bar{x}^2 + \bar{y}^2 + \gamma^2 \left(\bar{z} - v\bar{t} \right)^2$.

We would then like to apply a coordinate transformation analogous to (5.3). However, after the Lorentz boost, the singularity no longer stays at the origin of the coordinate system. Because the height function divergence is centered around the singularity the trumpet throats will also be centered around different $\bar{z}$ values for different $\bar{t}$ values. Consequently, if we apply the height function directly after the Lorentz boost, the spatial slices will intersect and not form a proper foliation, as shown in Fig. 5.2g. To get around this problem, we apply a Galilean boost in the opposite direction to the Lorentz boost. This shifts the spatial coordinates along with the black hole, keeping the singularity at the origin, while retaining the change in the shape of the time slicing associated with the Lorentz boost. We use the following relationships to make this coordinate change

$$\overline{T} = \bar{t} \qquad\qquad \overline{X} = \bar{x}$$

$$\overline{Y} = \bar{y} \qquad\qquad \overline{Z} = \bar{z} - v\bar{t}. \tag{5.30}$$

The capital letters denote a coordinate system in which both the (forward) Lorentz boost and backward Galilean boost have been applied.

It is now possible to apply analogues of the coordinate transformations discussed in §5.1.1. We apply the height function with the coordinate transformation

$$t = \overline{T} - h(R(\rho)), \tag{5.31}$$

while making no changes to the spatial coordinates. Note that the previous coordinate transformation made $R^2 = \overline{X}^2 + \overline{Y}^2 + \gamma^2 \overline{Z}^2$ time-independent. In addition to seeing that the puncture does not move through the coordinate system, consider that skipping the previous coordinate transformation would leave us with the equation

$$t = \bar{t} - h \left(\sqrt{\bar{x}^2 + \bar{y}^2 + \gamma^2 \left(\bar{z} - v\bar{t} \right)^2} \right), \tag{5.32}$$

(a) Kerr-Schild

(b) Boosted Kerr-Schild

(c) Lorentz Boost with reverse Galilean boost

(d) Trumpet time slicing

(e) Trumpet slicing and radial rescaling

(f) Final boosted-trumpet coordinate system

(g) If the reverse Galilean boost is not applied before the trumpet time slicing the spatial slices intersect.
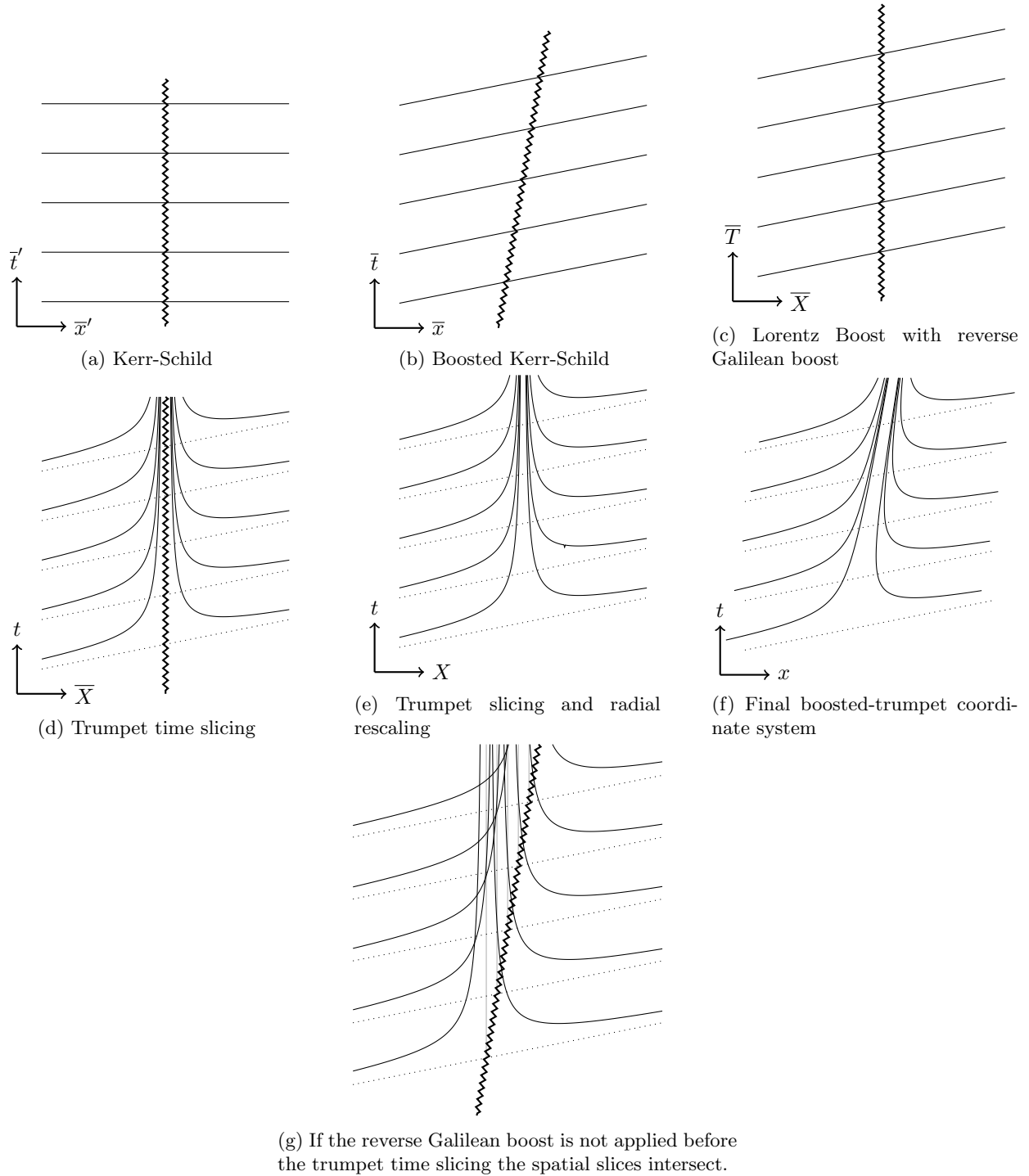
Figure 5.2: Surfaces of constant $\bar{t}'$ and $\bar{x}'$ in various coordinate systems. The zig-zag line shows the black hole's worldline. Fig. 5.2g shows why the height function cannot be applied immediately after the Lorentz boost (shown in Fig. 5.2b); the spatial slices intersect, as the divergence is centered at the location of the black hole. In contrast, if we apply a Galilean boost in the opposite direction (shown in Fig. 5.2c) the location of the puncture does not move so that the slices do not intersect when applying the height function (shown in Fig. 5.2d). Note the singularity is no longer covered by the coordinates after the radial rescaling is done (shown in Fig. 5.2e).

which leads to $\bar{t}(t)$ being multivalued. This is another way in which to see the importance of the reverse Galilean boost.

We next obtain a set of re-scaled coordinates X, Y, and Z by applying the radial scaling

$$X = \overline{X}\rho/R(\rho)$$
$$Y = \overline{Y}\rho/R(\rho) \tag{5.33}$$
$$Z = \overline{Z}\rho/R(\rho)$$

(with no change to the time coordinate), where the quasi-isotropic radius is

$$\rho^2 = X^2 + Y^2 + \gamma^2 Z^2. \tag{5.34}$$

Because there is no ρ such that $R(\rho) = 0$, this rescaling removes the singularity from the coordinate patch (and therefore simulation domain).

Finally, we set the puncture moving through the coordinate system again by reversing the Galilean boost, but doing so on the scaled X, Y, Z coordinates

$$x = X \qquad y = Y \qquad z = Z + vt. \tag{5.35}$$

This gives $\rho^2 = x^2 + y^2 + \gamma^2(z - vt)^2$ and explains the choice (5.34).

Summary

The sequence of coordinate changes is summarized in Table 5.1. By combining (5.27), (5.30), (5.31), (5.33), and (5.35), the relationship between the Kerr-Schild and the final boosted-trumpet coordinate system is given by

$$\bar{t}' = \gamma^{-1}[t + h(R(\rho))] - \gamma v(z - vt)R(\rho)/\rho \tag{5.36a}$$
$$\bar{x}' = xR(\rho)/\rho \tag{5.36b}$$
$$\bar{y}' = yR(\rho)/\rho \tag{5.36c}$$
$$\bar{z}' = \gamma(z - vt)R(\rho)/\rho, \tag{5.36d}$$

where $h(R(\rho))$ is given by (5.16b) and (5.8), $R(\rho)$ is given by (5.16a), and ρ is given by (5.34). This relationship allows us to go between the first and final coordinate systems without needing to reference the

	Sequence of Coordinate Changes
$\{\bar{t}', \overline{x}', \overline{y}', \overline{z}'\}$	Kerr-Schild
$\downarrow$	$\bar{t} = \gamma(\bar{t}' + v\overline{z}) \qquad \overline{z} = \gamma(\overline{z}' + v\bar{t})$
$\{\bar{t}, \overline{x}, \overline{y}, \overline{z}\}$	Lorentz boosted Kerr-Schild
$\downarrow$	$\overline{Z} = \overline{z} - v\bar{t} \qquad \overline{T} = \bar{t}$
$\{\overline{T}, \overline{X}, \overline{Y}, \overline{Z}\}$	Lorentz boosted Kerr-Schild
	with backward Galilean boost
$\downarrow$	$t = \overline{T} - h(R(\rho))$
$\{t, \overline{X}, \overline{Y}, \overline{Z}\}$	Lorentz boosted Kerr-Schild with
	backward Galilean boost
	and trumpet slicing
$\downarrow$	$X^i = \overline{X}^i \rho/R(\rho)$
$\{t, X, Y, Z\}$	Lorentz boosted Kerr-Schild with
	backward Galilean boost, trumpet
	slicing, and quasi-isotropic radius
$\downarrow$	$z = Z + vt$
$\{t, x, y, z\}$	Lorentz boosted Kerr-Schild with
	trumpet slicing and quasi-isotropic radius

Table 5.1: Sequence of coordinate changes described in the text. The relationship between each system is given to the right of the $\downarrow$.

intermediate systems (e.g., the bar and un-primed system, or the systems with capitals). Given (5.36), we can compute the relationships between the coordinate differentials and plug them into (5.1) to find the line element in terms of our new coordinates. We obtain

$$ds^2 = -f d\bar{t}'^2 + \left[dx^2 + dy^2 + \gamma^2(dz - vdt)^2\right] \frac{R^2}{\rho^2} + \left(\frac{dR}{d\rho} - \frac{R}{\rho}\right)\left(\frac{dR}{d\rho} + \frac{R}{\rho}\right)\left(\rho_{,a} dx^a\right)^2 \tag{5.37a}$$
$$+ \frac{4M}{R} \frac{dR}{d\rho} \left(\rho_{,a} dx^a\right)\left[d\bar{t}' + \frac{1}{2}\frac{dR}{d\rho}\left(\rho_{,b} dx^b\right)\right],$$

where the Kerr-Schild coordinate differential $d\bar{t}'$ is related to the boosted-trumpet coordinate differentials by

$$d\bar{t}' = \frac{dt}{\gamma} + \frac{1}{\gamma}\frac{dh}{dR}\frac{dR}{d\rho}\left(\rho_{,a} dx^a\right) - \gamma v(dz - vdt)\frac{R}{\rho} - \frac{\gamma v(z - vt)}{\rho}\left(\frac{dR}{d\rho} - \frac{R}{\rho}\right)\left(\rho_{,a} dx^a\right), \tag{5.37b}$$

and taking the derivative of (5.34) gives

$$\rho_{,a} dx^a = \frac{1}{\rho}\left[xdx + ydy + \gamma^2(z - vt)(dz - vdt)\right]. \tag{5.37c}$$

Equations (5.37) describe Schwarzschild spacetime in a boosted-trumpet coordinate system.

We will refer to a 'boosted-trumpet black hole' to mean a spacetime (or simulation) which took its initial data from this line element. and refer to a 'Bowen-York black hole' to mean a simulation which was initialized with Bowen-York initial data.

Section 5.2:   Setup for Numerical Simulations

Our simulations were done using the Somerville release of the Einstein Toolkit [1]. In addition to an initial data thorn we created, we made use of a number of preexisting thorns. These include (a modified) `McLachlan` [3] for evolution; `AHFinderDirect` [51, 52] to identify apparent horizons; (a modified) `QuasiLocalMeasures` [27] to measure ADM mass and momenta and apparent horizon properties; `WeylScal4` [19] to compute the Weyl curvature quantities $\mathcal{I}$ and $\mathcal{J}$ and, with `Multipole` [4], generate spherical harmonic amplitudes of gravitational waveforms; and `TwoPunctures` [16] to generate the canonical Bowen-York initial data against which we assess our work. In this section, we describe how we set up our simulations and relevant additions and modifications we have made to some of the code. Post-processing of data was carried out with the help of the `SimulationTools` package for Mathematica [5].

5.2.1:   Review of Initial Data Scheme Implementation in Code

With our metric and the numerical solutions in hand, we now turn to implementation of our initial data. We read off from our line element (5.37) the metric components g_{ab} in Mathematica. We then computed $g_{ab,c}$ and $g_{ab,cd}$ symbolically. The expressions for the components and their derivatives were written into a a C header file by Mathematica.

Because we have analytic expressions for our initial data (except for the numerical solutions for dh/dR and $R(\rho)$) our code essentially consists of a simple loop over the grid points. For every point, our code finds ρ from the location on the grid $\vec{x}$, time t (typically zero), and v. The code then interpolates to find $R(\rho)$, $dR(\rho)/d\rho$, $d^2R(\rho)/d\rho^2$, $d^3R(\rho)/d\rho^3$, $dh(R(\rho))/dR$, $d^2h(R(\rho))/dR^2$, and $d^3h(R(\rho))/dR$ using cubic spline interpolation from GSL [2]. We have lookup table values for higher derivatives and second derivatives of the metric in anticipation of needing them to compute the constraint violations when we eventually superpose the data and re-solve the constraint equations.

These lookup table values are plugged into the aforementioned expressions for g_{ab}, $g_{ab,c}$, and $g_{ab,cd}$. These are then used to compute the determinants γ and g, the inverse spatial metric γ^{ij}, and

$$\alpha = \sqrt{-g/\gamma} \tag{5.38a}$$

$$\beta^i = g_{0j}\gamma^{ij} \tag{5.38b}$$

$$\beta^i{}_{,t} = g_{0j,t}\gamma^{ij} + g_{0j}\gamma^{ij}{}_{,t} \tag{5.38c}$$

$$K_{ij} = \frac{1}{2\alpha}\left[-g_{ij,0} + g_{0j,i} + g_{0i,j} - \beta^l\left(g_{lj,i} + g_{il,j} - g_{ij,l}\right)\right] \tag{5.38d}$$

(with the product rule applied to find time derivatives of the above). Our C code is implemented as a thorn

in the Einstein Toolkit.

5.2.2: Modifying the Computation of ADM Mass and Momentum for Moving Black Holes

Two of the diagnostics with which we characterize our initial data are the ADM mass and momentum. They are only exactly defined in the limit of an integral over a surface at infinity. As we are not able to simulate all the way to infinity, we want to verify analytically that our data not only have the correct limit, but also have the same limiting behavior as found by `QuasiLocalMeasures` [27] in our simulations. There are a number of expressions – all of which have the same limit, but different asymptotic expansions.

We find that we are unable to analytically compute the expression used by `QuasiLocalMeasures` for our initial data. However, we did find expressions which we were able to work with both analytically as well as implement in a modified version of `QuasiLocalMeasures`. We use the expressions

$$M_{\text{ADM}}(r) = \frac{1}{16\pi} \oint_{\mathbb{S}^2(r)} \left[\delta^{ij} h_{kj,i} - \partial_k \left(\delta^{ij} h_{ij} \right) \right] \frac{x^k}{r} r^2 d\Omega^2 \tag{5.39}$$

(compare (3.11)) and

$$P_{\text{ADM}}{}^i(r) = \frac{1}{8\pi} \oint_{\mathbb{S}^2(r)} \delta^{ki} \left[\frac{1}{2} \left(h_{k0,j} + h_{j0,k} - h_{jk,t} \right) - \delta_{kj} \left(h_{l0,l} - \frac{1}{2} h_{ll,t} \right) \right] \frac{x^j}{r} r^2 d\Omega^2, \tag{5.40}$$

(compare (3.12)) where $M_{\text{ADM}} = \lim_{r \to \infty} M_{\text{ADM}}(r)$, $P_{\text{ADM}}{}^i = \lim_{r \to \infty} P_{\text{ADM}}{}^i(r)$, $r^2 = x^2 + y^2 + z^2$, and $x^i = (x, y, z)$. Additionally, the difference used by `QuasiLocalMeasures`, $h_{ab} \equiv g_{ab} - \eta_{ab}$, is not a perturbation but the exact difference. This will not change the asymptotic values, but it will affect the expansions.

Note that, although the ADM quantities are only defined in the $r \to \infty$ limit, we will refer to the expressions we obtain before the limit as if they were the ADM quantities for ease of discussion. Plugging the boosted-trumpet metric (5.37) with the expansions from §5.1.1 into (5.39) and (5.40) and having Mathematica perform series expansions and integrals, we obtain

$$
\begin{aligned}
M_{\text{ADM}}(r) = \gamma M &+ \frac{v \left[v^2 (14 - 32\gamma) + 32\gamma - 21 \right] + \left[96 - 59\gamma - 32v^4\gamma + v^2 (84\gamma - 64) \right] \sin^{-1} v}{32v} \frac{M^2}{r} \\
&+ \left[\frac{\sqrt{N} \left(2v^2 - 3 \right) (\gamma - 1)}{12\sqrt{2}\gamma} - \frac{\gamma \left(4v^4 + 25v^2 - 45 \right)}{60} \right] \frac{M^3}{r^2} \\
&+ \frac{1}{4096v} \left[N \frac{6v^3 - 9v + \left(4v^2 - 7 \right) \gamma \sin^{-1} v}{\gamma^2} \right. \\
&\qquad + \sqrt{N} \frac{16\sqrt{2} (\gamma - 1) \left[3v \left(2v^4 - 5v^2 + 3 \right) \gamma + \left(7 - 4v^2 \right) \sin^{-1} v \right]}{\gamma} \\
&\qquad \left. + 16 \left[v \left(4v^2 \left(v^2 - 5 \right) + 19 \right) + \left(13 - 10v^2 \right) \gamma \sin^{-1} v \right] \right] \frac{M^4}{r^3}
\end{aligned}
$$

58

$$-\frac{\gamma^2 N \left(64v^6 - 455v^4 + 910v^2 - 735\right) + 560\sqrt{2N}\left(4v^4 - 15v^2 + 15\right)(\gamma - 1)}{107520\gamma}\frac{M^5}{r^4}$$

$$+ \mathcal{O}\left(\frac{M^6}{r^5}\right), \tag{5.41}$$

$$P_{\mathrm{ADM}}{}^z(r) = \gamma v M + \frac{v\left[15 + 32v^4\left(1 - 2\gamma\right) - 32\gamma + 6v^2\left(16\gamma - 9\right)\right] + \left[32 + \left(8v^4 - 15\right)\gamma\right]\sin^{-1}v}{32v^2}\frac{M^2}{r}$$

$$- \frac{\gamma v\left[44v^2 - 80 + 4v^4 + 5\sqrt{2N}\left(2 - 3v^2 + v^4\right)(\gamma - 1)\right]}{120}\frac{M^3}{r^2}$$

$$+ \frac{1}{12288v^2}\left[v\left[-3N\left(-1 + v^2\left(3 - 2v^2\right)^2\right) - 48\sqrt{2N}\left(1 - 8v^2 + 4v^4\right)\left(\gamma^{-1} - 1 + v^2\right)\right.\right.$$

$$\left.+ 16\left(-15 + 8v^2\left(4 - 2v^2 + v^4\right)\right)\right] - 3\left[-80 + 224v^2 - 192v^4\right.$$

$$\left.\left. + N\left(1 + v^2 - 2v^4\right) - 16\sqrt{2N}\left(1 + v^2 - 2v^4\right)(\gamma - 1)\right]\gamma\sin^{-1}v\right]\frac{M^4}{r^3}$$

$$+ \frac{3N\left(105 - 112v^2 + 51v^4 - 8v^6\right)\gamma^2 - 280\sqrt{2N}\left(10 - 9v^2 + 3v^4\right)(\gamma - 1) + 448\left(5 - 6v^2 + v^4\right)\gamma^2}{53760\gamma/v}\frac{M^5}{r^4}$$

$$+ \mathcal{O}\left(\frac{M^6}{r^5}\right), \tag{5.42}$$

It is apparent that both (5.41) and (5.42) asymptotically approach the values expected for a boosted black hole of mass M. Comparing with the numerical results gives a powerful test of our initial data (see §5.5.1).

In our simulations, we measure $M_{\mathrm{ADM}}(r)$ and $P^z{}_{\mathrm{ADM}}(r)$ at at least four radii. We can then extrapolate to infinity by fitting to an asymptotic expansion with a few negative powers of r; the constant term gives a rough estimate for the value at infinity.

5.2.3: Interpreting Weyl Scalars for Moving, Off-Center Black Hole

We use the `WeylScal4` and `Multipole` thorns to compute $\mathcal{I}$, $\mathcal{J}$, and spherical harmonic modes of ψ_4 in our simulations. The fourth Weyl scalar

$$\psi_4 \equiv C_{abcd}n^a\overline{m}^b n^c\overline{m}^d, \tag{5.43}$$

where n^a is the radially ingoing null vector and $\overline{m}^a$ is the typical complex angular null vector, is tetrad dependent. It is only a scalar in the sense of a coordinate transformation which is applied to both the Weyl tensor and the tetrad basis vectors. On the other hand, the Weyl curvature invariants

$$\mathcal{I} = \frac{1}{16}C_{ab}{}^{cd}\left(C_{cd}{}^{ab} - \imath^*C_{cd}{}^{ab}\right) = 3\psi_2^2 - 4\psi_1\psi_3 + \psi_4\psi_0 \tag{5.44}$$

and

$$\mathcal{J} = \frac{1}{96} C_{ab}{}^{cd} C_{cd}{}^{ef} \left(C_{ef}{}^{ab} - {}^{*}C_{ef}{}^{ab} \right) = -\psi_2^3 + \psi_0\psi_4\psi_2 + 2\psi_1\psi_3\psi_2 - \psi_4\psi_1^2 - \psi_0\psi_3^2, \qquad (5.45)$$

where the dual is

$$^{*}C_{ab}{}^{cd} \equiv \frac{1}{2}\epsilon_{ab}{}^{ef} C_{ef}{}^{cd}, \qquad (5.46)$$

are true (tetrad independent) scalars [19, 37].

Because the boosted-trumpet coordinates describe a Schwarzschild spacetime, we can use scalars to compute the Schwarzschild areal radius R at every grid point. In Schwarzschild coordinates,

$$\mathcal{I} = \frac{3M^2}{R^6} \quad \text{and} \quad \mathcal{J} = \frac{M^3}{R^9}. \qquad (5.47)$$

Thus, at every point in our spacetime

$$R = \left(\frac{3M^2}{\mathcal{I}}\right)^{1/6} = \left(\frac{M^3}{\mathcal{J}}\right)^{1/9}. \qquad (5.48)$$

This cannot be done with the Bowen-York simulations, because the initial data there does not represent Schwarzschild spacetime, so (5.47) do not apply.

We must be careful in how we apply this in our numerical simulations though. The gauge conditions we use in a simulation (see §5.2.5) are not actually compatible with (5.37), so a simulated spacetime is not Schwarzschild spacetime. On the initial time slice, because of the initial data we specified for the differential gauge conditions, the numerical data exactly matches the analytic data on one time slice of Schwarzschild spacetime. At $t = 0$ in a simulation, $\mathcal{I}$ and $\mathcal{J}$ can be computed using only the initial data which we have specified and its spatial derivatives [19]. For the first time slice only then, we can compute R and interpret it as the areal radius coordinate in a Schwarzschild spacetime.

5.2.4: Using Apparent Horizon Circumferences as Measures of Horizon Distortion

We use `QuasiLocalMeasures` to compute the circumference of the apparent horizon in the xy-, xz-, and yz-planes

$$C_{xy} = \int_0^{2\pi} d\phi \sqrt{q_{\phi\phi} \left(\theta = \pi/2, \phi\right)} \qquad (5.49a)$$

$$C_{xz} = 2\int_0^{\pi} d\theta \sqrt{q_{\theta\theta} \left(\theta, \phi = 0\right)} \qquad (5.49b)$$

$$C_{yz} = 2\int_0^{\pi} d\theta \sqrt{q_{\theta\theta} \left(\theta, \phi = \pi/2\right)}, \qquad (5.49c)$$

60

where q_{AB} is the 2-metric on the apparent horizon

$$q_{AB} = \frac{\partial x^i}{\partial \theta^A} \frac{\partial x^j}{\partial \theta^B} \gamma_{ij} \tag{5.50}$$

and $A, B \in \{\theta, \phi\}$. We did not alter this part of `QuasiLocalMeasures`. Finding the circumferences (of our Schwarzschild black hole) in the usual Schwarzschild coordinates tells us that these circumferences should all be equal. Our coordinates are not Schwarzschild coordinates, so there may be some discrepancy in the circumferences we compute.

Additionally, we know that the lapse and shift we set initially do not correspond with the steady state lapse and shift our gauge conditions will settle to (because h and R which go into the calculation of $\alpha(t = 0M)$ and $\beta^i(t = 0M)$ were computed for the unboosted black hole). It is therefore possible that we may have created a black hole that is somewhat distorted. Since we are boosting along the z-axis, we expect that differences might manifest as $C_{xz} \neq C_{xy}$ or $C_{yz} \neq C_{xy}$.

5.2.5: Simulation Gauge Conditions

Advection in the 1+log slicing condition for the lapse

$$(\partial_t - \beta^i \partial_i)\alpha = -2\alpha K, \tag{5.51}$$

was necessary for the analysis leading to (5.6). If the advection term were not present, the assumption that the lapse settles down to a steady state would lead to $0 = -2\alpha K$; see Fig. 5.14. In order to compare our data with some of the results in [30] in Appendix 5.5, we switched this advection term off and on to produce Fig. 5.14 and Fig. 5.15. For all other simulations advection in the lapse gauge condition was turned on.

We also use the "shifting shift" hyperbolic Γ-driver condition for the shift vector

$$(\partial_t - \beta^j \partial_j)\beta^i = \frac{3}{4} B^i \tag{5.52a}$$

$$(\partial_t - \beta^j \partial_j)B^i = (\partial_t - \beta^j \partial_j)\tilde{\Gamma}^i - \eta B^i. \tag{5.52b}$$

While not as strictly necessary as advection was for the lapse condition, we do find that the long term stability of our simulations is much improved with advection turned on (i.e., the $\beta^i \partial_i$ terms present) in the Γ-driver equations. To produce Fig. 5.14 and Fig. 5.15, the "shiftless shift" Γ-driver with no advection was used. For all other simulations advection in the shift gauge condition was turned on. In all simulations we chose one of the following cases for η: $M\eta = 0$, $M\eta = 1$, or $M\eta = 2$.

5.2.6:   Bowen-York Initial Data as a Control

In order to see if the boosted-trumpet initial data we have constructed is an improvement over the Bowen-York data, we use `TwoPunctures` to generate a comparison. However, we were unable to get `TwoPunctures` to give initial data with only one black hole. To get around this, we utilized a basic configuration with a $1M$ black hole near the origin and a $10^{-4}M$ black hole very far ($2\,000M$) from the origin. We sought to compare our boosted-trumpet black hole with a single control Bowen-York black hole, and this approach to initialization is intended to provide this control as well as is possible. Other than the initial data thorns used, simulations for comparing the two types of initial data are otherwise identical.

5.2.7:   Grid Set Up

We next describe the standard set up for simulations, which varies between simulations due to changing parameters such as resolution.

We use five levels of refinement at the black hole puncture; this is on top of the the coarsest adaptive mesh refinement (AMR) level, which covers the entire simulation domain. We use $\Delta x = 0.8M$ and $\Delta t = 0.36M$ on the coarsest level. On the next finest level, we halve both so that the CFL parameter is the same. Each subsequent level is halved again, keeping the CFL parameter the same on all levels. The "radii" (half-length) of the AMR cubes are $\{0.9, 1.8, 3.6, 7.2, 14.4\}M$ (not including ghost zones).

For a single boosted black hole, we utilize the symmetry to reduce the size of the domain which must be simulated. The extent of the physical boundaries of the simulation domain is $[0M, 112M]$ along the x- and y-axes and $[-112M, 224M]$ along the z-axis, with reflection symmetry applied in the x- and y-directions.

When computing ADM quantities and spherical harmonic modes of Weyl scalars, we integrate over between four and ten spherical surfaces centered around the black hole's original location. These spheres have coordinate radii between $33M$ and $100M$ and are evenly spaced in $1/r$.

Section 5.3:   Resulting Properties of Boosted-Trumpet Coordinates and Improvements Compared to Bowen-York Initial Data

5.3.1:   Qualitative Description of Boosted-Trumpet Data Initially and After Evolution

Because we motivated the construction of our coordinate system by adapting it to the moving punctures gauge conditions, we expect our initial data to be much closer to the steady state of the differential gauge conditions. Fig. 5.3 shows that this expectation holds true. We compare a boosted-trumpet black hole with a Bowen-York black hole at early time and after some evolution. These figures show various quantities in
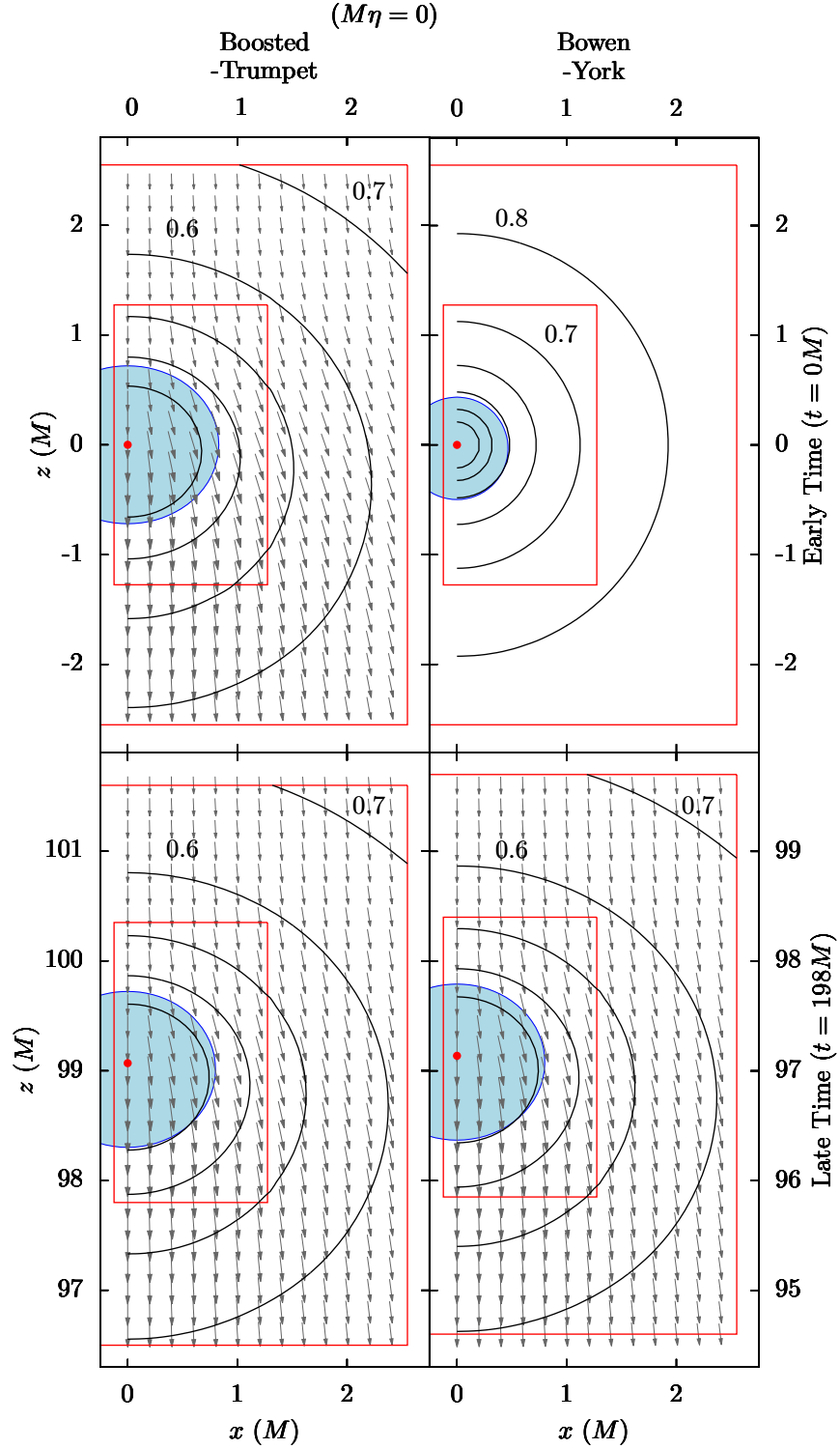
Figure 5.3: Equatorial slices showing lapse, shift, puncture location, apparent horizon, and AMR boundaries. Top images show the initial time slice and bottom images are at late time ($t = 198M$). Left images are for boosted-trumpet data and right images are for Bowen-York data. On the initial time slice for Bowen-York $\beta^i = 0$. In all cases, two of the lapse contours are labeled, other contours are evenly spaced in lapse value. All four slices have equal scales except that the two late time images are at different locations (because the Bowen-York black hole had a lower average speed than the boosted-trumpet black hole, see Fig. 5.7). In both cases, the black holes have $v = 1/2$ in the positive z direction.

the equatorial plane. Arrows show shift vectors ($\beta^y = 0$ in the $y = 0M$ plane), contours show level sets of the lapse, blue shaded regions show the trapped region with the outermost surface (apparent horizon) shown with a heavier line, the red dots show puncture location, and red boxes show AMR boundaries. In both simulations, the black hole is boosted in the positive z-direction, which is up in these plots.

Note that the features of the two types of black holes look qualitatively different at early time and similar at late time. In particular, at $t \approx 0M$ the apparent horizon of the boosted-trumpet initial data is Lorentz contracted along the direction of motion, compared to the apparent horizon for the Bowen-York initial data which looks more circular. Additionally, the shift vectors at early time are different (specifically, β^i is initially zero for the Bowen-York initial data). The shift vectors at late time in the boosted-trumpet simulation look similar to the shift vectors at early time in the same simulation, meaning that the boosted-trumpet black hole has not had to undergo as drastic of a realignment of the coordinate system as the Bowen-York black hole does. These observations indicate that the boosted-trumpet and Bowen-York black holes reach the same steady state of the gauge conditions but that the boosted-trumpet black hole starts out "closer" to this steady state.

5.3.2: Understanding Boosted Trumpet Gravitational Wave Due to Tetrad Offset and Discretization

We can use the expansions from §5.1.1 to obtain asymptotic expansions for the Weyl scalars by plugging (5.37) into (5.43) and doing the spherical harmonic projection. We start with a Graham-Schmidt process as outlined in (5.6) and (5.7) in [19] to find a spatial triad that is orthonormal with respect to the spatial metric derived from (5.37) and adapted to a spherical coordinate system.

Because of the computational complexity of finding the Weyl tensor from (5.37), we set $v = 1/2$ from the onset of the calculation. Through a brute force Mathematica computation, we find one spherical harmonic mode of ψ_4

$$
\begin{aligned}
\psi_4^{l=2,m=0}\left(v = 1/2\right) = &-\sqrt{\frac{5\pi}{2}}\frac{M}{4r^3}\left(27\ln 3 - 28\right) - \sqrt{\frac{5\pi}{2}}\frac{M}{24r^4}\left[\left(225\sqrt{3} - 142\pi\right)M + 12\left(27\ln 3 - 28\right)t\right] \\
&-\sqrt{\frac{5\pi}{2}}\frac{M}{1512r^5}\left[4\left(4493 - 960\sqrt{3}\right)M^2 + 126\left(130\pi - 261\sqrt{3}\right)Mt + 378\left(27\ln 3 - 28\right)t^2\right] \\
&+\mathcal{O}\left(\frac{M\left(M + t\right)^3}{r^6}\right).
\end{aligned}
\tag{5.53}
$$

Note that, because of the cylindrical symmetry, the $l = 2$, $m = 2$ mode is not dominant and we focus on the $l = 2$, $m = 0$ mode.

We see that $\psi_4 \neq 0$. At first glance this is unexpected for Schwarzschild spacetime, which (5.37) covers. In usual Schwarzschild coordinates, ψ_2 is the only non-zero Weyl scalar. However, the Weyl scalars are

only scalars in the sense of coordinate changes; they are still tetrad dependent. Utilizing the Gram-Schmidt orthonormalization procedure of [19] in different coordinate systems will yield different tetrads which are not related by a coordinate transformation. The five Weyl scalars computed using these two tetrads are therefore not related by a coordinate transformation either.

Furthermore, the tetrad used to do the projection is adapted to a spherical coordinate system that is centered around the origin, whereas a single boosted black hole moves away from the origin. When the centers of the tetrad and black hole are not aligned, the Weyl scalars (other than ψ_2) are no longer zero because of the contributions from different multipole orders. This problem does not exist in the case of binaries, where the center of mass of the two black holes stays near the origin. We will see that a single Bowen-York black hole suffers the same problem.

Another way to think about this is imagining two tetrads, one centered at the origin and one centered around the black hole. Each of the elements of the first tetrad will have projections onto multiple elements of the second tetrad. The Weyl scalars computed using the second tetrad can be computed as linear combinations of the the Weyl scalars computed using the first tetrad, given the sixteen tetrad projections. In particular, because the Weyl scalars computed with the second tetrad remain fixed with respect to the black hole and are therefore time independent, the Weyl scalars computed in the first tetrad must change throughout the simulation as well.

Physically, when the black hole gets near the radius at which a mode of ψ_4 is extracted (i.e., $t \approx r/v$), we expect the standard asymptotic interpretation of ψ_4 to break down. When the puncture crosses the extraction surface the expansion of the spacetime in multipoles makes little sense. We can see from (5.53) that, in this case, every term in the expansion becomes $\mathcal{O}\left(M/r^3\right)$ and the series will diverge.

In Fig. 5.4 we compare the analytic calculation (5.53) with a waveform from a simulation. We see that there is a smoothly varying, non-zero ψ_4. These plots show that the asymptotic expansion approaches the smooth trend in the numerical waveform as we add more orders. There are two main reasons for which the analytic and numerical results do not exactly align.

First, the analytic calculation is an expansion in large radius so we are committing an error by evaluating (5.53) at a finite radius. Looking at the form of the sub-leading terms in (5.53) shows one way in which this particularly breaks down: recall the understanding of the situation when $t \approx r/v$. Considering that this black hole is moving at $v = 1/2$, it makes sense that when $t \approx 2r$ and the black hole has crossed the surface on which ψ_4 is extracted and our interpretation of the expansion (5.53) is no longer valid. This is especially apparent in Fig. 5.4a, where the nature of the numerical waveform changes drastically around $t \approx 66M$.

Secondly, recall that we found h and R assuming an unboosted black hole. So we know that the lapse associated with (5.37) will not be exactly equal to the steady state solution of the 1+log slicing condition of
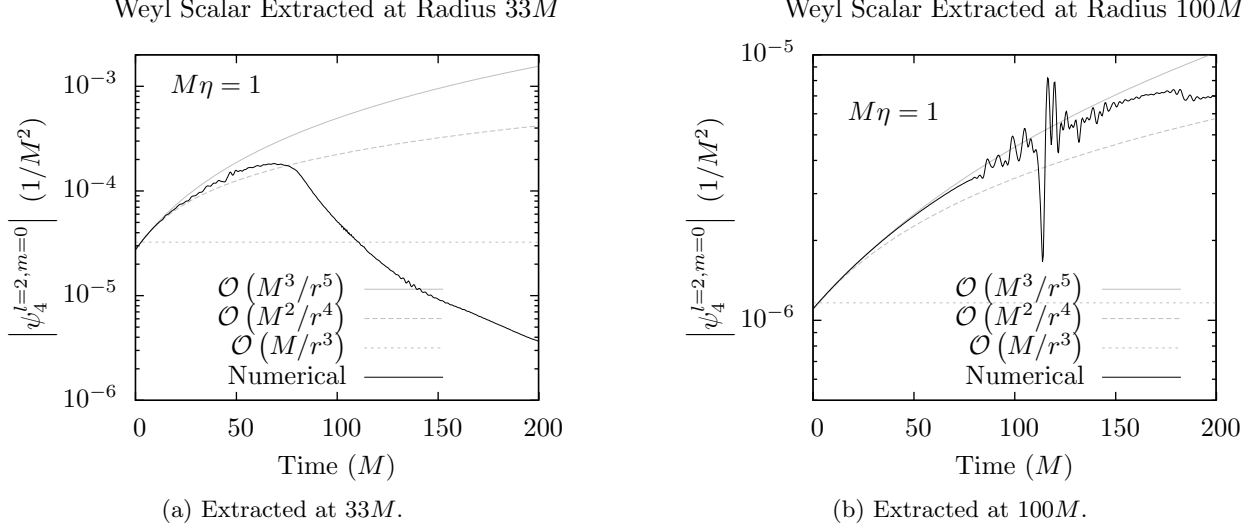
Figure 5.4: Comparison of analytic and numerical computations of gravitational waves. The left (right) subfigure show the $l = 2$, $m = 0$ mode of ψ_4 evaluated at a coordinate radius of $33M$ ($100M$). The black line is a numerical result from a simulation. The gray lines show approximations given by (5.53) to various orders. We can see the approximation (5.53) breaking down near $t \approx 66M$ ($t \approx 200M$), as discussed in in the text.

the simulation. In addition to the series truncation error, we are also committing an error because we have not done our analytic calculation in the same gauge as our simulation (indeed, the analytic and numerical calculations were not even done in the same spacetime, as was discussed in the last paragraph of §5.2.3). This effect will be smaller at larger radius where the lapse approaches unity and at earlier times where the numerical spacetime is in some sense closer to Schwarzschild.

Fig. 5.5 shows the $l = 2$, $m = 0$ mode of ψ_4 extracted at a coordinate radius of $100M$ for three simulations with varying resolution. We see that the slowly varying background offset of ψ_4 due to mixing with ψ_2 is already accurately converged and does not depend noticeably on resolution. The higher frequency signal imposed on top of the slow growth is, however, resolution dependent. This reinforces our understanding that the slow growth as due to the offset of the tetrad. It also indicates that the high-frequency part – evidence of a junk gravitational wave – is due primarily to discretization error and whatever small gravitational wave content our nearly-Schwarzschild spacetime has.

5.3.3: Reduced Junk Gravitational Wave

Fig. 5.6a shows the $l = 2$, $m = 0$ mode of the gravitational wave ψ_4 as a function of time, extracted at a radius of $33M$ for both a boosted-trumpet black hole and a Bowen-York black hole. Fig. 5.6b shows the same for an extraction radius of $100M$. We see that the Weyl scalar has much smaller amplitude for
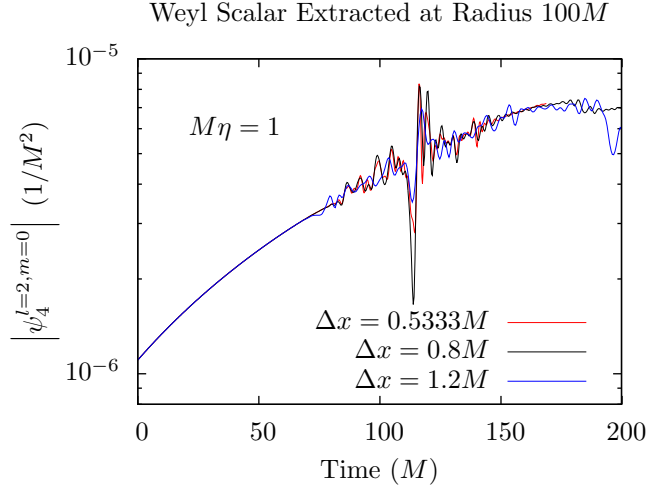
Figure 5.5: Resolution dependence of the $l = 2$, $m = 0$ mode of ψ_4 extracted from three simulations at coordinate radius $r = 100M$.

the boosted-trumpet black hole (by two or three orders of magnitude), especially when considering that the largest part of the signal in the boosted-trumpet case – the slow background growth – is indeed shared by the Bowen-York black hole.

5.3.4: Increased Accuracy of Black Hole Speed

Fig. 5.7 shows the speed of black holes as determined by the shift at the puncture. We can see a number of things from this plot. First, we see that the boosted-trumpet black hole's speed is more consistent with the anticipated final steady-state speed than is that of the Bowen-York black hole because the initial shift is non-zero. The Bowen-York black hole starts with a non-zero ADM momentum but has zero coordinate velocity (due to the initially zero shift). Secondly, it is evident that the η parameter in the Γ-driver condition plays a large role in the initial speed. Comparing the solid lines to the dashed lines, we see that the black hole reaches the anticipated speed much more quickly when $M\eta = 0$.

We have seen that the coordinate speeds of the boosted-trumpet black holes are initially more consistent with their momenta than are the speeds of the Bowen-York black holes. In addition, we find that boosted-trumpet black holes have a faster maximum speed than Bowen-York black holes. Sperhake, et. al. measure the speed of fast-moving Bowen-York black holes in terms of their Lorentz factors as computed from the momentum and irreducible mass [50]

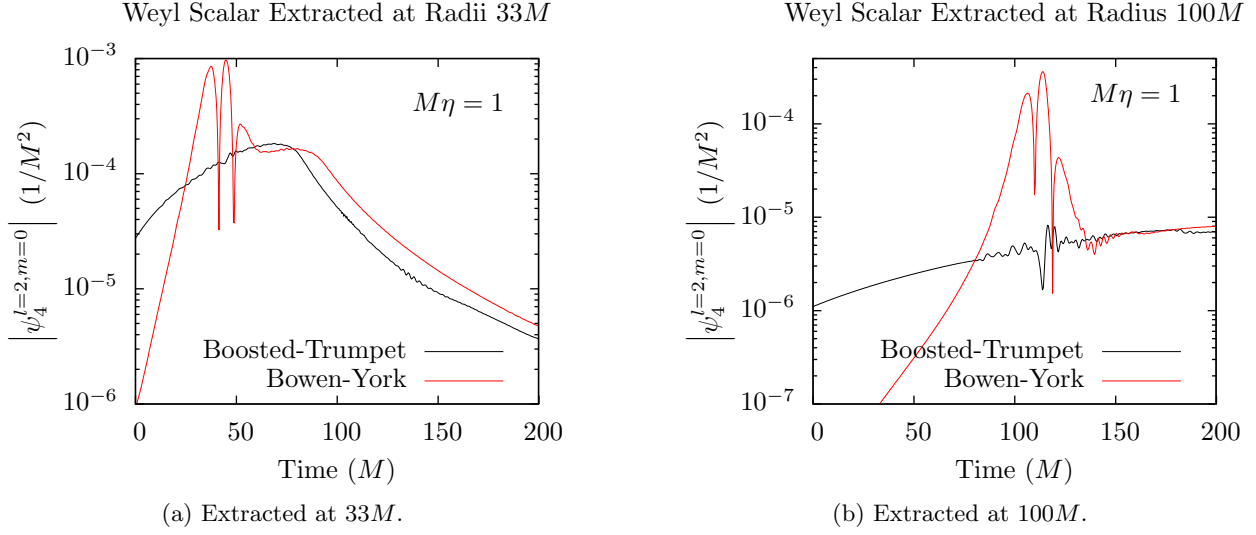$$\gamma = \sqrt{1 + \left(\frac{P_{\text{ADM}}}{M_{\text{irr}}}\right)^2}. \tag{5.54}$$

67

(a) Extracted at $33M$.

(b) Extracted at $100M$.

Figure 5.6: Dominant mode of the Weyl scalar ψ_4 extracted at coordinate radii $33M$ and $100M$. Note that the Weyl scalar computed in the Bowen-York simulations does indeed have the same background growth. This simulation uses $M\eta = 1$.
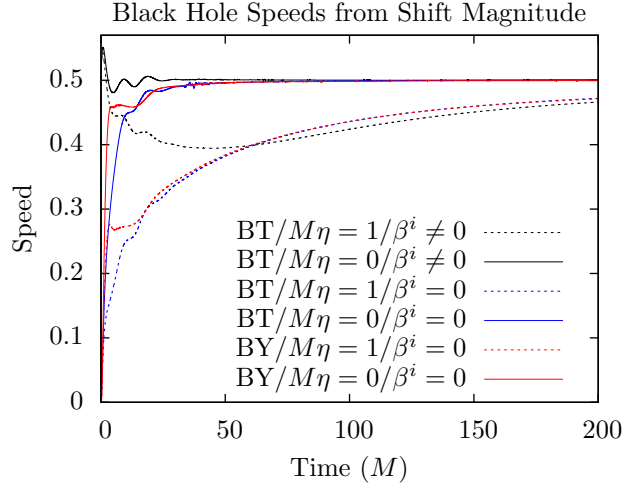

Figure 5.7: Speed of black holes computed from shift norm as a function of simulation time. These black holes have $v = 0.5$. Dashed lines correspond to simulations with $M\eta = 1$ and solid lines to simulations with $M\eta = 0$. Black lines are boosted-trumpet black holes, blue lines are boosted-trumpet black holes except with zero initial shift, and the red line is a Bowen-York black hole.
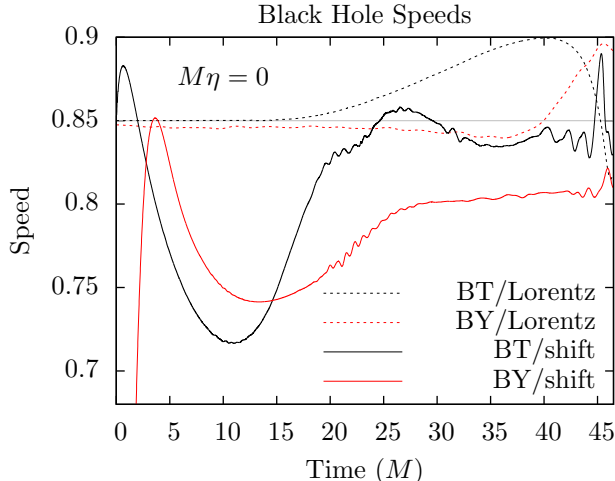
Figure 5.8: Speed of black holes with $v = 0.85$ as measured by shift and Lorentz factor (5.54) from $v = \sqrt{1 - 1/\gamma^2}$. These values are not accurate at late time because of the difficulty in extrapolating the ADM momentum when the black holes get closer to the extraction surfaces.

Instead of the Bowen-York momentum parameter, we substitute the (analytically equivalent for Bowen-York initial data [20]) ADM momentum because this is measurable in the simulation for both kinds of black holes.

From Fig. 5.8, we see that the speed as measured from the Lorentz factor is more accurate for both boosted-trumpet and Bowen-York black holes, especially at early time. However, we find this measure unreliable – especially at later times – for two main reasons. First, the ADM momentum includes momentum of the gravitational wave as well as that of the black hole. Thus, the speed inferred from the ADM momentum will be too large when gravitational radiation is present. Second, the ADM momentum is difficult to compute and the extrapolation to infinite radius is suspect when the black hole and gravitational waves get near the surfaces on which the ADM integral is computed. As such, when [50] discuss a Bowen-York black hole with $\gamma \approx 3$, we suspect that the coordinate velocity is less than $0.94 \approx \sqrt{1 - 1/3^2}$. Speed (as determined by shift) as functions of time for various boosted-trumpet black holes are shown in Fig. 5.9.

5.3.5:   Comparison of Apparent Horizons

In this final subsection, we consider a number of properties of the apparent horizons of the black holes in our simulations.

We can see a couple things from Fig. 5.10. First, the apparent horizon matches well the expectation that it lies near the event horizon at $R = 2M$. Second, the areal radius appears to have a limit near $1.3M$ at the location of the puncture ($z = 0M$). This is close to the trumpet radius $R(0M) = 1.3124M$ expected for a black hole with $v = 0$ found in setting $\alpha = 0$ in (5.7a).
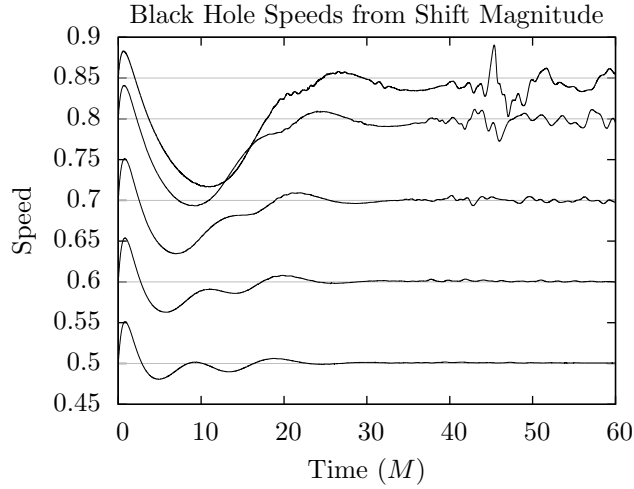
Figure 5.9: The speed of a boosted-trumpet black hole for a number of specified speeds.
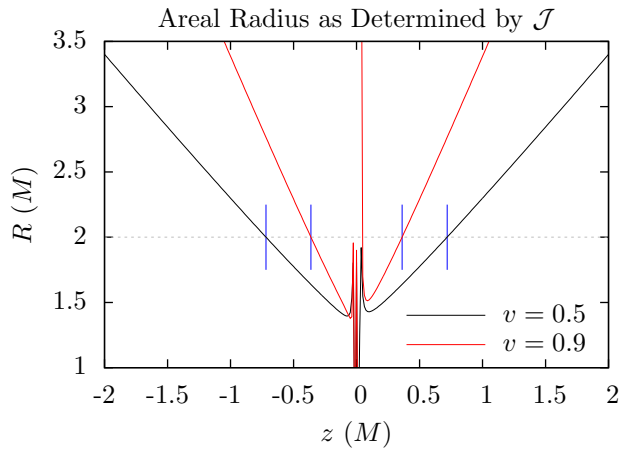
Figure 5.10: Areal radius as computed from $\mathcal{J}$ and (5.47) along the z-axis at time $t = 0M$ for boosted-trumpet black holes with $v = 0.5$ and $v = 0.9$. The blue vertical lines show the extent of the apparent horizon for the two black holes. The gray dashed line shows $R = 2M$, the location of the event horizon. Note that the finite difference used to compute derivatives when finding $\mathcal{J}$ will be inaccurate when applied across the puncture, so there are a few data points near the black hole which are invalid. We find visually indistinguishable results when computing R from $\mathcal{I}$. How $\mathcal{J}$ is computed in simulations is discussed in §5.2.3.

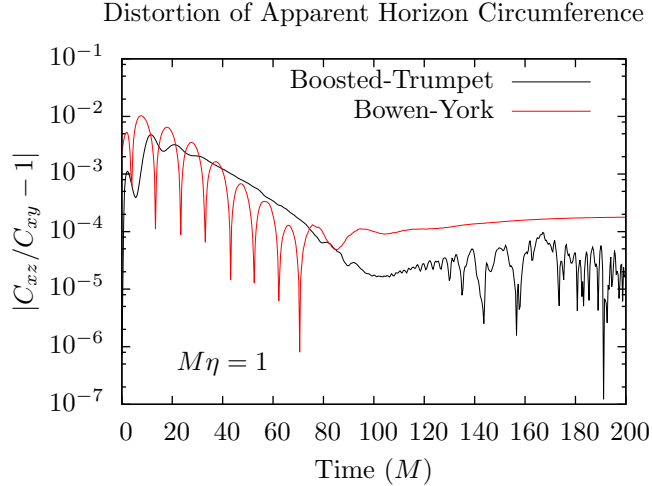Distortion of Apparent Horizon Circumference

Figure 5.11: Ratios of circumferences of the apparent horizon as functions of simulation time. These black holes have speeds set to $v = 0.5$. See (5.49) for how the circumferences are computed. We only show one of the two polar circumferences we could have computed here (i.e., we show C_{xz} but not C_{yz}); the analogous plot comparing C_{yz} and C_{xy} is indistinguishable by eye from this one. Note that the boosted-trumpet data has less distortion than the Bowen-York data both at early times and late times.

We see from Fig. 5.11 that the boosted-trumpet black hole starts out with no distortion. It is also apparent that the maximum distortion of the boosted-trumpet black hole is smaller than the maximum distortion of the Bowen-York black hole. The Bowen-York black hole is expected to be initially distorted due to the assumption of conformal flatness.

Additionally, we see evidence of quasi-normal ringing in the initially excited Bowen-York black hole. Fig. 5.11 shows a damped oscillation in the aspect ratio of the horizon. The circumferences C_{xz} and C_{yz} agree within a part in about 10^7, so we are confident that this effect is not a numerical artifact. Because the ratio oscillates above and below unity we can see that the horizon is oscillating between being oblate and prolate.

Section 5.4:   Summary Remarks About Boosted-Trumpet Black Holes

We have seen that it is possible to apply a Lorentz boost to the trumpet representation of a black hole which is adapted to the steady state of the moving punctures gauge conditions. Simulations initialized with initial data in the boosted-trumpet coordinate system are closer to the intended physical configuration than analogous simulations initialized with canonical Bowen-York initial data, as evidenced by more accurate coordinate speed and lower junk radiation content.

With the initial data for one black hole in hand, it should be possible to superpose this data in a manner described in [34]. Ideally, this will yield binary black hole initial data with lower initial junk radiation
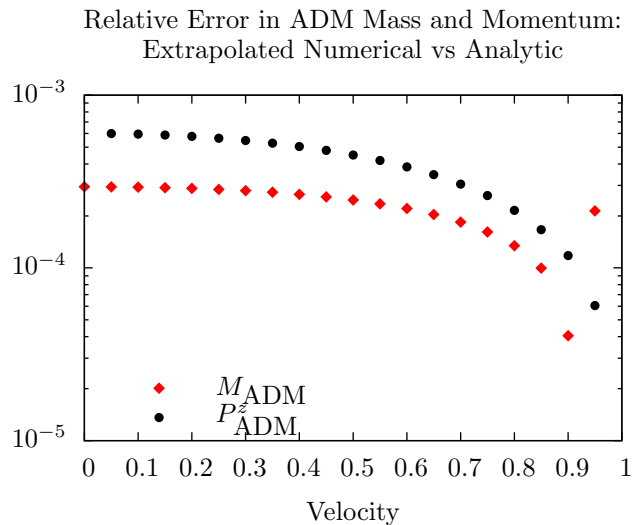
71

Relative Error in ADM Mass and Momentum:
Extrapolated Numerical vs Analytic

Figure 5.12: Relative error of simulated values of M_{ADM} and $P^z{}_{\text{ADM}}$.

content. This approach should in turn allow for more accurate waveform extraction and smaller simulation domains.

We also see some of the effects the η parameter in the Γ-driver condition can have on a simulation. The coordinate speed is much more accurate when $M\eta = 0$. We also found that the coordinate shape of the apparent horizon is very η dependent; when $M\eta = 0$ the horizon appears to maintain its shape (see Fig. 5.3) but when $M\eta = 1$ the horizon becomes stretched in the direction of motion. This happens for both the boosted-trumpet and Bowen-York black holes.

Section 5.5:   Code Validation

5.5.1:   ADM Quantities

Fig. 5.12 shows the relative error of the numerically extrapolated values compared with the analytic values for boosted-trumpet black holes with various velocities. Fig. 5.13 shows $M_{\text{ADM}}(r)$ vs $P^z{}_{\text{ADM}}(r)$ for two extraction radii and the extrapolated value alongside the analytic curve. Together, these figures give us confidence in our modifications to `QuasiLocalMeasures`, our construction of the boosted-trumpet spacetime, and the physical interpretation of the boosted-trumpet spacetime.

5.5.2:   Stationary Solution

We set $v = 0$ to do consistency checks with [30]. We find that, to double precision, there is no difference in the initial data we compute using an unboosted metric and the data we compute using the boosted metric
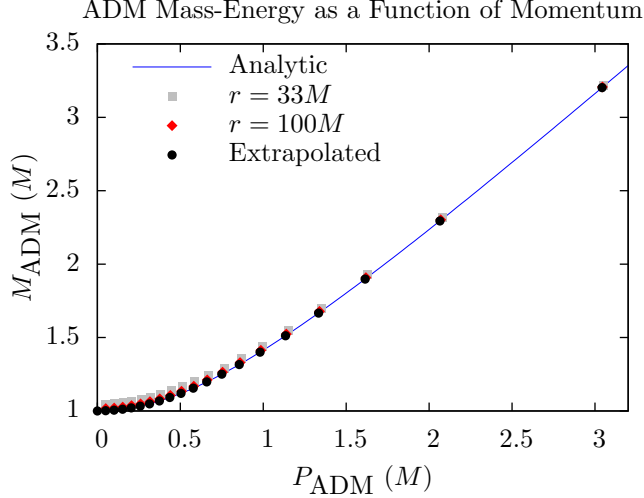
Figure 5.13: ADM mass-energy as a function of ADM momentum up to $v_{\text{max}} = 0.95$. The blue curve shows the analytic values expected from (5.41) and (5.42), black dots show the numerical values extrapolated to infinity, and red diamonds and gray squares show the numerical values calculated at $100M$ and $33M$, respectively. The values computed at $33M$ are much less accurate than the extrapolated values, but the values computed at $100M$ (which are mostly hidden by the extrapolated data points) are also less accurate than the extrapolated values.

but with $v = 0$. We find an initial apparent horizon radius of $r = 0.830404M$, in agreement with [30]. We also recreate Fig. 21 and Fig. 22 of [30] in our Fig. 5.14 and Fig. 5.15, respectively.

In addition to providing nice proof of concept, these figures demonstrate why we are confident in using the lapse of the unboosted black hole to determine our height function: both show how the data is robust with respect to changing gauge conditions. In both cases, when the gauge is changed the values jump but then undergo damped oscillation around their new value. Thus, if we are starting off with a height function determined by a slightly different gauge than we are using, we expect the discrepancy to relax away quickly after the simulation has begun.

5.5.3: Constraint Violation

Fig. 5.16 shows the violation of the constraints along the z-axis at time $t = 0M$. It is apparent that over most of the simulation domain the boosted-trumpet initial data has much smaller Hamiltonian constraint violation (as much as eight orders of magnitude) and slightly smaller z-momentum constraint violation than the Bowen-York data.

We point out that part of the power of the Bowen-York formalism is that the momentum constraint is satisfied by construction. However, our data satisfies both constraints by construction. It is therefore sensible that the momentum constraint violations are more comparable whereas we have improved much
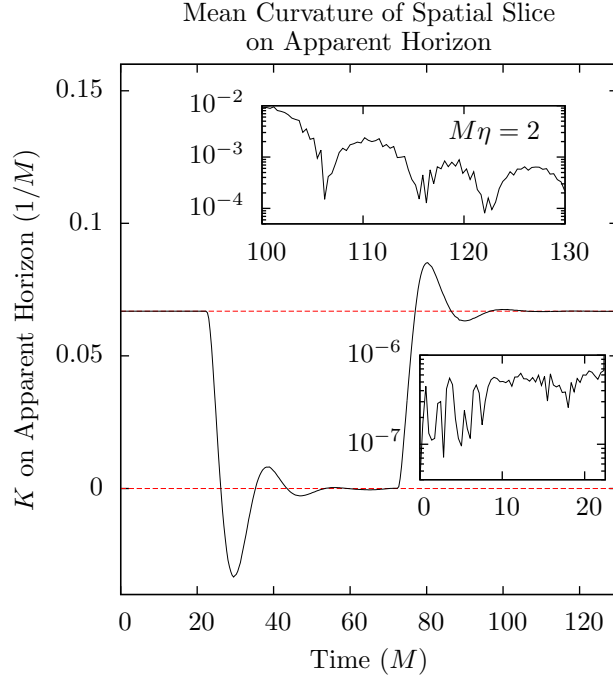
Figure 5.14: The average value of the mean curvature of the spatial slice at the location of the apparent horizon as a function of simulation time. This simulation starts with advection in the lapse gauge condition on, it is turned off at $t = 22.5M$ and back on again at $t = 72.5M$. This is intended as a consistency check with [30] (see their Fig. 21). It also has $M\eta = 2$ and advection turned off in the Γ-driver gauge condition. The insets show relative error as a function of time calculated as $|K(0) - K(t)|/K(0)$.
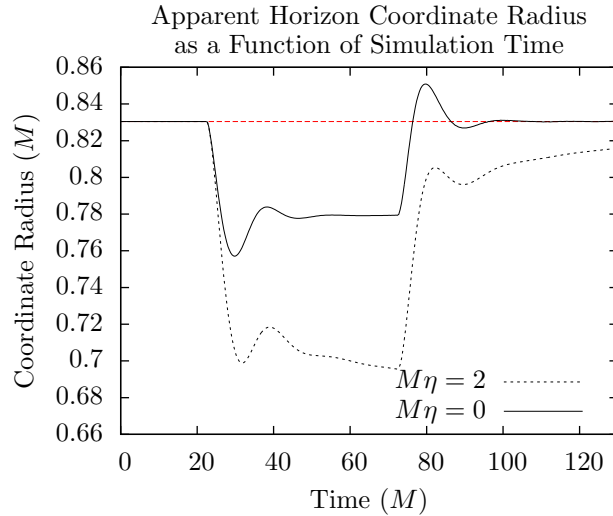
Figure 5.15: Coordinate radius of the apparent horizon as a function of simulation time. The simulations start with advection in the lapse gauge condition on, it is turned off at $t = 22.5M$, and back on again at $t = 72.5M$. This is intended as a consistency check with [30] (see their Fig. 22). Both simulations have advection turned off in the Γ-driver gauge condition. The solid line corresponds to $M\eta = 0$ and the short dashed line corresponds to $M\eta = 2$.

74

Figure 5.16: Violation of the Hamiltonian constraint H along the z-axis on the initial time step for boosted-trumpet (black) and Bowen-York (red) initial data. These black holes have $v = 0.5$ in the positive z direction.

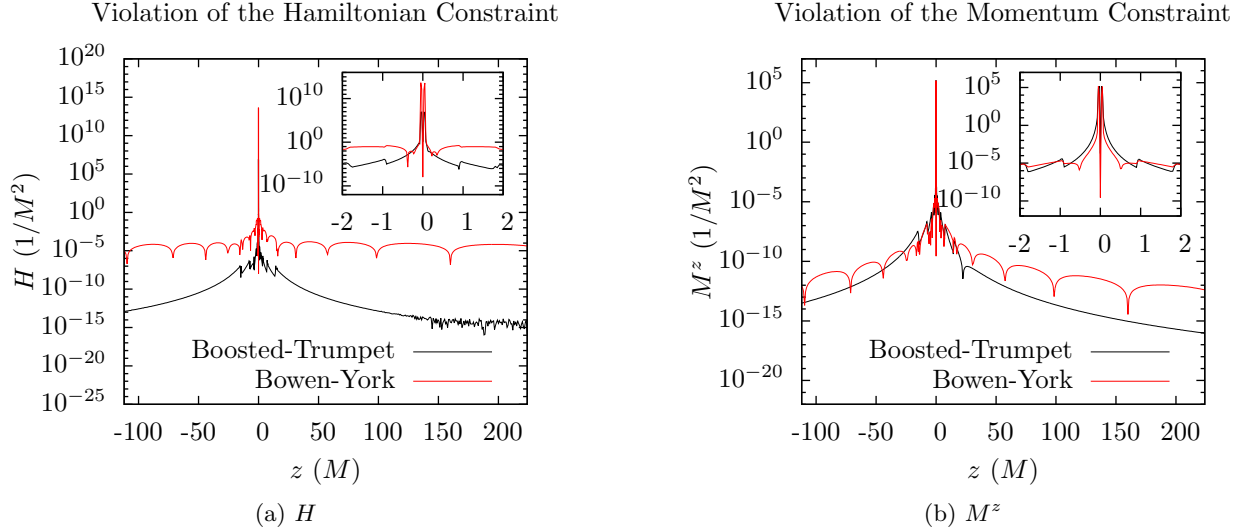more significantly the Hamiltonian constraint violation. The Hamiltonian constraint violation of the Bowen-York data is not only due to the finite differencing in computing H, but also the accuracy with which `TwoPunctures` was able to solve the constraint equation. When superposing boosted-trumpet data and re-solving the constraint equations, we expect the superposed boosted-trumpet data would have similar violation of the constraint.

Fig. 5.17 shows the resolution dependence of the violation of the Hamiltonian constraint H. Analytically, it should be zero, so any deviation should be due solely to the finite differencing used to calculate the Weyl tensor. The black curve has the standard grid spacing $\Delta x = 0.8M$ on the coarsest level, the red and blue curves have grid spacings of $\frac{2}{3}\Delta x$ and $\frac{4}{9}\Delta x$, respectively. With fourth order finite differencing, we expect the constraint violation to drop by a factor of $(2/3)^4$ when increasing the resolution by a factor of $3/2$. The figure also shows the constraint violation with this expected rescaling applied. This shows that finite differencing is indeed responsible for the constraint violations we have observed in the boosted-trumpet initial data. Note also that the boundaries of the AMR regions are visible. The discontinuities are caused by the change in grid spacing by a factor of two between the levels. We find similar results for the violation of the momentum constraint.
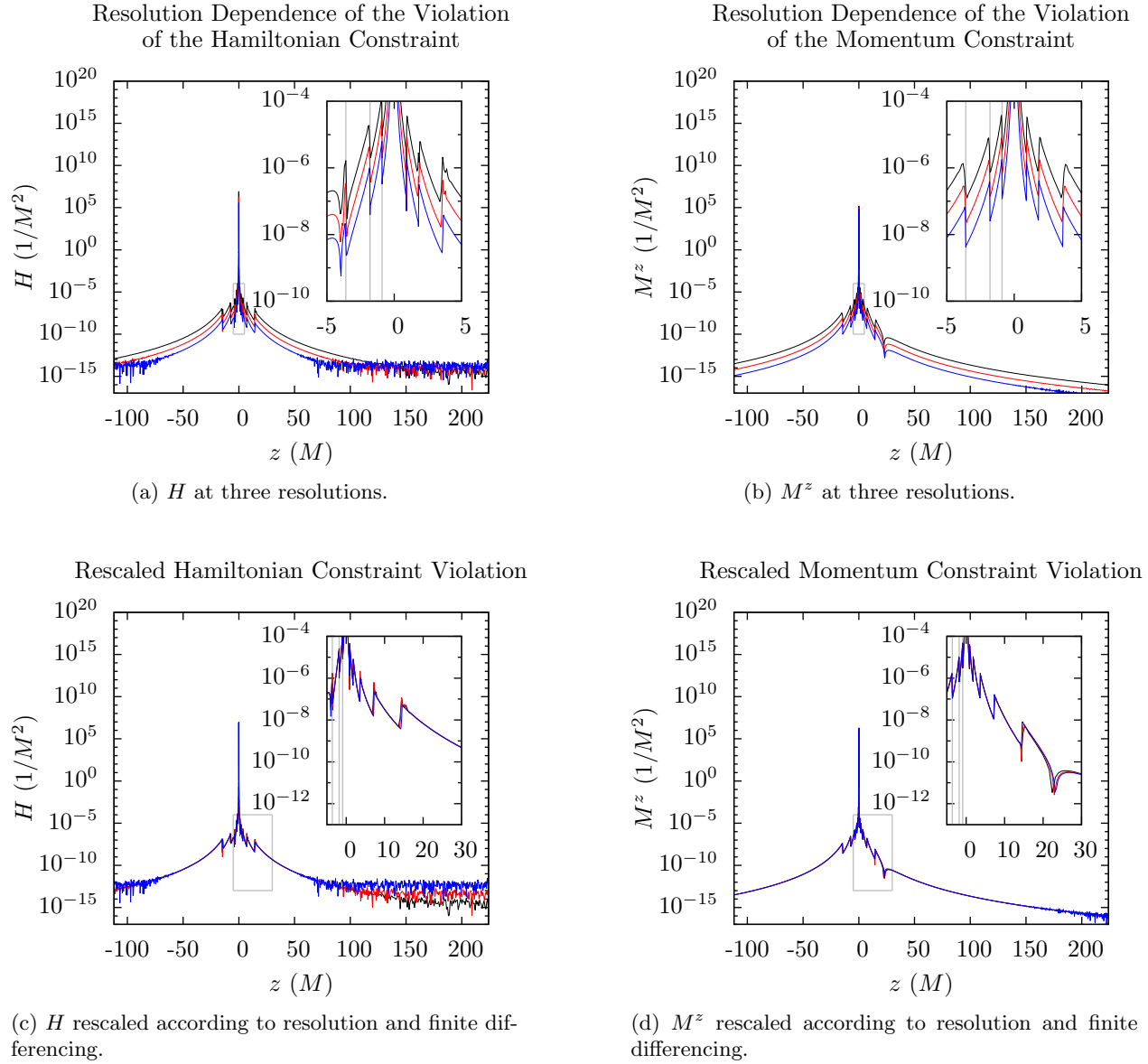
(a) H at three resolutions.

(b) M^z at three resolutions.

(c) H rescaled according to resolution and finite differencing.

(d) M^z rescaled according to resolution and finite differencing.

Figure 5.17: Top: Resolution dependence of the Hamiltonian constraint H and momentum constraint M^z along the z-axis on the initial time step for boosted-trumpet initial data. The black curve has grid spacing $\Delta x = 0.8M$ on the coarsest level, the red and blue curves have grid spacings of $\frac{2}{3}\Delta x$ and $\frac{4}{9}\Delta x$, respectively. These black holes have $v = 0.5$ in the positive z direction. In the inset, the AMR boundaries are shown on the left side by gray lines; AMR boundaries on the right side are not marked, but are at the same distances and should be visible as discontinuities in the curves. Bottom: Same except that the constraint violations from the medium and high resolution simulations have been multiplied by $(3/2)^4$ and $(9/4)^4$, respectively.

CHAPTER 6:   Superposing Initial Data

In section 6.1 we outline a scheme to approximately superpose initial data. This scheme produces data that violates the constraint equations, but we will see that we can reduce the violation to a level which is small enough that simulations can still be run. In section 6.2 we examine a binary inspiral which uses this approximate superposition scheme; we see that the junk radiation from a boosted-trumpet binary is smaller than that from a Bowen-York binary. We also discuss some of the limitations of the approximately superposed boosted-trumpet data.

Section 6.1:   Recipe for Approximate (Constraint-Violating) Superposition

We perform a superposition of two copies of our initial data, using a scheme similar to that laid out in [46]. In particular, we superpose our data using

$$\psi = 1 + f_1 \left(\psi^{(1)} - 1 \right) + f_2 \left(\psi^{(2)} - 1 \right) \tag{6.1a}$$

$$\tilde{\gamma}_{ij} = \delta_{ij} + f_1 \left(\tilde{\gamma}_{ij}^{(1)} - \delta_{ij} \right) + f_2 \left(\tilde{\gamma}_{ij}^{(2)} - \delta_{ij} \right) \tag{6.1b}$$

$$K = f_1 K^{(1)} + f_2 K^{(2)} \tag{6.1c}$$

$$\tilde{A}_{ij} = f_1 \tilde{A}_{ij}^{(1)} + f_2 \tilde{A}_{ij}^{(2)} \tag{6.1d}$$

$$\alpha = 1 + f_1 \left(\alpha^{(1)} - 1 \right) + f_2 \left(\alpha^{(2)} - 1 \right) \tag{6.1e}$$

$$\beta^i = f_1 \beta_{(1)}^i + f_2 \beta_{(2)}^i \tag{6.1f}$$

$$\partial_t \beta^i = f_1 \partial_t \beta_{(1)}^i + f_2 \partial_t \beta_{(2)}^i, \tag{6.1g}$$

where $\tilde{\gamma}_{ij}^{(1)}$ is the conformal spatial metric associated with the first black hole, etc. and

$$f_1 \left(\vec{r} \right) = 1 - e^{-(|\vec{r} - \vec{r}_2|/\omega_1)^4} \tag{6.2a}$$

$$f_2 \left(\vec{r} \right) = 1 - e^{-(|\vec{r} - \vec{r}_1|/\omega_2)^4} \tag{6.2b}$$

are functions which attenuate the contribution of the data from one black hole near the other black hole. Note that these definitions ensure that the superposed quantities have the same asymptotic properties as the original data for a single black hole. Fig. 6.1 is a flowchart which shows how the superposed data are

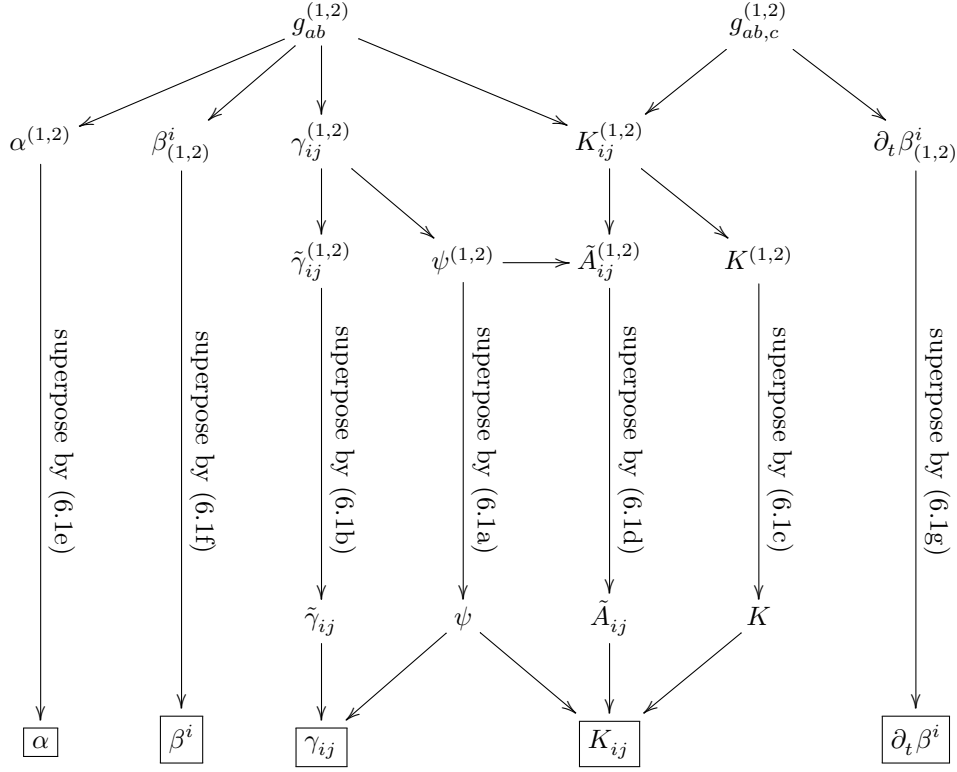computed from the data for two individual boosted-trumpet black holes.

Figure 6.1: Flowchart showing how superposed initial data is computed. The spacetime quantities are decomposed into the ADM quantities and then the conformal quantities. Then these conformal quantities are superposed according to (6.1) and finally the physical ADM quantities are reconstructed.

Because general relativity is a non-linear theory, the superposition of two solutions given above is not a solution. In order to find an exact solution to the constraint equations, the superposition would need to be corrected through the addition of terms such as

$$\psi = 1 + f_1 \left(\psi^{(1)} - 1 \right) + f_2 \left(\psi^{(2)} - 1 \right) + u \tag{6.3a}$$

$$\tilde{A}_{ij} = f_1 \tilde{A}_{ij}^{(1)} + f_2 \tilde{A}_{ij}^{(2)} + \left(\tilde{\mathbb{L}} b \right)_{ij}. \tag{6.3b}$$

These definitions would then need to be plugged into the constraint equations in order to solve for the corrections u and b^i. In practice, these corrections are small, especially if the black holes are initially widely separated so that the mutual field seen by each black hole is weak. Fig. 6.2 shows how increasing the
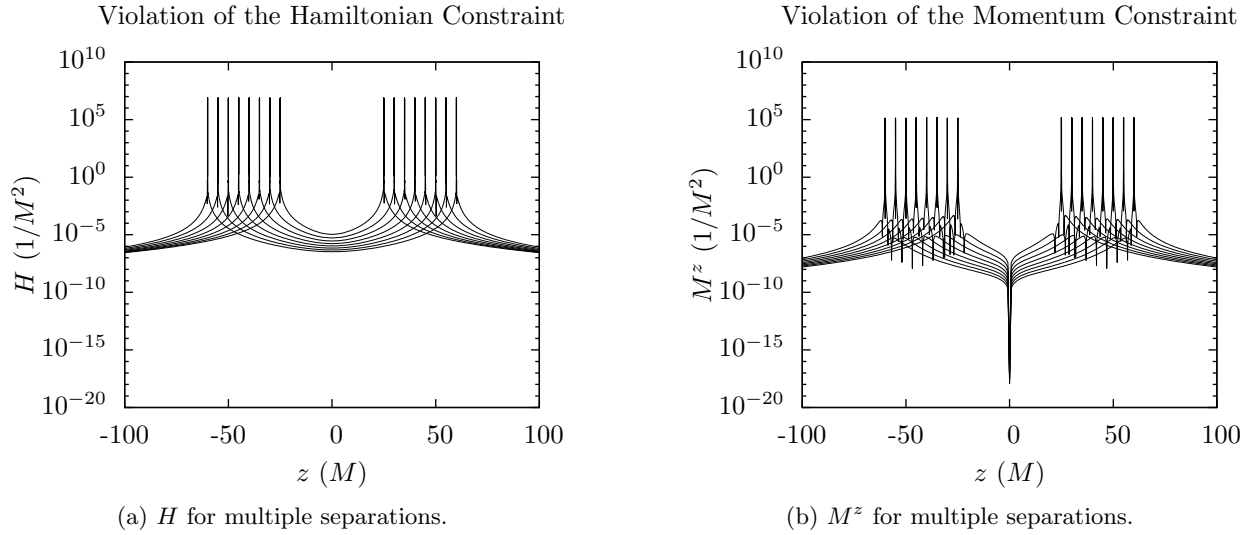
78

(a) H for multiple separations.

(b) M^z for multiple separations.

Figure 6.2: The violation of the constraint equations for two black holes superposed along the z-axis. Multiple simulations with varying separations between the black holes are show, all at the initial time. Note that as the black holes get further apart, the violation gets smaller.
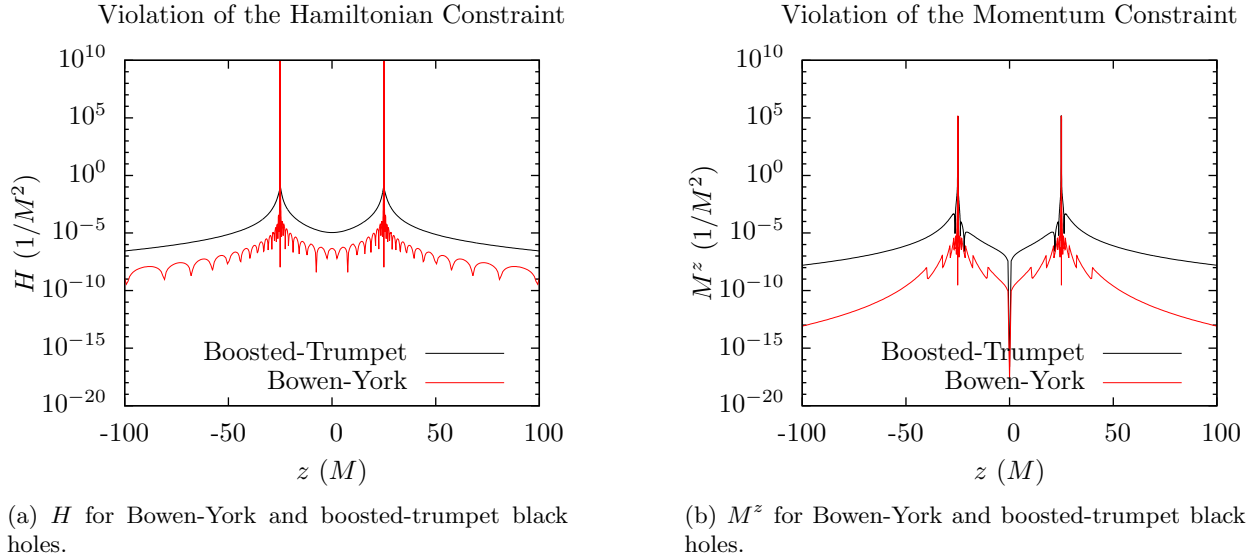

(a) H for Bowen-York and boosted-trumpet black holes.

(b) M^z for Bowen-York and boosted-trumpet black holes.

Figure 6.3: Violation of the Hamiltonian constraint with two black holes superposed along the z-axis, comparing Bowen-York initial data to boosted-trumpet initial data. Even without re-solving the constraint equations, the boosted-trumpet initial data violates the Hamiltonian constraint only by a couple orders of magnitude more than the Bowen-York data. The violation of the momentum constraint is comparatively much larger because Bowen-York data satisfies the momentum constraint by construction; the violation is therefore only due to the finite differencing used to compute the derivatives in the constraint equation (the AMR boundaries are visible where the resolution changes).

black hole separation decreases the constraint violation. Fig. 6.3 shows that, even for a relatively modest separation, the violations are only a couple orders of magnitude worse than the Bowen-York data (which satisfies the momentum constraint by construction and satisfies the Hamiltonian constraint by solving (2.69a) with (2.72)).

Section 6.2:   Preliminary Results for a Boosted-Trumpet Binary

Using the scheme outlined in the previous section, we are able to evolve a binary system formed from two boosted-trumpet black holes. This simulation does not, strictly speaking, provide a solution to Einstein's equation because the constraints are violated (by the superposition, not just by approximate methods for computing derivatives). Nonetheless, we see many interesting results from this simulation; indeed, modern initial data for neutron star simulations does not satisfy the constraint equations [53]. It is important to note that initial conditions for this simulation are symmetric under a π-rotation about the y-axis. In particular, the black holes have equal mass, are initially placed at $x = \pm 20.0125M$ (and $y = z = 0M$), and have initial velocities $v_z = \pm 0.1$ (and $v_x = v_y = 0$).

Equatorial snapshots are shown at four times in Fig. 6.6 (using the same conventions as Fig. 5.3). The paths of the punctures are shown throughout the entire simulation in Fig. 6.8. One of the most notable features of this binary simulation is the breaking of the symmetry of the trajectories of the punctures near the end of the simulation. This deviation is visible in the latest ($t = 1348M$) time slice in Fig. 6.6. It is also visible in Fig. 6.8, especially in the inset which shows the paths with a π-rotation applied to one of the trajectories; it is clear that the curves remain visually symmetric for much of the simulation then suddenly diverge.

No conclusion has been reached to explain this deviation. The constraint equations are violated, so errors may accumulate until instabilities are apparent. However, the violations of the constraints are symmetric, so it is not clear how this alone can lead to asymmetric behavior. Additionally, this does not appear to be a problem with Bowen-York initial data (see Figs. 6.7 and 6.9). Experimentation suggested that using the `RotatingSymmetry180` thorn could prevent such asymmetries from forming, but this was far from conclusive and leaves much to be desired as a solution.

Given that initially symmetric initial data (both boosted-trumpet and Bowen-York) leads to asymmetries, it would seem that the evolution model is one major factor. It is possible that roundoff errors in the construction of the boosted-trumpet data cause the initial data to be asymmetric at the level of machine precision and these asymmetries grow during evolution. The method of superposition does not treat the two black holes completely symmetrically on a numerical level: for one black hole, the initial data (e.g., $\beta^i_{(2)}$ or

$\gamma_{ij}^{(2)}$) undergoes a rotation whereas the other (e.g., $\beta_{(1)}^i$ or $\gamma_{ij}^{(1)}$) does not. On the other hand, the spectral methods used by `TwoPunctures` in the construction of Bowen-York data should give initial data which is more symmetric, even at a numerical level.

Fig. 6.4 shows that the Bowen-York initial data is indeed more symmetric than the boosted-trumpet initial data and that there is a growing asymmetry throughout the evolution, though it is not visually apparent from Fig. 6.9. This figure further reinforces the idea that the asymmetry issue may not be tied to the type of initial data: both binaries reach a comparable level of asymmetry near $t \approx 20 - 50M$ and both binaries grow more and more asymmetric throughout evolution.
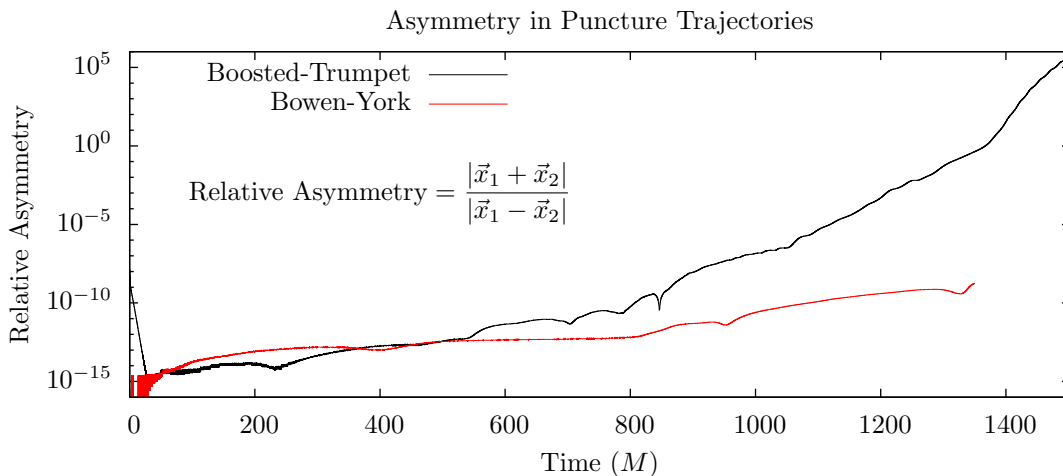

Figure 6.4: The growth in the asymmetry of the puncture trajectories for both boosted-trumpet and Bowen-York black hole binaries. Since it should be symmetric about the y-axis, the sum of the puncture locations should be zero $\vec{x}_1 + \vec{x}_2 = 0$. Given that this is a semi-log plot, it appears that the asymmetry in both binaries is growing approximately exponentially (though, the asymmetry in boosted-trumpet binary may be super-exponential).

Fig. 6.5 shows the gravitational wave (the $l = 2$, $m = 2$ mode of ψ_4) at a radius of $100M$ for simulations which used both kinds of initial data. The $l = 2$, $m = 0$ mode is not dominant as it was in the previous Chapter, where we were considering a cylindrically symmetric single boosted black holes. For both kinds of data, the background growth from the offset of the tetrad from the origin of the black hole is no longer an issue, as we anticipated in §5.3.2.

The small oscillations at $t \approx 100M$ show that there is some junk radiation in both binaries. Even with constraint-violating data, the junk radiation content of the boosted-trumpet data is smaller than that of the Bowen-York data (by approximately a factor of two here, as compared with the approximately two orders of magnitude we saw for the single black holes in the previous Chapter). The boosted-trumpet data shows a large pulse starting at $t \approx 1300M$ coming from the strong interaction near merger. The pulses near $t \approx 500M$

Weyl Scalar Extracted at Radius $100M$

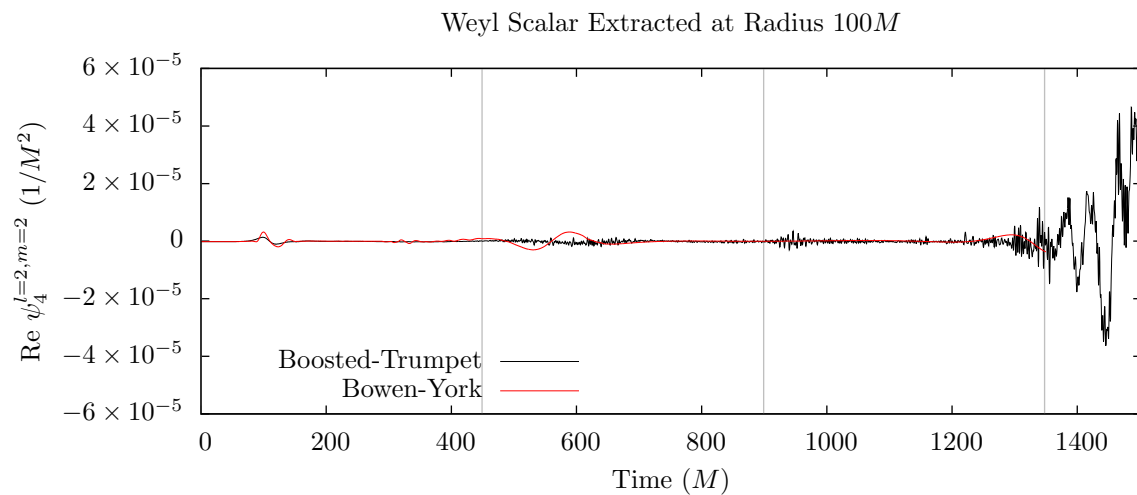Figure 6.5: The real part of the $l = 2$, $m = 2$ mode of ψ_4 extracted at a radius of $100M$ for the binary boosted-trumpet and Bowen-York black holes. Grey lines correspond to the times shown in Fig. 6.6 and Fig. 6.7. The Bowen-York data ends due to CPU-hour constraints, not because of physical or numerical limitations.

and $t \approx 1300M$ in the Bowen-York signal come from the close (non-merger) interactions.
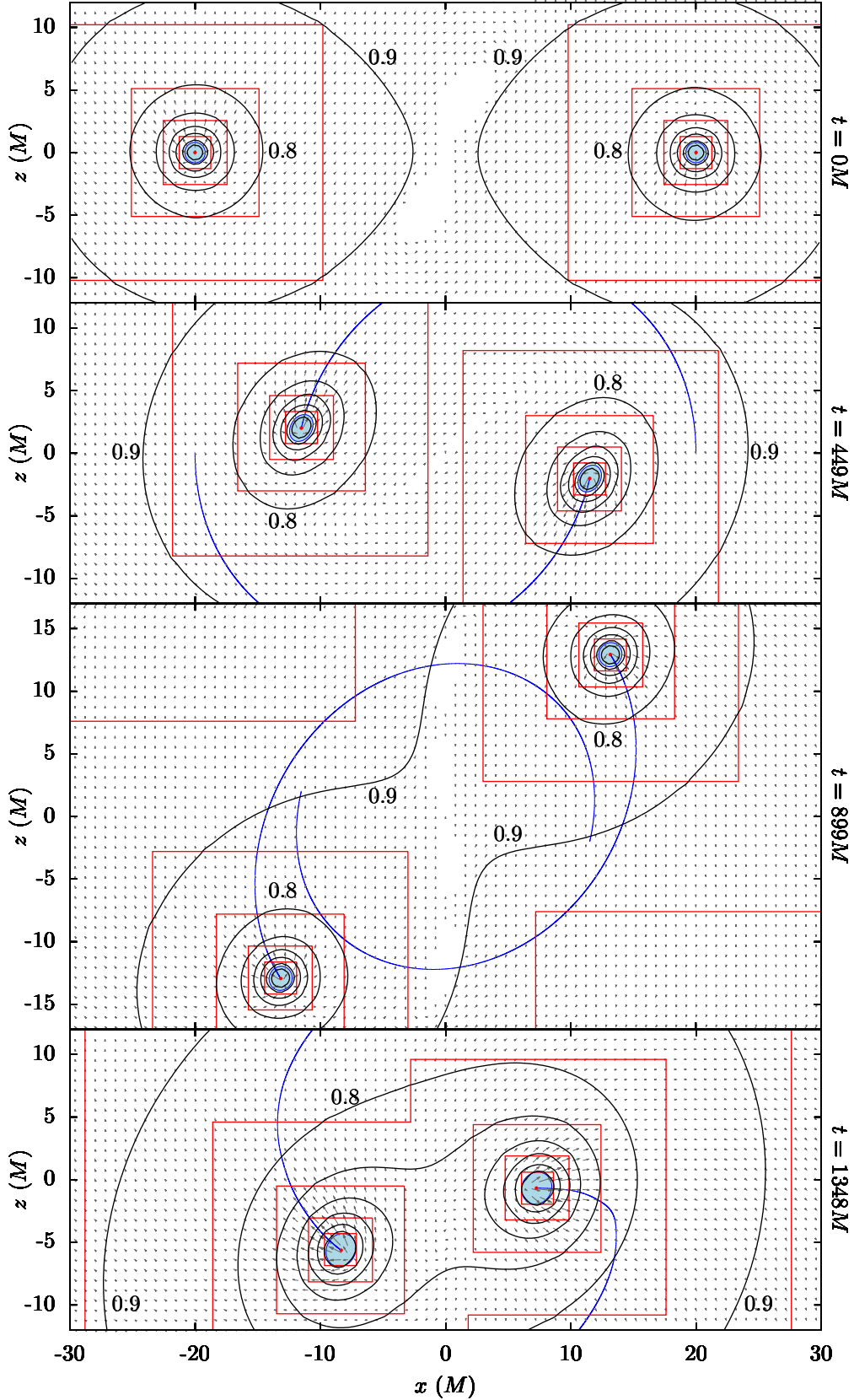
Figure 6.6: Equatorial slices showing evenly spaced level sets of the lapse (with labels), shift vectors, puncture locations, puncture trajectories (between snapshots), apparent horizons, and AMR boundaries at four times throughout evolution. The asymmetry in the trajectories is apparent in the last frame.

83
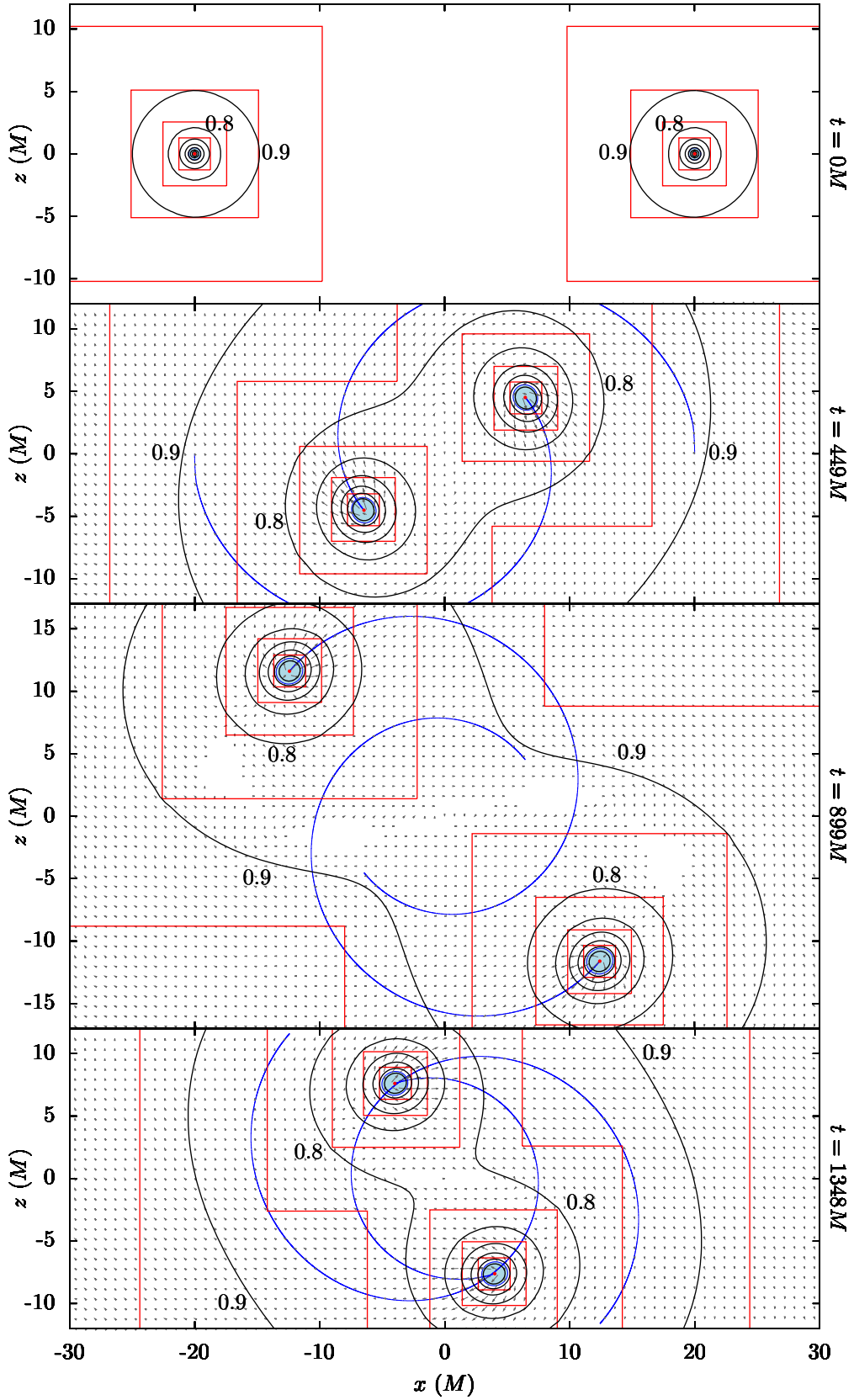
Figure 6.7: Same as Fig. 6.6 except with Bowen-York initial data.
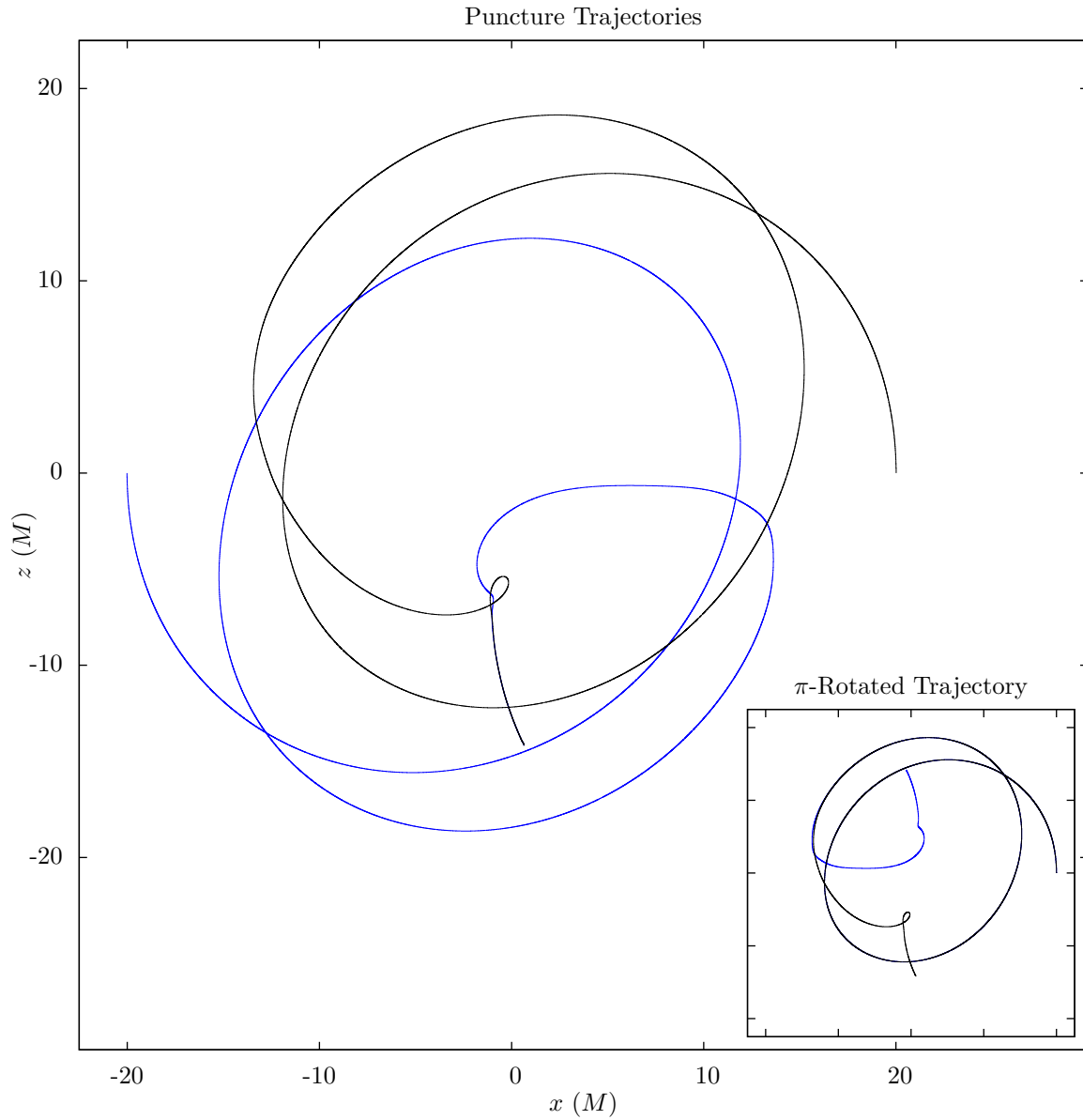
Figure 6.8: The trajectories of the punctures in the binary simulation. Initial data was symmetric under a rotation of π about the y-axis. The trajectories do not retain this symmetry though. This is particularly evident in the inset, where one trajectory has been rotated so that the two trajectories initially line up.

Figure 6.9: Same as Fig. 6.8 except with Bowen-York initial data. In the inset, the π-rotated trajectory is visually coincident with the other trajectory (though, see Fig. 6.4 for evidence that there is a growing asymmetry even in the Bowen-York black hole trajectories).

CHAPTER 7:   Conclusions

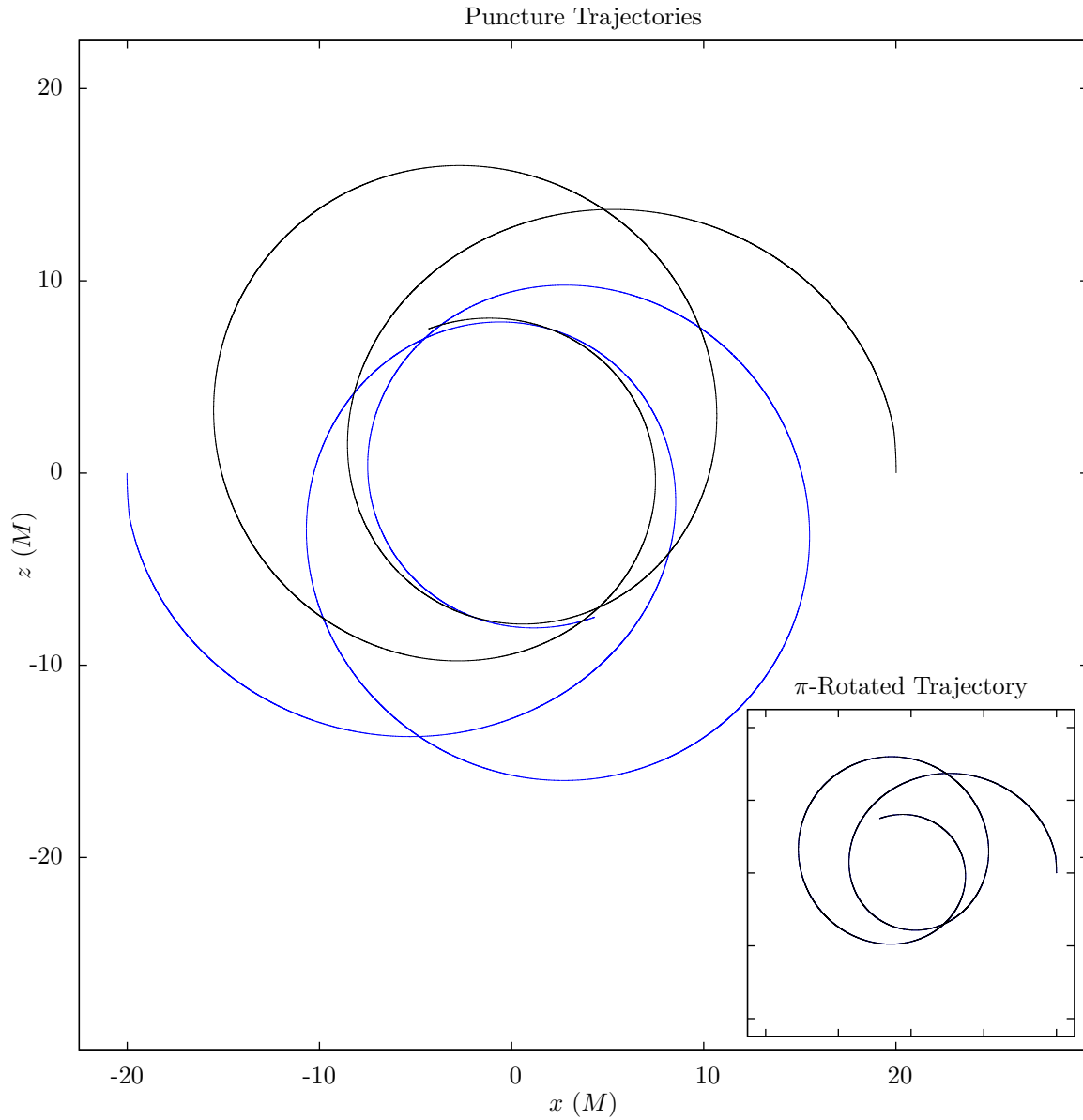We discuss in section 7.1 future directions that Boosted-Trumpet initial data can take before making concluding remarks in section 7.2.

Section 7.1:   The Future of Boosted-Trumpet Initial Data

We consider three important extensions for boosted-trumpet initial data: superposed data in §7.1.1, velocities in arbitrary directions in §7.1.2, and spinning black holes in §7.1.3. The ideas are discussed to the extent they have been developed so far in this project and considerations which are anticipated to be important for further development are laid out.

7.1.1:   Boosted-Trumpet Binaries

We have already talked some about using boosted-trumpet initial data to construct binary systems in section 6.2. We saw there that a rough superposition without re-solving the constraint equations did allow for a simulation, though it was not without its problems. We also outlined in that section a recipe which uses this rough superposition as a starting point for a solution which does satisfy the constraint equations. Numerical solvers for elliptic partial differential equations (such as the `CT_Multilevel` thorn [21] or a modified `TwoPuncture` such as in [46]) can be used to find solutions to the fully general (elliptic) constraint equations.

7.1.2:   Black Hole With Trumpet Slicing Boosted in an Arbitrary Direction

The data presented in Chapter 5 only allows for a black hole which has been boosted in the z-direction. For a single black hole, this is not such a big deal as the symmetry allows us to call whatever axis we like (i.e., the boost axis) the z-direction. However, as soon as we have two black holes, this symmetry is broken and we need to be able to control the direction of boost. This point was somewhat swept under the rug in Chapter 6, where the rotation matrix

$$\mathbf{R}\left(\vec{v}=-v\hat{z}\right) = \begin{pmatrix} 1 & 0 & 0 \\ 0 & -1 & 0 \\ 0 & 0 & -1 \end{pmatrix} \tag{7.1}$$

was applied to the initial data for one of the black holes before the superposition.

We want the black hole to have a velocity vector $\vec{v} = (v_x, v_y, v_z)$. The transformation matrix is a series of rotations

$$\mathbf{R}(\theta_v, \phi_v) = \begin{pmatrix} \cos\phi_v & -\sin\phi_v & 0 \\ \sin\phi_v & \cos\phi_v & 0 \\ 0 & 0 & 1 \end{pmatrix} \begin{pmatrix} \cos\theta_v & 0 & \sin\theta_v \\ 0 & 1 & 0 \\ -\sin\theta_v & 0 & \cos\theta_v \end{pmatrix} \begin{pmatrix} \cos\phi_v & -\sin\phi_v & 0 \\ \sin\phi_v & \cos\phi_v & 0 \\ 0 & 0 & 1 \end{pmatrix}^{-1}, \quad (7.2)$$

where $\cos\theta_v = v_z/v$, $\tan\phi_v = v_y/v_x$, and $v^2 = v_x^2 + v_y^2 + v_z^2 < 1$ (note θ_v and ϕ_v have nothing to do with the spherical coordinates; they describe the direction of the velocity vector). Together,

$$\mathbf{R}(\vec{v}) = \begin{pmatrix} \frac{v_y^2 + v_x^2 v_z/v}{v_x^2 + v_y^2} & \frac{v_x v_y(v_z/v - 1)}{v_x^2 + v_y^2} & v_x/v \\ \frac{v_x v_y(v_z/v - 1)}{v_x^2 + v_y^2} & \frac{v_x^2 + v_y^2 v_z/v}{v_x^2 + v_y^2} & v_y/v \\ -v_x/v & -v_y/v & v_z/v \end{pmatrix}, \quad (7.3)$$

when $\theta_v \in (0, \pi)$. Note $\mathbf{R}^{-1} = \mathbf{R}^\mathrm{T}$, as expected for a rotation matrix, and it rotates the vector $(0, 0, v)$ to (v_x, v_y, v_z).[1] This means that (7.3) can be used to rotate β^i, $\partial_t \beta^i$, γ_{ij}, and K_{ij} for the black hole boosted along the z-axis to get data for a boosted-trumpet black hole which is boosted in any direction. It is important to note that – while not covariant in the sense of spacetime coordinate transformations – the decomposed data is covariant under spatial coordinate transformations. Thus, the rotation matrix implements a spatial coordinate transformation and the initial data quantities then transform according to

$$\alpha[t, \vec{x}] = \alpha\left[t, \mathbf{R}^{-1} \cdot (\vec{x} - \vec{x}_0)\right] \tag{7.4a}$$

$$\beta^i[t, \vec{x}] = (\mathbf{R})^i_{\ k} \beta^k\left[t, \mathbf{R}^{-1} \cdot (\vec{x} - \vec{x}_0)\right] \tag{7.4b}$$

$$\gamma_{ij}[t, \vec{x}] = \left(\mathbf{R}^{-1}\right)^k_{\ i} \left(\mathbf{R}^{-1}\right)^l_{\ j} \gamma_{kl}\left[t, \mathbf{R}^{-1} \cdot (\vec{x} - \vec{x}_0)\right] \tag{7.4c}$$

$$K_{ij}[t, \vec{x}] = \left(\mathbf{R}^{-1}\right)^k_{\ i} \left(\mathbf{R}^{-1}\right)^l_{\ j} K_{kl}\left[t, \mathbf{R}^{-1} \cdot (\vec{x} - \vec{x}_0)\right] \tag{7.4d}$$

$$\partial_t \beta^i[t, \vec{x}] = (\mathbf{R})^i_{\ k} \partial_t \beta^k\left[t, \mathbf{R}^{-1} \cdot (\vec{x} - \vec{x}_0)\right], \tag{7.4e}$$

where $\vec{x}_0$ is the location of the puncture. See Fig. 7.1 for the set-up.

---

[1] The matrix (7.1) is the specific case where $v_z = -v$, $v_x = 0$, and $v_y \to 0$ (a limit is required to avoid dividing by zero).
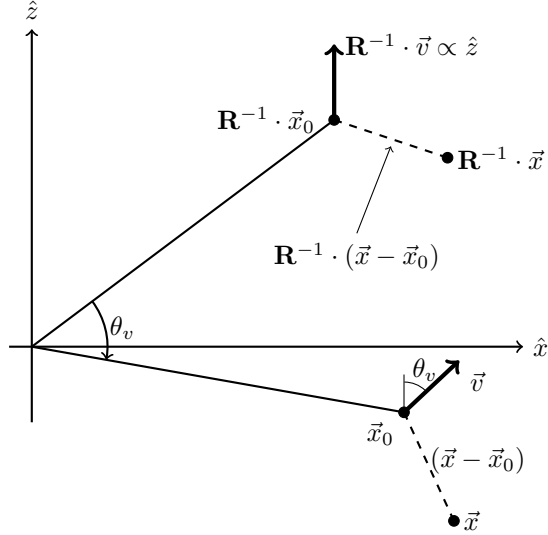
Figure 7.1: Figure showing relevant vectors for rotation of initial data via a spatial coordinate transformation (in the $\phi_v = 0$ plane for visual simplicity).

7.1.3: Boosted-Trumpet Black Holes with Spin

Because we started our series of coordinate transformations with Kerr-Schild coordinates, obtaining a boosted-trumpet black hole with spin may be a simple matter of applying (5.36) to Kerr spacetime in Kerr-Schild coordinates. However, there are a few points which need to be considered to make sure that this will work.

First, the spin axis of the Kerr black hole breaks the spherical symmetry which made it possible to boost in an arbitrary direction. Rotations must therefore be applied to make sure the spin axis and boost direction both point in the direction desired. This is likely just a matter of applying a rotation before making the coordinate change (5.36) to get the correct angle between the spin and velocity. A rotation after the coordinate change (as discussed in the previous sub-section) would then place the spin and velocity in their final directions.

Second, it must be verified that the trumpet slicing used in (5.36) covers the desired parts of the Kerr spacetime. The spatial slices must penetrate the outer horizon but not intersect the ring singularity; given that simulations with spinning black holes have been done in the moving punctures gauge it should be possible, but it is not a priori obvious where the trumpet's radius will be within the black hole. Numerical Penrose diagrams such as those constructed in [30] and an analysis based on the 2+1 decomposition [26] could both be helpful. For example, in [26] they use the 2+1 decomposition to verify that their trumpet slicing limits on a radius between the outer and inner horizons. Fig. 7.2 shows schematically what two such trumpet slicings might look like on a Penrose diagram for Kerr spacetime. Whereas overcoming the issue of

aligning the spin axis will likely be straightforward if tedious, this is potentially a more fundamental problem which could prevent extending these methods to spinning black holes.
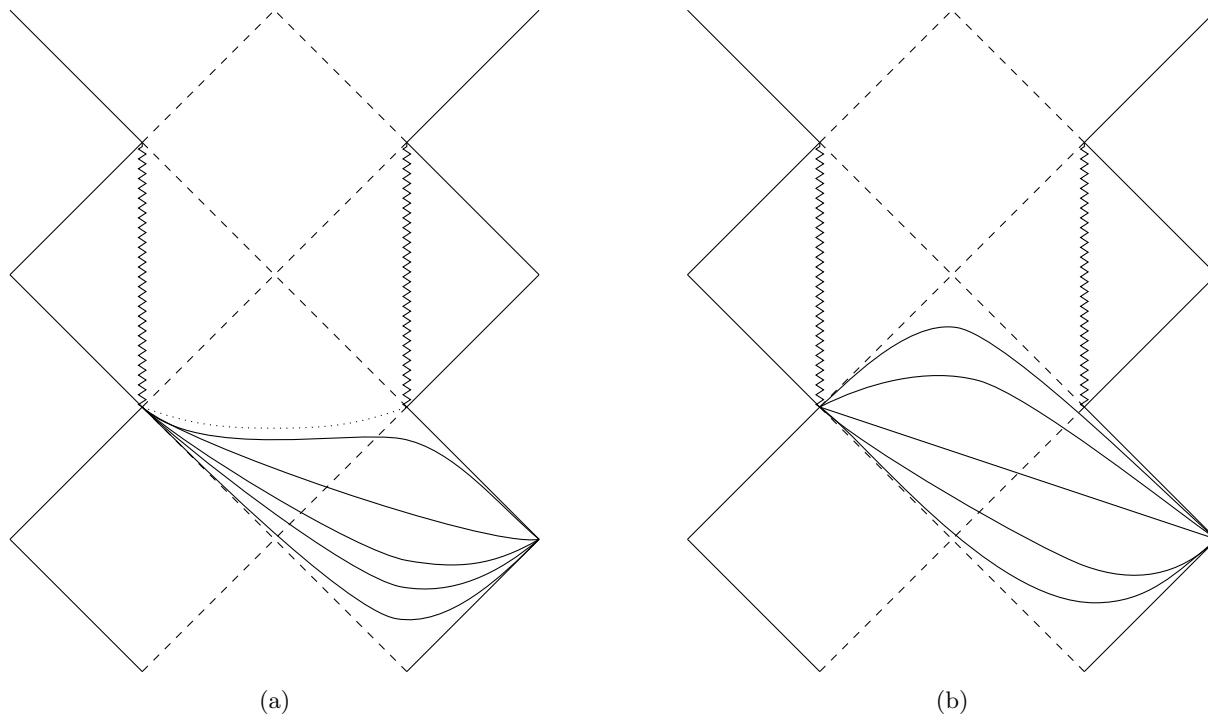

Figure 7.2: Penrose diagrams for the Kerr spacetime with two trumpet slicings. The zigzag line shows $r = 0$ (which is not singular off of the equatorial plane) and the inner and outer horizons at $r = r_{\pm}$ are shown with dashed lines. On the left the limiting radius of the trumpet slices $r_- < r < r_+$ is shown by the dotted line and on the right the limiting radius of the trumpet is r_-.

Section 7.2: Summary Remarks

After providing some theoretical and practical background, we have demonstrated a novel method for constructing initial data for single boosted black holes. We begin with Schwarzschild spacetime written in Kerr-Schild coordinates and apply a series of coordinate transformations. These transformations include

1. a Lorentz boost,

2. trumpet slicing,

3. a radial rescaling to remove the singularity from the coordinate patch (and therefore numerical simulation domain), and

4. a pair of Galilean boosts which ensure that the trumpet slicing and Lorentz boost are compatible.

Analytically, this data contains no junk radiation. Our analysis showed that – when this data is implemented in a simulation – discretization and gauge condition mis-match lead to non-zero junk radiation, though it is several orders of magnitude smaller than the junk radiation in Bowen-York initial data. This analysis relied on developing a thorough understanding of how to physically interpret the Weyl scalars when the black hole puncture is not near the origin of the tetrad. We saw that both types of initial data exhibit a growth of a background trend in ψ_4 which does not represent a physical gravitational wave and agrees well with our calculated prediction from the offset. The boosted-trumpet data also yields more immediately consistent black hole speeds than Bowen-York does.

We built initial data for a binary black hole system by superposing two copies of the boosted-trumpet initial data for a single black hole; this data approximately satisfies the constraint equations. We saw that the numerical asymmetries present in the initial data grew to the point where the black holes' trajectories were qualitatively different. We saw a similar growth in asymmetry for the Bowen-York black hole, indicating that attempting to evolve a perfectly symmetric binary may be difficult due to chaos in the non-linear evolution equations.

Finally, we looked at how boosted-trumpet initial data can be expanded into new areas. Using the approximate binary data could provide a helpful starting point for re-solving the constraint equations to obtain initial data which retains the benefits we found for a single boosted-trumpet black hole over a Bowen-York black hole while also satisfying the constraints. The application of rotation matricies to boost the black holes in any direction and using Kerr spacetime to obtain spinning boosted-trumpet black holes were discussed.

REFERENCES

[1] Einstein toolkit homepage. `https://einsteintoolkit.org/`.

[2] Gnu scientific library. `http://www.gnu.org/software/gsl/`.

[3] McLachlan Thorn Homepage. `https://www.cct.lsu.edu/~eschnett/McLachlan/`.

[4] Multipole on einstein toolkit homepage. `http://einsteintoolkit.org/documentation/ThornDoc/EinsteinAnalysis/Multipole/`.

[5] Simulation tools homepage. `http://simulationtools.org/`.

[6] B. P. Abbott, R. Abbott, T. D. Abbott, M. R. Abernathy, F. Acernese, K. Ackley, C. Adams, T. Adams, P. Addesso, R. X. Adhikari, and et al. Observation of Gravitational Waves from a Binary Black Hole Merger. *Physical Review Letters*, 116(6):061102, February 2016.

[7] B. P. Abbott, R. Abbott, T. D. Abbott, M. R. Abernathy, F. Acernese, K. Ackley, C. Adams, T. Adams, P. Addesso, R. X. Adhikari, and et al. Tests of general relativity with gw150914. *Phys. Rev. Lett.*, 116:221101, May 2016.

[8] B. P. Abbott, R. Abbott, T. D. Abbott, F. Acernese, K. Ackley, C. Adams, T. Adams, P. Addesso, R. X. Adhikari, and et al. Gw170814: A three-detector observation of gravitational waves from a binary black hole coalescence. *Phys. Rev. Lett.*, 119:141101, Oct 2017.

[9] B. P. Abbott, R. Abbott, T. D. Abbott, F. Acernese, K. Ackley, C. Adams, T. Adams, P. Addesso, R. X. Adhikari, and et al. Gw170817: Observation of gravitational waves from a binary neutron star inspiral. *Phys. Rev. Lett.*, 119:161101, Oct 2017.

[10] Abbott, B. P. et al. (The LIGO Scientific Collaboration and VIRGO Collaboration). Directly comparing gw150914 with numerical solutions of einstein's equations for binary black hole coalescence. *Phys. Rev. D*, 94:064035, Sep 2016.

[11] Abbott, B. P. et al. (The LIGO Scientific Collaboration and VIRGO Collaboration). GW151226: Observation of Gravitational Waves from a 22-Solar-Mass Binary Black Hole Coalescence. *Phys. Rev. Lett.*, 116:241103, Jun 2016.

[12] Abbott, B. P. et al. (The LIGO Scientific Collaboration and VIRGO Collaboration). GW170104: Observation of a 50-Solar-Mass Binary Black Hole Coalescence at Redshift 0.2. *Phys. Rev. Lett.*, 118:221101, Jun 2017.

[13] M. Alcubierre. *Introduction to 3+1 Numerical Relativity*. Oxford University Press, UK, 2008.

[14] Daniela Alic, Carles Bona-Casas, Carles Bona, Luciano Rezzolla, and Carlos Palenzuela. Conformal and covariant formulation of the z4 system with constraint-violation damping. *Phys. Rev. D*, 85:064040, Mar 2012.

[15] W. Ames. *Numerical Methods for Partial Differential Equations*. Academic Press, Inc., 1977.

[16] Marcus Ansorg, Bernd Brügmann, and Wolfgang Tichy. Single-domain spectral method for black hole puncture data. *Phys. Rev. D*, 70:064011, Sep 2004.

[17] Richard L. Arnowitt, Stanley Deser, and Charles W. Misner. The Dynamics of general relativity. *Gen. Rel. Grav.*, 40:1997–2027, 2008.

[18] Abhay Ashtekar and Badri Krishnan. Dynamical horizons and their properties. *Phys. Rev. D*, 68:104030, Nov 2003.

[19] John Baker, Manuela Campanelli, and Carlos O. Lousto. The lazarus project: A pragmatic approach to binary black hole evolutions. *Phys. Rev. D*, 65:044001, Jan 2002.

[20] T. W. Baumgarte and S. L. Shapiro. *Numerical Relativity: Solving Einstein's Equations on the Computer.* Cambridge University Press, June 2010.

[21] Eloisa Bentivegna. Solving the Einstein constraints in periodic spaces with a multigrid approach. *Class. Quant. Grav.*, 31:035004, 2014.

[22] L. Blanchet. Gravitational Radiation from Post-Newtonian Sources and Inspiralling Compact Binaries. *Living Reviews in Relativity*, 17:2, February 2014.

[23] Jeffrey M. Bowen and James W. York. Time-asymmetric initial data for black holes and black-hole collisions. *Phys. Rev. D*, 21:2047–2056, Apr 1980.

[24] Katy Clough, Pau Figueras, Hal Finkel, Markus Kunesch, Eugene A Lim, and Saran Tunyasuvunakool. Grchombo : Numerical relativity with adaptive mesh refinement. *Classical and Quantum Gravity*, 32(24):245011, 2015.

[25] Kenneth A. Dennison and Thomas W. Baumgarte. A Simple Family of Analytical Trumpet Slices of the Schwarzschild Spacetime. *Class.Quant.Grav.*, 31:117001, 2014.

[26] Kenneth A. Dennison, Thomas W. Baumgarte, and Pedro J. Montero. Trumpet Slices in Kerr Spacetimes. *Phys. Rev. Lett.*, 113:261101, Dec 2014.

[27] Olaf Dreyer, Badri Krishnan, Deirdre Shoemaker, and Erik Schnetter. Introduction to isolated horizons in numerical relativity. *Phys. Rev. D*, 67:024018, Jan 2003.

[28] C. R. Evans. *A method for numerical relativity: Simulation of axisymmetric gravitational collapse and gravitational radiation generation.* PhD thesis, Univ. Texas at Austin, 1984.

[29] J. N. Goldberg, A. J. Macfarlane, E. T. Newman, F. Rohrlich, and E. C. G. Sudarshan. Spins spherical harmonics and . *Journal of Mathematical Physics*, 8(11), 1967.

[30] Mark Hannam, Sascha Husa, Frank Ohme, Bernd Brügmann, and Niall Ó Murchadha. Wormholes and trumpets: Schwarzschild spacetime for the moving-puncture generation. *Phys. Rev. D*, 78:064020, Sep 2008.

[31] R. A. Hulse and J. H. Taylor. Discovery of a pulsar in a binary system. *The Astrophysical Journal*, 195(2):L51–L53, 1975.

[32] Frank Loffler, Joshua Faber, Eloisa Bentivegna, Tanja Bode, Peter Diener, et al. The Einstein Toolkit: A Community Computational Infrastructure for Relativistic Astrophysics. *Class.Quant.Grav.*, 29:115001, 2012.

[33] Geoffrey Lovelace, Mark A. Scheel, and Béla Szilágyi. Simulating merging binary black holes with nearly extremal spins. *Phys. Rev. D*, 83:024010, Jan 2011.

[34] Richard A. Matzner, Mijan F. Huq, and Deirdre Shoemaker. Initial data and coordinates for multiple black hole systems. *Phys. Rev. D*, 59:024015, Dec 1998.

[35] C.W. Misner, K.S. Thorne, and J.A. Wheeler. *Gravitation.* Freeman, San Francisco, CA, U.S.A., 1973.

[36] Hiroyuki Nakano, Yosef Zlochower, Carlos O. Lousto, and Manuela Campanelli. Intermediate-mass-ratio black hole binaries. ii. modeling trajectories and gravitational waveforms. *Phys. Rev. D*, 84:124006, Dec 2011.

[37] Andrea Nerozzi, Christopher Beetle, Marco Bruni, Lior M. Burko, and Denis Pollney. Towards a wave-extraction method for numerical relativity. ii. the quasi-kinnersley frame. *Phys. Rev. D*, 72:024014, Jul 2005.

[38] E. Newman and R. Penrose. An Approach to Gravitational Radiation by a Method of Spin Coefficients. *Journal of Mathematical Physics*, 3:566–578, May 1962.

[39] E. Newman and R. Penrose. Errata: An Approach to Gravitational Radiation by a Method of Spin Coefficients. *Journal of Mathematical Physics*, 4:998–998, July 1963.

[40] Niall Ó Murchadha and James W. York. Gravitational energy. *Phys. Rev. D*, 10:2345–2357, Oct 1974.

[41] Vasileios Paschalidis, Zachariah B. Etienne, Roman Gold, and Stuart L. Shapiro. An efficient spectral interpolation routine for the TwoPunctures code. 2013.

[42] Eric Poisson, Adam Pound, and Ian Vega. The motion of point particles in curved spacetime. *Living Rev. Rel.*, 14:7, 2011.

[43] Eric Poisson and Clifford M. Will. *Gravity: Newtonian, Post-Newtonian, Relativistic.* Cambridge University Press, Cambridge, UK, 1st edition, 2014.

[44] William H. Press, Saul A. Teukolsky, William T. Vetterling, and Brian P. Flannery. *Numerical Recipes in C: The Art of Scientific Computing.* Cambridge University Press, Cambridge, UK, 2nd edition edition, 1993.

[45] Christian Reisswig and Denis Pollney. Notes on the integration of numerical relativity waveforms. *Classical and Quantum Gravity*, 28(19):195015, 2011.

[46] I. Ruchlin, J. Healy, C. O. Lousto, and Y. Zlochower. New Puncture Initial Data for Black-Hole Binaries: High Spins and High Boosts. *ArXiv e-prints*, October 2014.

[47] Erik Schnetter, Scott H Hawley, and Ian Hawke. Evolutions in 3d numerical relativity using fixed mesh refinement. *Classical and Quantum Gravity*, 21(6):1465, 2004.

[48] Erik Schnetter, Badri Krishnan, and Florian Beyer. Introduction to dynamical horizons in numerical relativity. *Phys. Rev. D*, 74:024028, Jul 2006.

[49] Ulrich Sperhake. Binary black-hole evolutions of excision and puncture data. *Phys. Rev. D*, 76:104015, Nov 2007.

[50] Ulrich Sperhake, Vitor Cardoso, Frans Pretorius, Emanuele Berti, and José A. González. High-energy collision of two black holes. *Phys. Rev. Lett.*, 101:161101, Oct 2008.

[51] Jonathan Thornburg. Finding apparent horizons in numerical relativity. *Physical Review D*, 54(8):4899–4918, October 15 1996.

[52] Jonathan Thornburg. A fast apparent-horizon finder for 3-dimensional Cartesian grids in numerical relativity. *Classical and Quantum Gravity*, 21(2):743–766, January 21 2004. gr-qc/0306056.

[53] Petr Tsatsin and Pedro Marronetti. Initial data for neutron star binaries with arbitrary spins. *Phys. Rev. D*, 88:064060, Sep 2013.

[54] T A Wagner, S Schlamminger, J H Gundlach, and E G Adelberger. Torsion-balance tests of the weak equivalence principle. *Classical and Quantum Gravity*, 29(18):184002, 2012.

[55] Clifford M. Will. The confrontation between general relativity and experiment. *Living Reviews in Relativity*, 17(1):4, 2014.

[56] J. W. York. Kinematics and dynamics of general relativity. In *Sources of gravitational radiation.* Cambridge University Press, 1978.

[57] J. W. York and Tsvi Piran. Initial value problem and beyond. In *Spacetime and Geometry: The Alfred Schild Lectures.* University of Texas Press, 1982.